Important Notice

This copy may be used only for the purposes of research and private study, and any use of the copy for a purpose other than research or private study may require the authorization of the copyright owner of the work in question. Responsibility regarding questions of copyright that may arise in the use of this copy is assumed by the recipient.

UNIVERSITY OF CALGARY

Suppression of Water-Column Multiples by Combining Components of Ocean-Bottom Seismic Surveys

by

Yan Yan

A THESIS

SUBMITTED TO THE FACULTY OF GRADUATE STUDIES

IN PARTIAL FULFILLMENT OF THE REQUIREMENTS FOR THE

DEGREE OF MASTER OF SCIENCE

DEPARTMENT OF GEOLOGY AND GEOPHYSICS

CALGARY, ALBERTA

July, 2002

© Yan Yan 2002

THE UNIVERSITY OF CALGARY

FACULTY OF GRADUATE STUDIES

The undersigned certify that they have read, and recommended to the Faculty of Graduate Studies for acceptance, a thesis entitled "Suppression of Water-Column Multiples by Combining Components of Ocean-Bottom Seismic Surveys" submitted by Yan Yan in partial fulfillment of the requirements for the degree of Master of Science.

Supervisor, Dr. R. James Brown
Department of Geology and Geophysics

Dr. Robert R. Stewart
Department of Geology and Geophysics

Dr. Gary F. Margrave
Department of Geology and Geophysics

Dr. M. Elizabeth Cannon
Department of Geomatics Engineering

Date

ABSTRACT

Methods to suppress water-column multiples by combining components of multicomponent ocean-bottom seismic (OBS) surveys are investigated and tested on both synthetic and field data. The dual-sensor method involves the use of hydrophone and vertical geophone, two motion-sensing components. Since these instruments should record signals with the same polarity for upgoing waves, but with opposite polarity for downgoing waves, the summation of these two, recorded at the same station, with a proper scaling factor, should attenuate the downgoing waves.

Multicomponent wavefield-decomposition techniques evolve naturally from the multicomponent seafloor recording technique, whose essence is combining hydrophone, vertical-geophone and horizontal-geophone components in proper proportions to obtain the upgoing and downgoing wavefields. In order to attenuate the water-column multiples in the recorded OBS data, we can apply this technique to extract the upgoing wavefields on each of components without the downgoing multiples. Then applying a crosscorrelation method, the source-side multiples can be further identified and eliminated from the decomposed upgoing wavefields.

ACKNOWLEDGEMENTS

I would like to thank my supervisor Dr. Jim Brown for his encouragement from the beginning and enthusiastic support through the end of finishing the thesis. His insightful guidance, and serious academic attitude go through all my thesis research. I can never thank him enough for his patience and time toward my thesis research and English communication.

I would also like to thank Chanpen Silawongsawat for her constructive discussion and friendship. Thanks also go to Richard Bale for his intelligent suggestions and kind help.

Thanks to sponsors of the CREWES project at the University of Calgary.

Thanks to all the people who have given me help in my study and in my life.

TABLE OF CONTENTS

LIST OF FIGURES

Chapter 1: Introduction

1.1 The OBS technique

Ocean-bottom seismic (OBS) techniques have been used for several decades and become fairly widespread in the seismic exploration industry. Rodriguez (2000) provided a comprehensive review of the development of OBS technology and stated that the OBS technique was first used in the mid-1930s. At that time, the geology of oceanic areas was almost completely unknown. The demand for nuclear-explosion discrimination gave some impulses for OBS use after World War II, but the expectations were not fulfilled. This was because noise at marine sites was not much lower than on land, also instrument is complex, unreliable and costs highly. Only in the late 1960s, thanks to microelectronics advances, the use of OBS became widespread. Currently, ocean-bottom seismometers are used in studies of earthquakes, continental margins, and adjacent ocean basins, seduction zones, spreading centers and fracture zones.

In ocean-bottom cable (OBC) acquisition, the cable containing a stationary array of receivers is laid on the seabottom to record data. A vessel tows a source array, which emits a powerful acoustic signal that travels through the water layer into the earth. Whenever the propagating wavefield encounters an interface between layers with different elastic properties, part of the energy is reflected back towards and recorded by the receivers, while the remaining energy passes through. The receiver signals, functions of time and offset, contain information about successive subsurface interfaces. The data can therefore be processed to give a continuous profile of the subsurface structure (after O'Brien, 1997).

The dual-sensor method (hydrophone and vertical geophone) is a simple combination of components in an OBS survey. The use of three components was a natural extension of the dual-sensor method. Recording a hydrophone with three geophone components created a new type of seismic data, called four-component (4C). Currently, 4C technology has been used widely in the North Sea and the Gulf of Mexico, for example. There are a number of benefits that arise out of a 4C description of the seismic wave, which make a 4C OBS survey desirable. For example, the S-waves are much stronger than the P-waves on the inline and crossline geophone components (Rodriguez, 2000); the imaging below gas clouds using 4C recording of P-SV reflections has been successful, being the lowest-risk application for the technique (Caldwell et al., 1999).

The advantages of OBS over conventional marine streamers include a quieter environment and a therefore higher signal-to-noise ratio. The use of geophones creates the possibility of shear-wave recording. Also, the OBS technique has provided high-quality coverage, high signal bandwidth, without offset limitations, low noise and reduced dependence on weather conditions. In addition, using OBS acquisition, a true 3D image can be obtained, as several azimuths may be sampled, unlike conventional marine 3D, where several parallel 2D lines are combined to form a data volume (Rodriguez, 2000). Dragoset and Barr (1994) also mentioned some other advantages of OBS techniques, one being that the receivers can be placed in areas of high boat traffic and very close to obstacles such as production platforms. This gives much better coverage in a closely spaced survey than a towed streamer survey, which can not be conducted close to structures.

Some problems of the OBS technique include sometimes poor geophone coupling to the water-bottom, and low accuracy of receiver placement. Also, the high cost is another big limitation: it is said that a 3D OBS survey is three to six times more expensive than a conventional 3D streamer survey (Caldwell et al., 1999).

1.2 OBS data

In an OBS survey, receivers are attached to (or inside) cables, which are distributed along the survey area. The length of cable and, therefore, number of receivers are limited, so a large number of shots are used to obtain good coverage; whereas a land survey uses a larger number of receivers and fewer shots. So the common-receiver gathers are tended to be used in OBS data processing as opposed to common-shot gathers as in land data processing.

Unfortunately, the recorded data in OBS surveys always contain some degree of random and coherent noise. Figure 1.1 shows a synthetic common-receiver gather that embraces all of the OBS data recorded by a hydrophone, such as the direct arrival, seafloor refraction, subseafloor reflection and sea-surface ghost. In addition, a considerable amount of coherent noise is caused by the reverberation of seismic energy within the water layer.

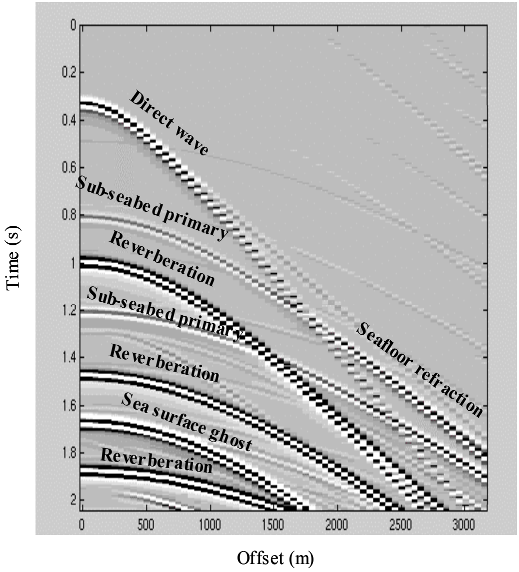

Figure 1.1. A synthetic common-receiver hydrophone gather.

Figure 1.2 shows a real common-receiver gather recorded by the four components. In addition to the direct arrival, seafloor reflection, seafloor refraction, subsea floor reflection, and reverberations, some degree of random noise is also observed. Because of innate relative sensitivity of hydrophone and geophones, it is difficult to determine the orientations of geophone axes and how well they are coupled to the water-bottom. Also, many assumptions, e.g., that the phase is matched and the impulse response of the measuring devices is the same on all components, are violated. These will bring many difficulties to multiple-attenuation efforts on real data.

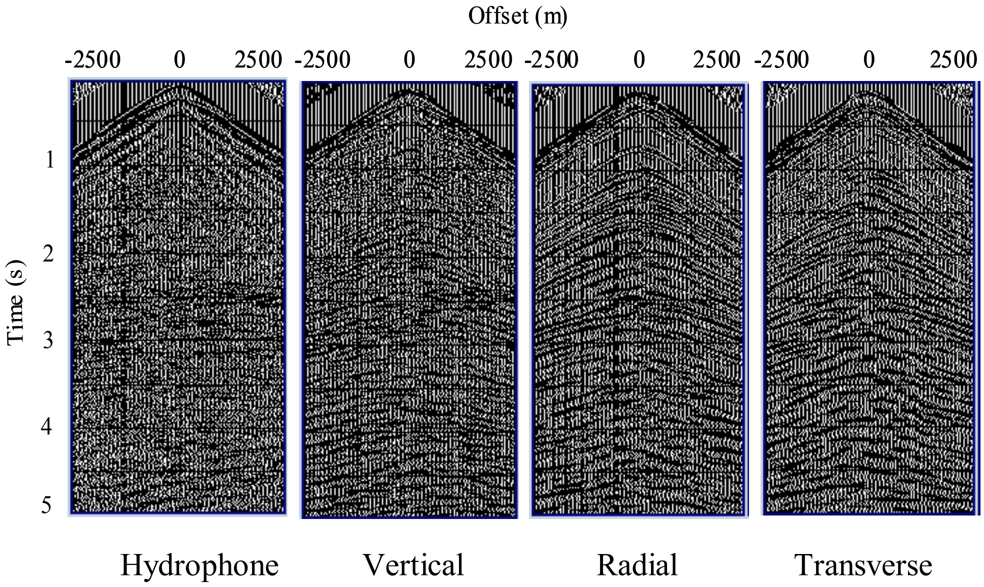

Figure 1.2. Real common-receiver gather on four components (from Gulf of Mexico).

1.3 Multiples in OBS data

All marine seismic surveys have multiple problems to some extent. According to their generating mechanism and propagating paths, multiples can be catalogued into the following types.

1.3.1 Water-column reverberations

The amount of seismic energy reflected at an interface is related to the density and velocity contrasts between the materials on either side of the boundary. The reflection coefficients increase as the contrast increases. In OBS data, since water and air have very large velocity and density contrasts, the sea-surface is almost a perfect reflector, with a downward reflection coefficient close to −1. The negative value is due to the fact that velocity decreases upwards across the boundary, causing a phase reversal (O'Brien, 1997). As a result, in areas where the seafloor is very hard, we then have an energy trap – a nonattenuating medium bounded by two strong reflecting interfaces. A seismic wave will be successively reflected in this trap, with a time interval equal to the two-way travel time, and an amplitude decay dependent on the reflection coefficients of the seafloor. These are water-column reverberations (Backus, 1959).

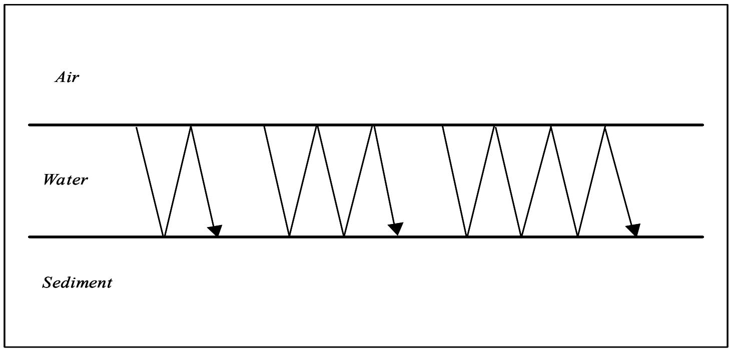

Figure 1.3. Water-column reverberations.

The harder the seafloor, the greater the number of multiples that have amplitudes comparable to the primaries. For example, a seafloor with reflection coefficient of 0.4 can produce six to eight orders of multiples that have amplitudes significantly higher than the subfloor primaries (O’Brien, 1997).

1.3.2 Receiver-side multiples

Waves traveling upward from subsurface reflective strata continue propagating after they are recorded by receivers as primary reflections. When a sharp velocity discontinuity exists above the receivers (air/water interface), the waves then reflect back, and are once more recorded by the same receivers but as downgoing waves. These are receiver-side multiples. The reverberations occur after the deeper reflection (Figure 1.4).

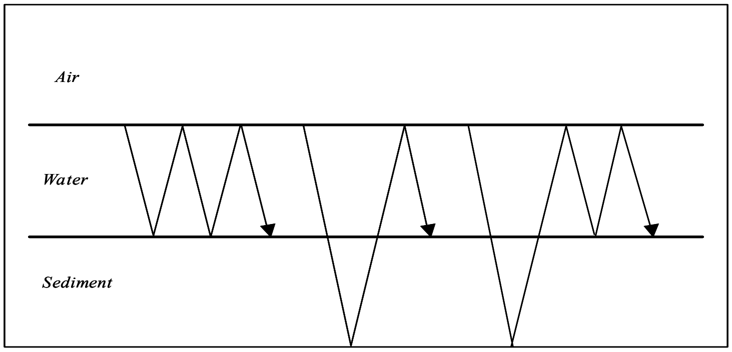

Figure 1.4. Receiver-side multiples.

1.3.3 Source-side multiples

Waves traveling downward from the source are reflected back at the sea bottom and experience one or more reflections at the air/water interface – free surface. After continuing propagation in the subsurface, they are recorded by the receivers as upgoing waves. These are source-side multiples. The reverberations occur before the deeper reflection (Figure 1.5).

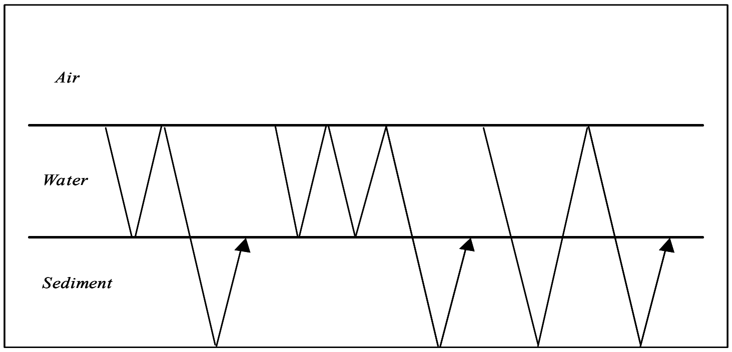

Figure 1.5. Source-side multiples.

1.3.4 Internal multiples

Internal multiples are multiply reflected events that experience two or more upward reflections in the subsurface (Figure 1.6). They are events that have all of their downward reflection points below the free-surface (Berkhout, 1982).

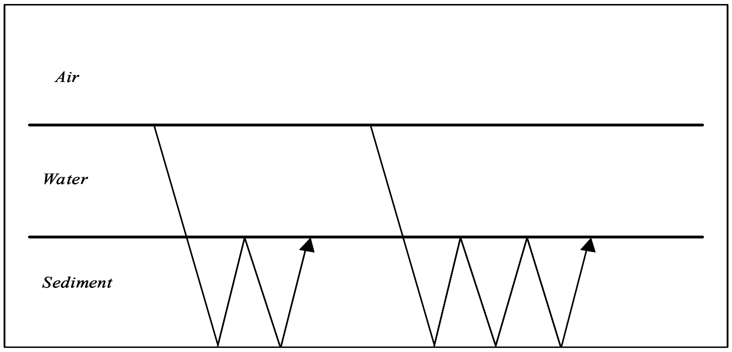

Figure 1.6. Internal multiples.

1.4 Thesis objectives

The overall objective of my thesis is to investigate new algorithms for attenuation of water-column multiples in OBS data. Addtionally, some of the existing methods are also addressed. Analyse and tests using synthetic data examples show the limited abilities of existing methods. Then a detailed investigation of wavefield-decomposition techniques is presented as a major objective of this thesis. The first goal is achieved by combining two components (hydrophone and vertical geophone) of OBS data to attenuate the water-column multiple. Then, by combining three components (hydrophone, vertical-geophone, and inline-geophone) in proper proportion, the upgoing wavefields, without downgoing multiples, are successfully extracted. The results obtained by synthetic and real data examples demonstrate that the wavefield-decomposition technique can be considered as a powerful and useful tool in multiple suppression.

1.5 Multiple suppression

The multiples in OBS data can be very strong and often contaminate seriously the primary reflections and cause problems for processors and interpreters. So suppression of multiples in OBS data processing is, without doubt, very important.

Over the past several decades, a number of processing techniques have been developed for multiple attenuation and these multiple-attenuation algorithms utilize different characteristics of multiples and primaries listed as follows:

1.5.1 The periodicity of multiples

Backus (1959) was probably the first to look at the problem from a linear-filtering point of view. He showed that the periodic nature of seafloor multiples can be used to predict which part of the recorded trace is multiple and which part is primary. Inverse filtering can then be used to remove the multiples from the trace. This method is now generally referred to as *predictive deconvolution* and will be discussed in detail in Chapter 2.

1.5.2 The different moveout between primaries and multiples

This method was developed in the early 1960s as a result of the development of multichannel processing. Because of the velocity difference between the primary and multiples, a primary and a multiple with the same vertical incidence travel-time will arrive at different times for nonvertical incidence (nonzero offset).

The Karhunen-Loève (K-L) transform, which optimally extracts coherent information from multichannel input data, can be used to attenuate the multiples. After applying the moveout correction with the velocity associated with the multiples, the gather is reconstructed using the K-L procedure, and the information associated with the multiples is omitted (Jones and Levy, 1987).

Another example of using the moveout difference between primaries and multiples for multiple suppression is the τ-p transform. In this case, it is better to apply NMO correction on the input data using the primary velocities. After the NMO, primary events become flattened, but multiples have residual moveout, increasing with offset. Having different moveouts, the primary and multiples will appear in different regions of the transform domain. Then a proper mute can be applied in the transform domain to get rid of multiples and an inverse τ-p transform can be applied (Russell and Hampson, 1990). These two methods will be discussed in detail in Chapter 2.

Stacking is also recognized as a very effective way of dealing with incoherent noise and long-period multiple interference on the far offsets. It is less effective on many other types of noise (such as short-period multiples and ground roll). Unfortunately, stacking does not eliminate all multiples and it attenuates multiples only for the stacked section (Yilmaz, 1987).

1.5.3 The difference in frequency content between primaries and multiples

According to the difference in frequency content between primaries and multiples, filtering techniques can be used for multiple elimination. Filtering techniques can be further subdivided into single-channel and multichannel forms. The simplest single-channel filter is the bandpass filter in which frequencies above and below selected cutoff points are rejected. This assumes that the multiple separates cleanly from the primary in the frequency domain, but this assumption is not always valid. The more effective filtering techniques for multiple attenuation are multichannel filtering. There, a group of traces is used in the estimation and removal of the multiple (Yilmaz, 1987).

A common 2D multichannel filter is the *f-k* filter, which is applied in the 2D frequency domain. The *f-k* filter is based on the fact that certain multiple patterns separate very effectively from primaries in the *f-k* domain. The disadvantage of the *f-k* filter is that, if it is applied too severely, the output data can look smeared. In particular, when the frequency content of a primary approaches the frequency content of a multiple, it is difficult to keep the primary in removing the multiple (Russell and Hampson, 1990).

In marine surveys, receivers are placed at some depth below the free surface. When waves travel upward from subsurface reflective strata and continue propagating after being recorded by receivers as primary reflections, they are then reflected back by the free surface and are once more recorded by the same receivers but as downgoing waves. This phenomenon can be referred to as the receiver ghost (Aytun, 1999). If we look at the *f-k* responses of receiver ghosts and primaries in a record, we can see that the null frequencies are caused by the time differences between the primary and the ghost arrivals. This strong frequency-spectral feature caused by the receiver ghost can be used to derive an algorithm to attenuate the receiver ghost, this method will also be discussed in detail in Chapter 2.

1.5.4 The difference in arrival directions between primaries and multiples

Very recently, due to advances in OBS acquisition, a number of new possibilities for multiple suppression have been introduced into OBS data processing. Dual-sensor and multicomponent wavefield-decomposition techniques are suitable methods for OBS multiple attenuation.

The dual-sensor method designs a scaling factor between hydrophone and vertical geophone then sums these two data components to attenuate the downgoing waves (Dragoset and Barr, 1994; Paffenholz and Barr, 1995; Barr and Sanders, 1989; Barr, 1997; Barr et al., 1997). The multicomponent wavefield-decomposition technique combines the hydrophone, horizontal- and vertical-geophone components in proper proportion to gain the upgoing and downgoing wavefields (Berkhout, 1982; Amundsen and Reitan, 1994; Osen et al., 1999; and Schalkwijk et al., 1999).

The fundamental physical principle of these techniques lies in the recognition that much of the multiple energy in seafloor recordings has propagated downward through the water, whereas the primary arrivals have propagated from the subsurface in the upward direction to the receivers. So with a proper proportions of hydrophone, horizontal- and vertical component data, the upgoing wavefields, without the downgoing waves, can be extracted.

1.6 Structure of thesis

In Chapter 1, a review of the fundamental concepts has been provided in order to give some background information on the topic of my research. The concepts of the OBS technique, OBS multiples, and OBS multiple suppression are described.

Chapter 2 contains a comprehensive discussion of current multiple-attenuation techniques (predictive deconvolution, K-L transform, *τ-p* transform, and *f-k* attenuation). Various methods have been tested on synthetic data to evaluate their effectiveness and analyze the advantages and disadvantages of the different methods.

The dual-sensor method for OBS multiple attenuation is addressed in Chapter 3. A new variation of the dual-sensor method based on crosscorrelation is reported, and a comparison of this method with two other dual-sensor methods is performed on both synthetic data and real data.

In Chapter 4, the multicomponent wavefield-decomposition technique is investigated, decomposing wavefields into upgoing and downgoing parts. The approach for extracting the upgoing wavefields on hydrophone, vertical-geophone, and inline-geophone components is realized in the *f-k* domain. Synthetic data and real data examples are provided for illustration. Lastly, conclusions are drawn and future work is suggested in Chapter 5.

Chapter 2: Review of current methods

2.1 Predictive deconvolution

Predictive deconvolution has proven to be a useful tool for suppression of multiples and the method of predictive deconvolution is based on the *prediction filter*.

2.1.1 Method

A prediction process is suggested by a time-advanced form of the input series. Given the input $x(t)$, its value $x(t+m)$ can be predicted at some future time $(t+m)$, where m is predictive lag. Robinson and Treitel (1980) showed that the prediction filter used to estimate $x(t+m)$ can be computed by solving the matrix equation:

$$\begin{bmatrix} r_0 & r_1 & r_2 & \cdots & r_{n-1} \\ r_1 & r_0 & r_1 & \cdots & r_{n-2} \\ r_2 & r_1 & r_0 & \cdots & r_{n-3} \\ \vdots & \vdots & \vdots & \ddots & \vdots \\ r_{n-1} & r_{n-2} & r_{n-3} & \cdots & r_0 \end{bmatrix} \begin{bmatrix} a_0 \\ a_1 \\ a_2 \\ \vdots \\ a_{n-1} \end{bmatrix} = \begin{bmatrix} r_m \\ r_{m+1} \\ r_{m+2} \\ \vdots \\ r_{m+n-1} \end{bmatrix}, \tag{2.1}$$

where r_i is the ith lag of the autocorrelation of the data $x(t)$, a_i is the ith element of the prediction filter, n is the length of the prediction filter and m is the desired delay, generally called the prediction lag. In the seismogram, if the period for multiples is constant, then the multiple can be estimated by convolving the prediction filter with the data and applying the desired delay time. The multiple-attenuated data can then be determined by subtracting the multiples from the original data. The processing procedure is illustrated in Figure 2.1:

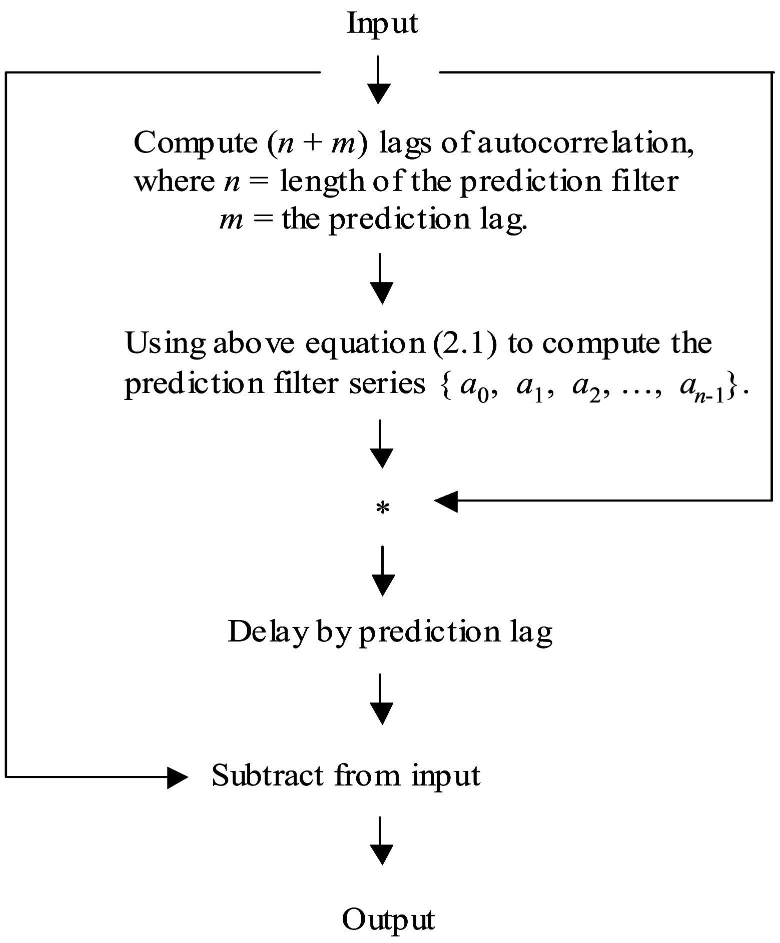

Figure 2.1. A flowchart for predictive deconvolution using prediction filters (after Yilmaz, 1987).

This can also be done by applying a modified filter, called the prediction-error filter:

$$\{1, \underbrace{0, 0, \ldots 0}_{m\ -1 \text{ zeros}}, -a_0, -a_1, -a_2, \ldots, -a_{n-1}\}, \tag{2.2}$$

and the processing procedure is illustrated in Figure 2.2:

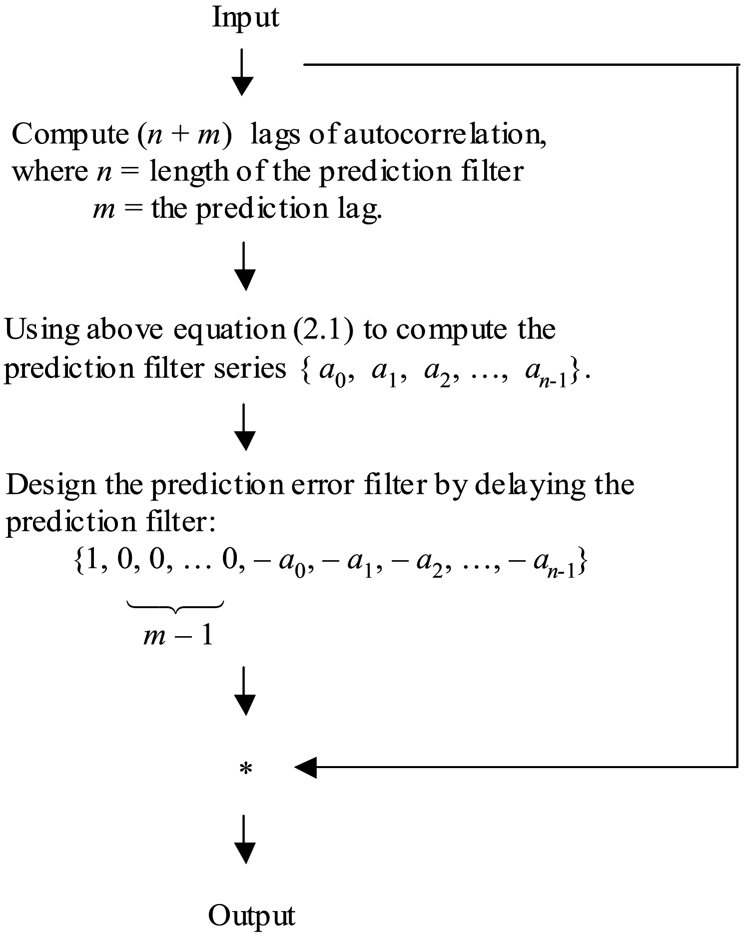

Figure 2.2. A flowchart for predictive deconvolution using prediction error filters (after Yilmaz, 1987).

2.1.2 Synthetic data example

We have learned that a prediction filter predicts the periodic multiples in the seismogram. The prediction error filter yields the unpredictable component of the seismogram; i.e., the reflectivity series. The following example will show how the water-column reverberations can be attenuated by applying a predictive deconvolution technique.

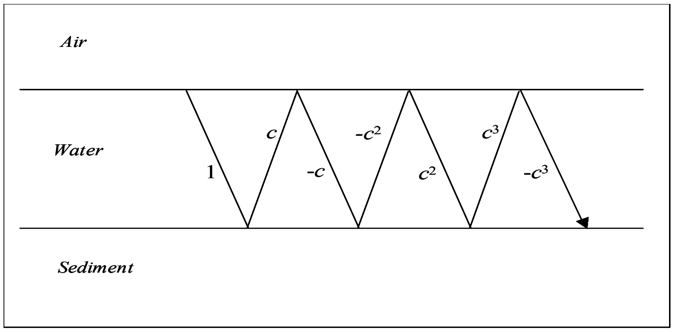

Figure 2.3. Water-column reverberations.

Figure 2.3 represents an idealized noise-free model. An incident seismic pulse with magnitude 1 will be successively reflected between the air-water surface (with reflection coefficient –1) and the seabottom reflector (with reflection coefficient c). The two-way traveltime through the water layer is τ. The form of the water-confined reverberation time series is,

$$x(t) = (1, \underbrace{0, 0, \dots, 0}_{\tau\,-\,1 \text{ zeros}}, -c, \underbrace{0, 0, \dots, 0}_{\tau\,-\,1 \text{ zeros}}, c^2, \underbrace{0, 0, \dots, 0}_{\tau\,-\,1 \text{ zeros}}, -c^3, 0, 0, \dots). \qquad (2.3)$$

To compute the prediction filter, the autocorrelation of $x(t)$ need be calculated, which is

$$\begin{array}{ll} r_t = 1 + c^2 + c^4 + \dots, & t = 0. \\ r_t = 0, & 0 < t < \tau. \\ r_t = -c(1 + c^2 + c^4 + \dots) = -cr_0, & t = \tau. \end{array} \qquad (2.4)$$

Let the filter length, n, be less than τ, and let the prediction distance be $m = \tau$. Then the matrix equations (2.1) become:

$$\begin{bmatrix} r_0 & 0 & \cdots & 0 \\ 0 & r_0 & \cdots & 0 \\ & & \vdots & \\ 0 & 0 & \cdots & r_0 \end{bmatrix} \begin{bmatrix} a_0 \\ a_1 \\ \vdots \\ a_{n-1} \end{bmatrix} = \begin{bmatrix} r_\tau \\ 0 \\ \vdots \\ 0 \end{bmatrix}, \tag{2.5}$$

The only member of this system whose right-hand side does not vanish is,

$$r_0 \, a_0 = r_\tau,$$

and thus,

$$a_0 = r_\tau / r_0 = -\, c r_0 / \, r_0 = -\, c.$$

The associated prediction-error operator is

$$f(t) = 1 , \underbrace{0, \, 0, \, \ldots,}_{\tau - 1 \text{ zeros}} \, 0, \, c, \, \ldots \, .$$

Then we have (after Peacock and Treitel, 1969):

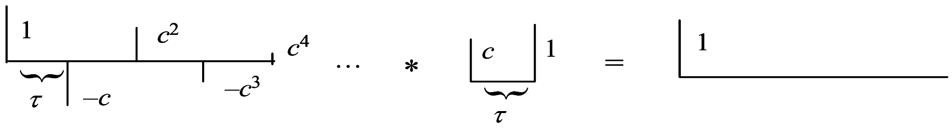

input prediction error filter output

where $*$ denotes convolution.

After applying the predictive deconvolution technique, the water-bottom reverberations was successful removed.

2.1.3 Discussion

Provided all of the assumptions about the data (minimum-phase wavelet, stationary source waveform, constant multiple period) are met, predictive deconvolution should be able to remove all of the periodic multiples.

In the presence of high-amplitude primaries and random noise, the prediction filter may have difficulty determining which part of the trace is multiple and which is not. As a result, the multiples may not be attenuated very well and it may actually cause some attenuation of the primaries. Also, it is only with vertical incidence and zero-offset recording that periodicity of the multiples is preserved. With increasing offset, considerable variations in the multiple period as well as severe amplitude and phase problems greatly reduce the effectiveness of predictive deconvolution aimed at multiple suppression (O'Brien, 1997).

2.2 Karhunen-Loève transform

The Karhunen-Loève (K-L) transform, which optimally extracts coherent information from multichannel input data, can be used for multiple suppression in seismic data processing. After applying the moveout correction associated with the multiples, the events of multiples are made flat whereas the primary events are under or overcorrected. The Karhunen-Loève transform then produces a set of uncorrelated (orthogonal) principal components from the dataset and segregates the energy associated with the multiples onto a single principle component. A data reconstruction omitting that principal component which is associated with 'fairly large' eigenvalues should be essentially multiple-free (Jones and Levy, 1987).

Application of the K-L method to seismic signals was considered early on by Hemon and Mace (1978), Jones (1985), and Ulrych et al. (1983). The recent application introduced by Jones and Levy (1987) is the suppression of multiples in CDP or CMP gathers by isolating coherent energy associated with a different coherent energy or from incoherent energy. The term 'coherent' refers to events that are similar horizontally in a trace-to-trace sense.

2.2.1 Application of the K-L transform

The application of the K-L transform for multiple suppression requires that the multiple events possess trace-to-trace coherency, so multiple suppression can be realized by isolating coherent energy from incoherent energy.

Given the seismic data $s(t)$, if we apply the moveout correction using the velocity associated with the observed multiples, then we have data $x(t)$ with the flattened multiple events. The covariance matrix, Γ, is constructed using the matrix $\mathbf{X}$:

$$\boldsymbol{\Gamma} = \mathbf{X}\mathbf{X}^{\mathrm{T}}, \tag{2.6}$$

where, $\mathbf{X} = \{x_i(t), i = 1,\ldots, n\}$, the seismic trace $x_i(t)$ are the rows of $\mathbf{X}$.

Since Γ is symmetric with dimensions $n \times n$, where n is the number of traces in the gather. It can be written in the form:

$$\boldsymbol{\Gamma} = \mathbf{R}\boldsymbol{\Lambda}\mathbf{R}^{\mathrm{T}}, \tag{2.7}$$

where the columns of $\mathbf{R}$ are the eigenvectors of Γ, and Λ is the diagonal matrix of eigenvalues. The eigenvalues are ordered from the largest to the smallest along the principal diagonal of Λ, and the corresponding eigenvectors are placed in the columns of $\mathbf{R}$ in the same order.

The principal components of data $\boldsymbol{\Psi} = \{\psi_j(t), j = 1,\ldots,n\}$ can be written as:

$$\mathbf{\Psi} = \mathbf{R}^{\mathrm{T}}\mathbf{X}. \tag{2.8}$$

If we form the matrix $\mathbf{\Psi}'$ by omitting the top m rows of $\mathbf{\Psi}$ (i.e., the principal components for the m largest eigenvalues) and remaining the $n - m$ rows, the multiple-free data can be obtained (after Liu, 1999) by:

$$\mathbf{X}'=\mathbf{R}\mathbf{\Psi}' \tag{2.9}$$

2.2.2 Summary of procedure

The procedure of attenuating multiples via the K-L transform can be summarized in five basic steps (after Jones and Levy, 1987):

1. From a velocity analysis, identify the stacking velocity and onset time associated with the observed multiples.

2. Apply the moveout correction to the data using this velocity. At this stage the arrivals due to multiples have been more or less flattened, whereas the primary events are under- or overcorrected, and have increased curvature in the section.

3. Compute the K-L transform of these moveout-corrected data. Correlated multiple energy in the gather now appears predominantly on the first principal component.

4. Reconstruct the moveout-corrected gather from the principal components omitting the first principal component, i.e., leave out any correlated energy associated with the multiples. It may also be advantageous to omit the second principal component when the waveform of the multiples has been severely distorted by interfering primary events, or by moveout operation.

5. Remove the moveout streching from the reconstructed data using the same moveout as in step 2.

2.2.3 Synthetic data example

Figure 2.4 shows a simple synthetic data gather representing reflection events from flat layers over a half-space, all overlain by water (after Jones and Levy, 1987). We can see the water-bottom multiples are present for events approximately at 1.10 s and 1.65 s. From velocity analysis, we know the multiple events at 1.10 and 1.65 s have a velocity of about 1450 m/s. Figure 2.5 shows the data after a constant-velocity NMO correction. Note that the multiple events at 1.10 and 1.65 s are now flattened. Also note that the primary at 1.4 s is overcorrected.

Application of K-L decomposition to the data window 1.00-1.80 s, and reconstructing (omitting the first and second principal component) gives the results in Figure 2.6. This result is then reverse-NMO'd (Figure 2.7). Comparing with Figure 2.4, we can see that the multiples have been effectively removed from the data.

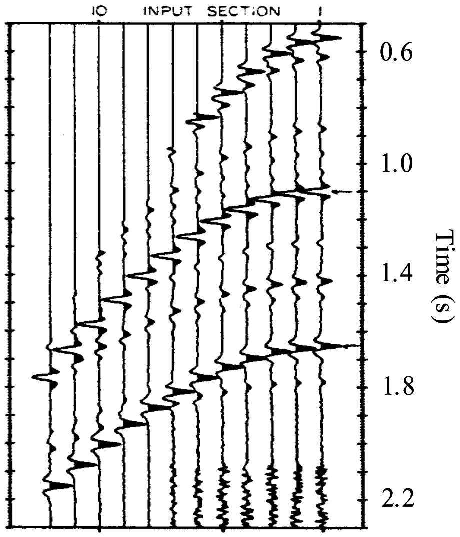

Figure 2.4. Input synthetic data.

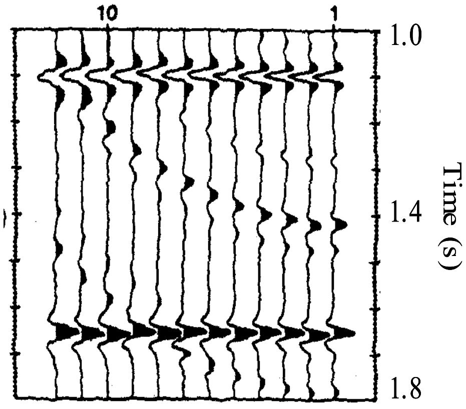

Figure 2.5. Data window after NMO correction.

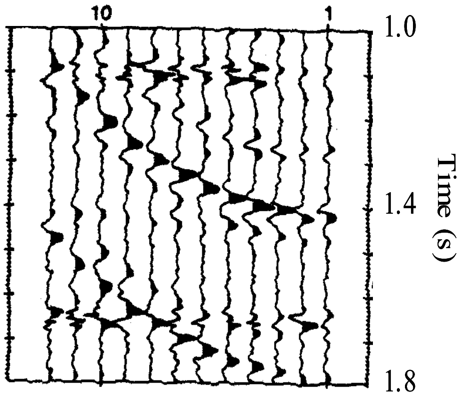

Figure 2.6. Reconstruction of the NMO-corrected data, omitting the first two principal components.

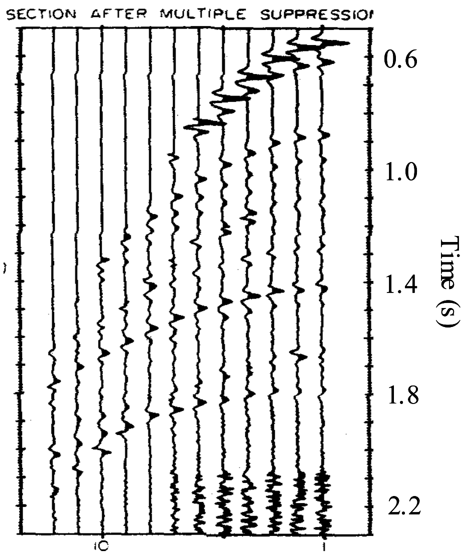

Figure 2.7. The processed data after attenuation of the multiples (after Jones and Levy, 1987).

2.2.4 Discussion

The K-L transform succeeds in suppressing multiples without distorting the reflection signal, even when signals and multiples overlap. The disadvantage of this method is that has high computational cost and requires a moveout contrast between the primary and multiple.

2.3 Radon or τ-p transforms

The τ-p transform, also called the Radon transform, transforms seismic data from the time-offset (t-x) domain to τ (intercept time) and p (ray parameter) domain. Performing the τ-p transform, the data in the t-x domain are summed along straight lines (linear τ-p transform or slant-stack) or along parabolas or hyperbolae (parabolic or hyperbolic τ-p transform) to yield points in the τ-p domain.

2.3.1 Linear τ-p transform

The linear τ-p transform sums along linear slopes in the t-x or offset domain (each slope representing a different p value) to yield data points in the τ-p domain.

Two steps typically are used in synthesizing plane waves by summing amplitudes in the offset domain along slanted paths. First, a linear moveout (LMO) correction is applied to the data through a coordinate transformation (Claerbout, 1976):

$$\tau = t - px, \tag{2.10}$$

where p is the ray parameter, x is the offset, t is the two-way traveltime at offset x, and τ is time at zero offset. After this LMO correction, an event with slope p on input is flat. Next, the data are summed over the offset axis to obtain:

$$\varphi(p,\tau) = \int \psi(x, \tau + px)dx\,, \tag{2.11}$$

where, $\psi(x, \tau + px)$ represents the trace in the *t-x* domain, and $\varphi(p, \tau)$ represents a plane wave with ray parameter $p = (\sin\theta)/v$. By repeating the LMO for various values of p and performing the sum (equation 2.11), the complete slant-stack (or *p*-gather), which consists of all the dip components in the original offset data, is constructed.

The mathematical transform defined by equation (2.11) has an inverse which can be written:

$$\psi(x,t) = \int \varphi(p, t - px)dp \ . \tag{2.12}$$

The schematic description of the plane-wave mapping described by equations (2.11) and (2.12) is shown in Figure 2.8. In this figure, the p values are defined by angles. A linear event, with a dip p and zero-offset intercept τ, will transform to a point at time t after a τ-p transform. In the inverse τ-p transform, points transform to straight lines.

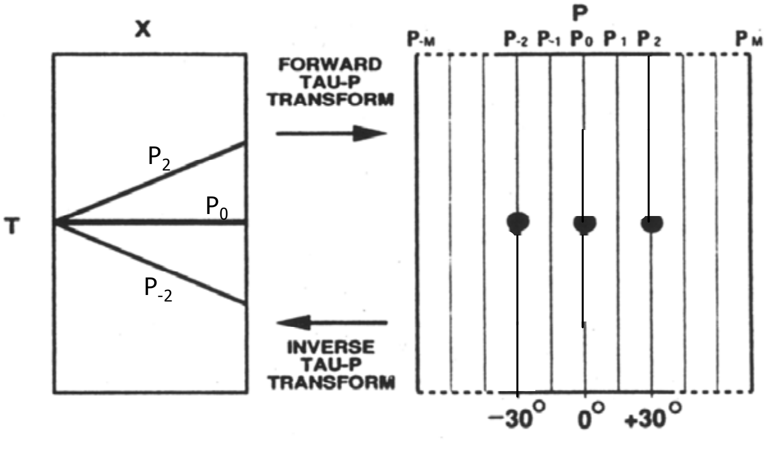

Figure 2.8. Forward and inverse linear τ-p transforms (Russell and Hampson, 1990).

Direct arrivals, ground roll, reflections, refractions have different incidence angles or different p values. It is difficult to separate them in the *t-x* domain but, in τ-p space, these events can be well separated. For example, ground roll transforms to a point at time zero, refractions transform to points at their zero-offset intercept times and reflection hyperbolae transform to ellipses. Significantly, the ellipses do not cross one another, even if the reflection hyperbolae do cross each other in *t-x* record space.

In Figure 2.9, the left-hand panel schematically represents events on a seismic field record. Hyperbolae A, B and C represent reflections. Linear events D, H1 and H2 represent directly arriving ground-roll (D) and two refractions. To construct the *τ-p* transform, the data in the seismic record are summed along a linear slope (slant-stack) for a specific *p*-value and for all intercept times, *τ*, to yield a single *p*-trace for the transform. The sample trace in the left panel, generated by summing along slant p_1, is a single trace in the right panel. The right panel, representing the equivalent *τ-p* space, has traces that are time series, but each trace has a specific slant, or slope, *p*. The quantity *p* has units of reciprocal velocity (μs/ft). Events that interfere in the left panel are separated in the right panel. In particular, reflection hyperbolae A, B and C become ellipses A, B and C. The linear event D has a slope of 300 μs/ft, and is thus beyond the range of *p*-values in this transform. The refractions H1, and H2 become points (or small regions) H1, and H2 in *τ-p* space, the arrival time is just the zero-offset intercept time of the refractions (Tatham et al., 1982).

Once a particular process is carried out in the (*τ-p*) domain, the inverse *τ-p* transform is used to reconstruct the data in the (*t-x*) domain. Performing the inverse *τ-p* transform, each point in (*t-x*) is constructed by integrating along a linear trajectory in (*τ-p*) domain (Margrave, 1999). This is accomplished by a similar slant-stack on the *τ-p* record along slopes *dτ/dp* corresponding to a particular *x*. Thus, the same algorithm is used in performing the inverse transform that is applied in constructing the forward transform (Tatham et al., 1982).

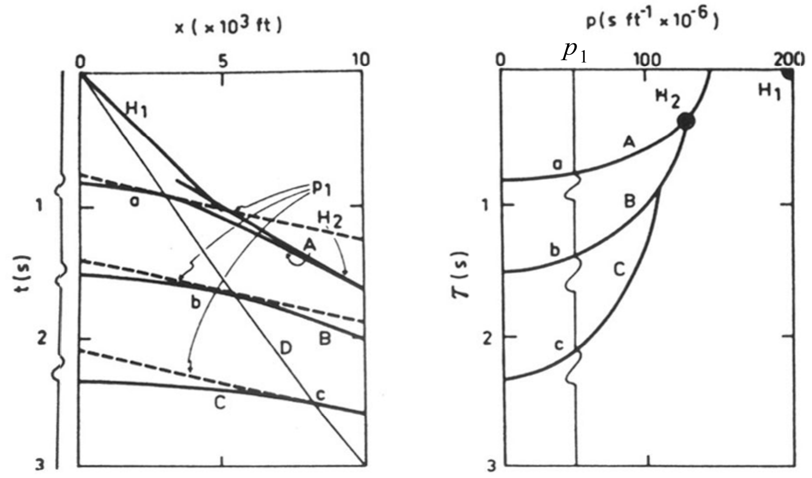

Figure 2.9. The linear *τ-p* transform showing linear events mapping to points and hyperbolae mapping to ellipses (Tatham et al., 1982).

2.3.2 Generalized *τ-p* transform

In the linear *τ-p* transform, a straight line is most suitable for modeling events with linear moveout. However, it may not always be the most appropriate transform when we try to model hyperbolic NMO curves. A better curve for matching normal moveout would appear to be the hyperbola.

In this case, all traces in the (*t-x*) domain are summed along a hyperbola to yield a single trace in (*τ-q*) domain. Forward transform:

$$\varphi(q,\tau) = \int \psi[x,\ (\tau^2 + qx^2)^{1/2}]dx\,, \tag{2.13}$$

and inverse transform:

$$\psi(x,t) = \int \varphi[q,\ (t^2 - q^2x^2)^{1/2}]dq\,, \tag{2.14}$$

where q has units of slowness s/m or s/ft.

Equation (2.12) can be used for modeling any events with linear moveout. Equation (2.14) can be used to model hyperbolic NMO curves. But its square root operation makes this a nonlinear equation and therefore difficult to implement in the frequency domain on a computer. An ideal compromise may therefore be the parabolic curve which displays curvature but does not involve taking a square root (Russell and Hampson, 1990). We call these (hyperbolic and parabolic) generalized Radon transforms. The latter will map a parabola to a point in the transform domain. We can also think of it as an extension of the *τ-p* transform. So, we have the forward transform:

$$\varphi(q,\tau)=\int\psi(x,\tau+qx^2)dx\,, \tag{2.15}$$

and inverse transform:

$$\psi(x,t)=\int\varphi(q,t-qx^2)dq\,, \tag{2.16}$$

where q is can be thought of as a generalized slowness, with units of s/m^2 or s/ft^2.

Figure 2.10 is an NMO-corrected CDP profile; P indicates a corrected primary, and M1 and M2 indicate undercorrected multiples. The three events map to three isolated points in the Radon domain. Then we can selectively filter the data in the Radon domain by the elimination of signal points. Then, when we perform an inverse transform to get back into the time domain, entire multiple events have vanished (Figures 2.10 and 2.11) (Russell and Hampson, 1990).

2.3.3 Synthetic data example

Since primaries and multiples have different moveout in the *t-x* domain, they will appear in different regions in the *τ-p* domain. By properly selecting a filter in the *τ-p* domain, the multiple data can be attenuated. Then an inverse transform can be performed to get back into the time and offset domain.

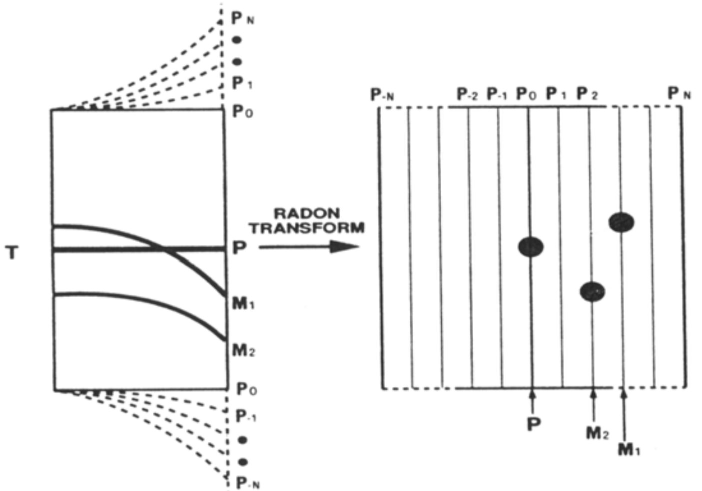

Figure 2.10. Generalized discrete Radon transform.

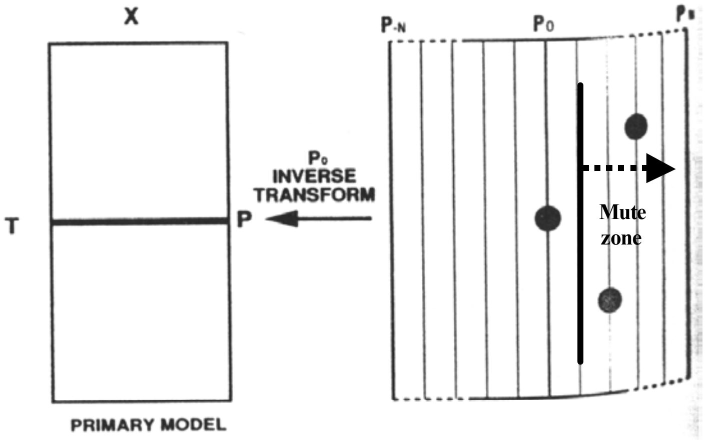

Figure 2.11. Selective inverse Radon transform (Russell and Hampson, 1990).

In order to demonstrate the performance of the τ-p transform, a synthetic test was carried out. The model consists of a water layer and two flat homogeneous layers with tops at depths of 1000 m and 2000 m, respectively. The corresponding velocities of the two layers are 1500 and 2200 m/s, respectively. The processing procedure is shown in Figure 2.12. The synthetic common-shot-point (CSP) gather is shown in Figure 2.13. We can see the water-bottom multiples are present for events approximately at 2.7, 4.5 and 5.0 s, while primaries are present for events approximately at 1.4 and 3.2 s.

The processing procedure using the linear τ-p transform is as follows:

- Applying NMO on input data, primaries become flattened, but multiples have residual moveout increasing with offset (Figure 2.14). The maximum moveout is 2000 ms.
- Using the linear τ-p transform, the flattened primaries appear at around $p = 0$, while undercorrected multiples appear at around $p > 0$ in the τ-p domain (Figure 2.15). Now, primaries are distinguished clearly from multiples.
- Pick mutes in (τ, p) domain that pass primaries and remove multiples, that means keep trace ($p \approx 0$), mute traces ($p > 0$) (Figure 2.16).
- Perform inverse transform back to offset space to get the model common-shot gather (Figure 2.17). Now it is a primaries-only common-shot gather.

The model result confirms that this algorithm is very powerful at attenuating multiples and the attenuation is equally good at all offsets.

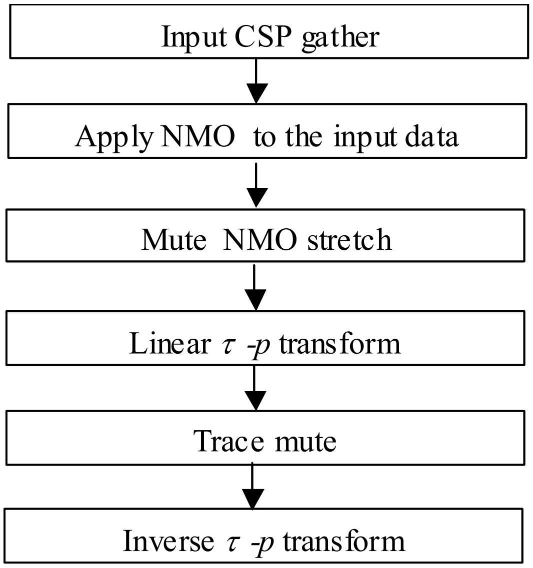

Figure 2.12. A flowchart for using the linear τ-p transform.

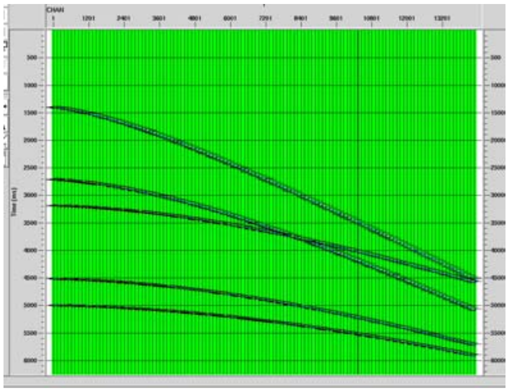

Figure 2.13. A synthetic common-shot gather.

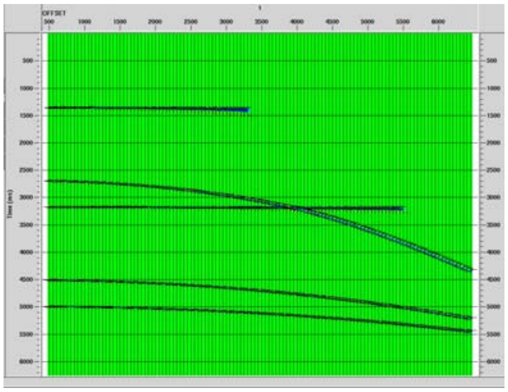

Figure 2.14. Applying NMO and muting stretch.

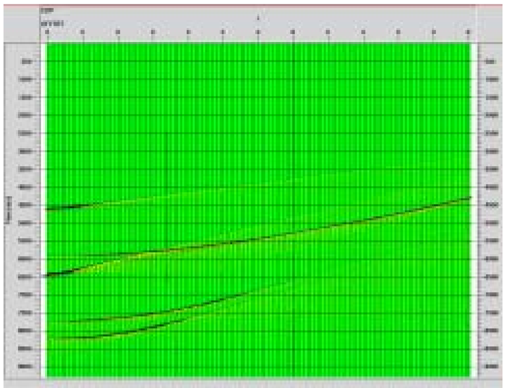

Figure 2.15. Applying linear τ-p transform.

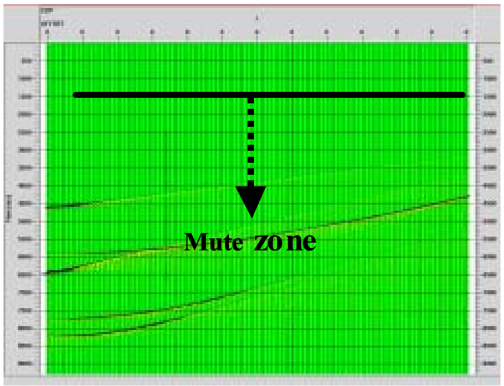

Figure 2.16. Trace muting in τ-p domain.

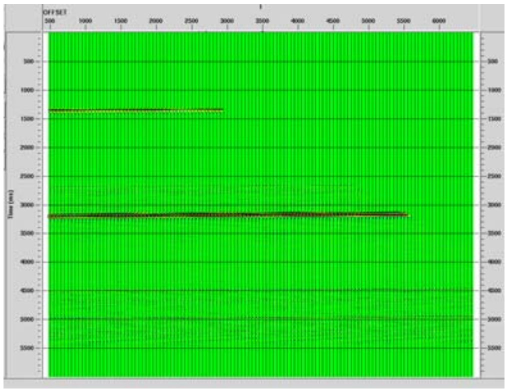

Figure 2.17. Inverse τ-p transform reconstructing the common-shot gather.

The input profile is still the NMO-corrected common-shot gather (Figure 2.14). The processing procedure using the Radon transform is as follows (Figure 2.18).

- After Radon transform, the data are mapped onto time-moveout space. Since the input data is NMO-corrected, the primary energy map to events at around 0*ms* move-out, while undercorrected multiples map to higher moveout (Figure 2.19).
- Pick a suitable mute to eliminate the primary energy (Figure 2.20). The multiple energy is left, which can then be modeled. See Figure.2.21.
- Subtracting the multiple model from the input data produces the final multiple-attenuated result in Figure 2.22.

Comparing with the results obtained with input data model (Figure 2.14), we can see the multiple-attenuation method described here has removed a significant amount of multiple energy in this synthetic example.

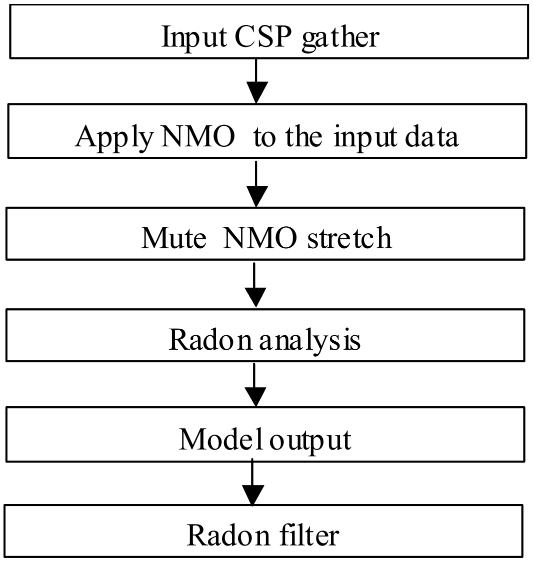

Figure 2.18. A flowchart for using the Radon transform.

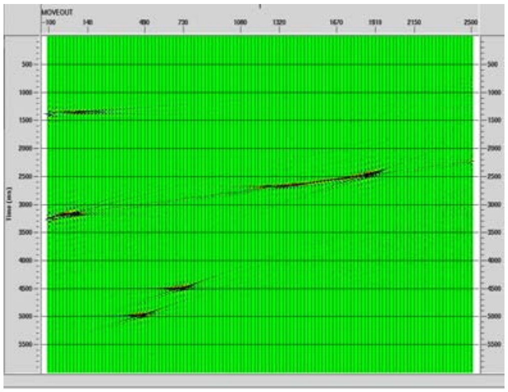

Figure 2.19. Applying the Radon transform.

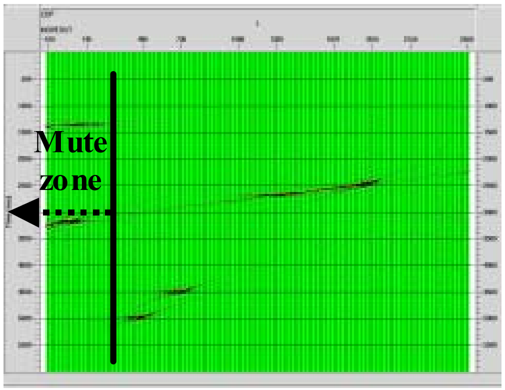

Figure 2.20. Trace mute in transform domain.

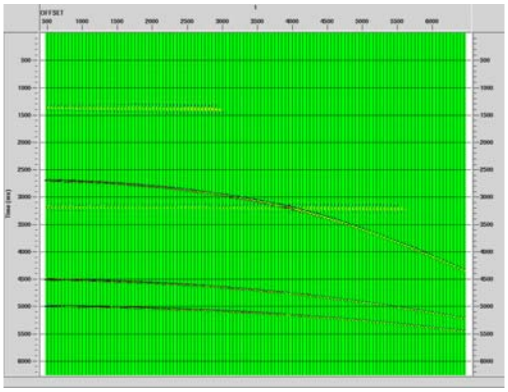

Figure 2.21. Multiple model output.

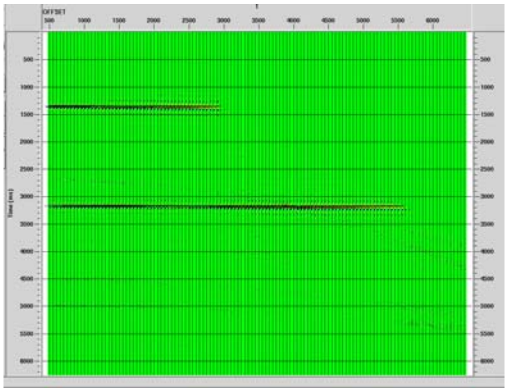

Figure 2.22. The final multiple-attenuated result.

2.3.4 Discussion

The *τ-p* transform provides a useful tool for multiple elimination. In the *τ-p* domain, many difficult problems become less difficult. The methods tested on a synthetic common-shot-point gather attenuate multiples by the moveout difference between primaries and multiples. The test results show that it is very effective in attenuating multiples from zero-offset to far-offset, and using this method, we do not need to know the multiple-generating mechanism or have detailed knowledge of the multiple and primary velocities; it will attenuate a wide range of multiples with variable moveouts.

The linear *τ-p* algorithm is based on a plane-wave model and is ideally suited to modeling linear events. The hyperbolic *τ-p* algorithm is based on a hyperbolic model and is ideally suited to modeling hyperbolic or approximately hyperbolic events. For the above simple synthetic example, both linear and hyperbolic transform provided a successful application. However, for more complicated cases, a hyperbola appears to be a better curve for fitting normal moveout, e.g., the trajectories of long-period multiples after NMO-correction at the primary velocity are more closely approximated by hyperbolae than by straight lines.

Another important feature of the algorithm is: while the primaries should be NMO-corrected, it is not necessary that the correction be exact.

Limitations associated with this method are that *τ-p* transform–based multiple suppression schemes are fundamentally limited by the transform's ability to resolve different events on the basis of moveout differences. Moveover, multiples must have sufficient move-out discrimination to be attenuated. Experience has shown that, while very fine discrimination may be achieved on model data, real data, with their variable amplitudes and waveforms and their additive noise, demand at least a 30-ms moveout from near to far trace to be effective. Also, sharp cut-offs in the transform domain may produce artifacts as a result of Gibb's phenomenon (Hampson, 1986).

2.4 Frequency-wavenumber (*f-k*) attenuation

Waves traveling upward from subsurface reflective strata continue propagating after they are recorded by receivers as primary reflections. When a sharp velocity discontinuity exists above the receivers, the waves are then reflected back, and are once more recorded by the same receivers but as downgoing waves. This phenomenon is known as the receiver ghost (Aytun, 1999).

In marine surveys, receiver ghosts can not be avoided because the receivers are placed at a depth below the free surface. For streamer data, because streamers are towed at shallow depths (typically 8 to 10 m) in traditional marine surveys, the receiver ghost notches in streamer data appear at frequencies at or beyond the top end of the usual seismic band and, hence, are not considered a severe problem (Dragoset and Barr, 1994). But for OBS data, if we look at the *f-k* responses of receiver ghost and primaries in an OBS record in the *f-k* domain, we can see the null frequencies are caused by the time differences between the primary and the ghost arrivals, and the variation of the null-frequency points with the spatial frequency is observed very clearly on *f-k* plots of synthetic data. These strong spectral features caused by the receiver ghost can be used to attenuate it.

2.4.1 Receiver ghost in *f-k* domain

A ghost appears in a trace as the addition of a delayed version of the primary reflections. The recorded signature is written (Aytun, 1999) as:

$$S(t) = R(t) + cR(t-\tau)\,, \tag{2.17}$$

where $S(t)$ is the trace with both primaries and ghost, $R(t)$ is the trace with primaries only, c is a coefficient such that $-1 \le c \le 1$, and τ is the traveltime difference between the direct arrival and the surface reflected arrival. For the vertical incidence situation:

$$\tau_0 = 2\frac{\Delta z}{\alpha_1}\,, \tag{2.18}$$

where α_1 is the velocity of water, $\Delta z = | z_r - z_0 |$ is the depth of receivers from the surface. z_r is the level at which the receivers are located, and z_0 is the level of the free surface.

For different receivers, we have:

$$\tau_n = 2\frac{\Delta z_n}{\alpha_1} = \tau_0 \cos\theta_n, \tag{2.19}$$

where θ_n are incidence angle of the respective receivers. The resonant frequencies are:

$$f_n = (2n-1)\frac{\alpha_1}{4\Delta z} , \tag{2.20}$$

and the frequency interval:

$$\Delta f = f_n - f_{n-1} = \frac{\alpha_1}{2\Delta z} . \tag{2.21}$$

The null-frequency points occur at $1/\tau$, $2/\tau$, …, m/τ. The loci of null frequencies and their harmonics with respect to k_x is (Aytun, 1999):

$$f_{null} = \sqrt{k_x^2 \alpha_1^2 + m^2 f_0^2} , \tag{2.22}$$

where $1 \le m \le M \, (M = f_{Nyguist} / f_0), f_0 = 1/\tau$.

The mathematical expression for the receiver ghost can be demonstrated in the *f*-*k* domain by the equation (Amundsen, 1993):

$$P(z_r) = [1 - \exp(2ik_z z_r)]U(z = z_r) , \tag{2.23}$$

where $P(z_r)$ is the recorded total pressure wavefield with ghost at level z_r, U (z = z_r) is the upgoing pressure wavefield at level z_r, $k_z = \sqrt{k^2 - k_x^2}$, $k = 2\pi f / \alpha_1$, f is the frequency.

Similarly, we also have the mathematical expression of the *n*th-order receiver ghost in the *f*-*k* domain:

$$P(z_r) = \{1 - \exp(2ik_z z_r) + \exp(4ik_z z_r) - ... + (-1)^n \exp(2nik_z z_r)\}U(z = z_r). \quad (2.24)$$

2.4.2 Deghosting in *f-k* domain

To remove the receiver ghost in the *f-k* domain, equation (2.23) is inverted. By doing this, the upgoing wavefield is extraplorated to z_0, that is,

$$U(z = z_0) = P(z_r)\frac{\exp(ik_z z_r)}{1 - \exp(2ik_z z_r)}, \quad (2.25)$$

as given by Amundsen (1993).

Also, inverting equation (2.24), we get the expression for removing the *n*th-order receiver ghost in the *f-k* domain.

2.4.3 Synthetic data example

To illustrate the above analysis, a model simulating a water-bottom reflection in marine data was generated with the parameters set as $\Delta z = 200$ m, $\alpha_1 = 1500$ m/s. In this model, only the effect of the water reverberation itself is considered; we have not considered the effect of the water layer on deep subsurface reflections.

The model of the primary reflection is shown in Figure 2.23; the modeled seismic record with primary and ghost is shown in Figure 2.24. The power spectrum of a trace of modeled primary is shown in Figure 2.25; the power spectrum of a trace of modeled primary and ghost is shown in Figure 2.26. The *f-k* response of modeled primary record is shown in Figure 2.27; and the *f-k* response of modeled primary and ghost record is shown in Figure 2.28. The effect of the ghost reflections can be seen by comparing Figures 2.25 and 2.26 and by comparing Figures 2.27 with 2.28.

From the equation (2.21), we know that the null-frequency points occur at $1/\tau$, $2/\tau$,…, m/τ. For this model, we have null-frequency points at 3.75, 7.5, and 11.25 Hz. The loci of the null frequencies are computed by equation (2.22) and plotted in Figure 2.29. The merged result of Figure 2.29 and Figure 2.28 is plotted in Figure 2.30.

Now, we want to demonstrate the application of equation (2.23). For the above model, in the *t*-*x* domain, the upgoing pressure wavefield at level z_r, $U(z = z_r)$, in equation (2.23) is observed as in Figure 2.23. By Fourier transformation in the *t* and *x* directions, the result $U(z = z_r)$ is shown in Figure 2.27. Taking this $U(z = z_r)$ as input, after using the equation (2.23), the total pressure wavefield with ghost at level z_r, $P(z_r)$, is obtained (Figure 2.31). Then applying a 2D inverse Fourier transformation, the ghost recorded in the *x*-*t* domain is obtained (Figure 2.32). Comparing with modeled primary and ghost (Figure 2.24), we can say the application of equation (2.23) is successful.

Next, we want to demonstrate the deghosting technique [equation (2.25)]. Taking the modeled primary and ghost in the *f*-*k* domain (Figure 2.28) as input, Figure 2.33 is the deghosted record by using equation (2.25), and this record in the *x*-*t* domain is obtained by inverse Fourier transform (Figure 2.34). Comparing the original upgoing wave record (Figure 2.23) with the deghosted record (Figure 2.34) in the *x*-*t* domain and the respective *f*-*k* responses (Figure 2.27 and Figure 2.33), we can conclude that the deghosting technique can be applied successfully in the *f*-*k* domain.

2.4.4 Discussion

Based on a thorough study of the *f*-*k* response of the receiver ghost in a record, we can see that null frequencies are caused by the time differences between the primary and the ghost arrivals, and that they vary with the angle of incidence. It is concluded that the ghost arrivals inevitably generate null frequencies in the *f-k* domain, and that the loci of the each harmonic of the null frequencies is a different hyperbola but with a common pair of asymptotes. Therefore, it may be possible to decide whether ghost arrivals are recorded or not, simply by looking at the *f-k* responses of a record. The *f-k* response of a record may also be used for checking the effectiveness of the deghosting process (Aytun, 1999).

The theory study of the *f-k* response of the receiver ghost in a record illustrated in synthetic example only considers the effect of the water-column reverberation itself; the effect of the water layer on deep subsurface reflections is not considered. In practice, a seismic record can possibly includes many kinds of reflections and the features of the *f-k* response of the receiver ghost are no longer precisely distinguished. In any case, this method can be used together with other methods as a supplement.

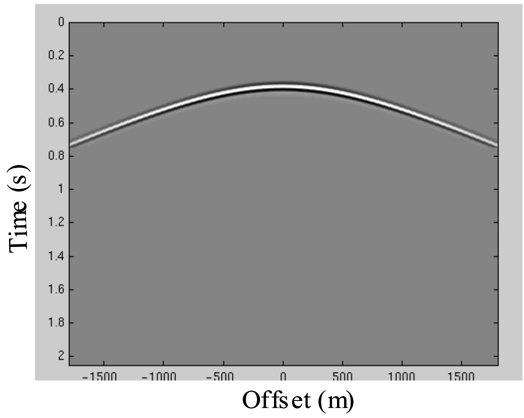

Figure 2.23. Modeled primary in the *t-x* domain.

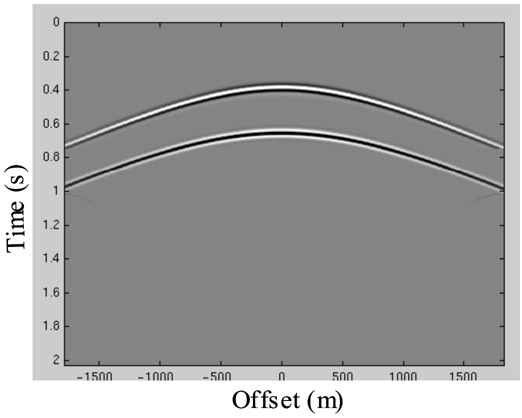

Figure 2.24. Modeled primary and ghost in the *t-x* domain.

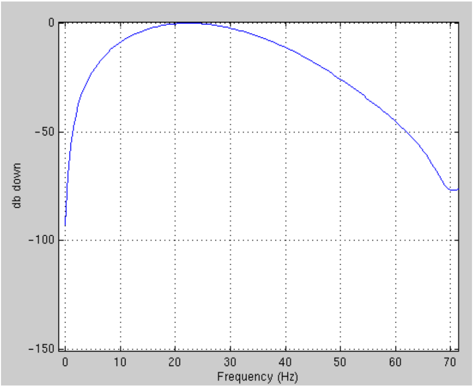

Figure 2.25. The power spectrum of a trace of modeled primary record.

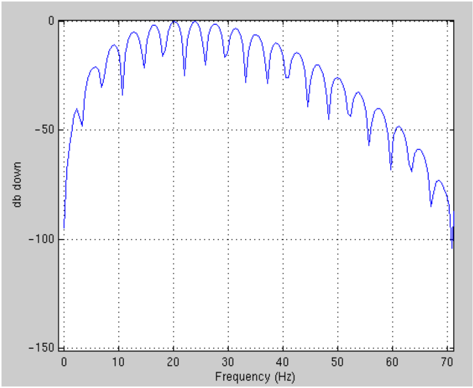

Figure 2.26. The power spectrum of a trace of modeled primary and ghost.

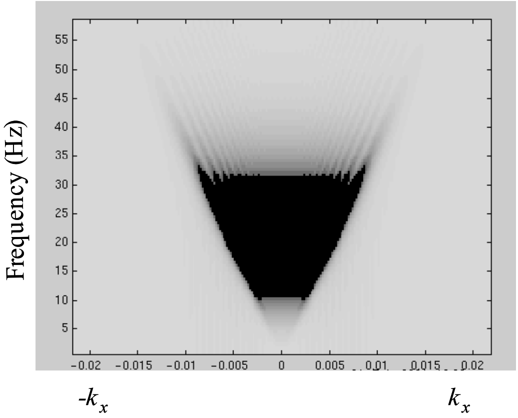

Figure 2.27. Modeled primary in the *f*-*k* domain.

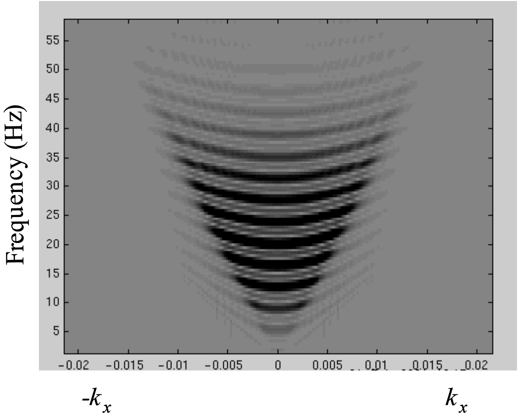

Figure 2.28. Modeled primary and ghost in the *f*-*k* domain.

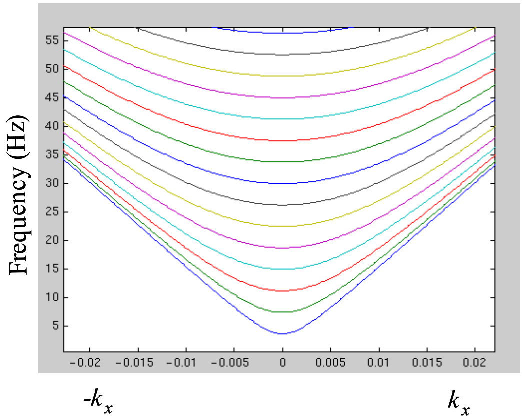

Figure 2.29. The loci of the null frequencies.

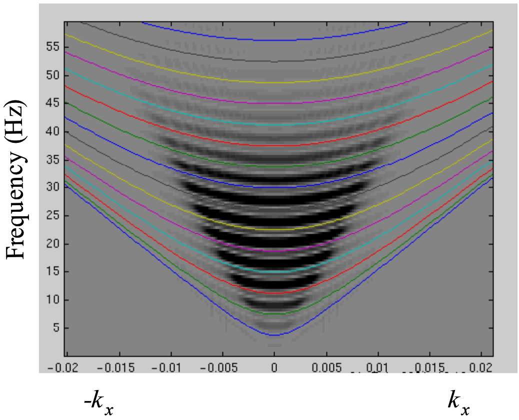

Figure 2.30. The loci of the null frequencies merged with primary and ghost in the *f*-*k* domain.

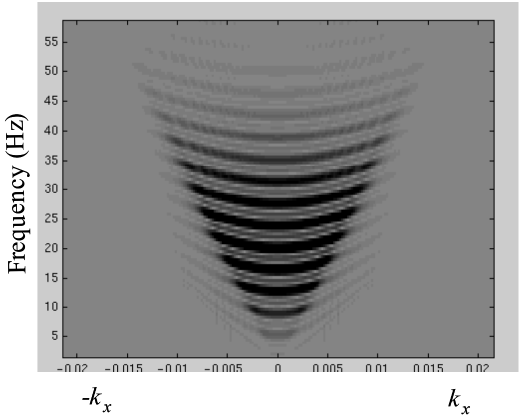

Figure 2.31. Primary and ghost in the *f*-*k* domain after applying equation (2.23) to the modeled primary record in *f*-*k* domain (Figure 2.27).

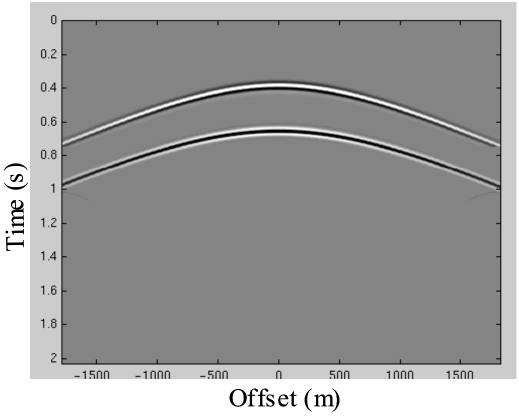

Figure 2.32. Primary and ghost in the *t*-*x* domain after applying 2D inverse Fourier transformation to Figure 2.31.

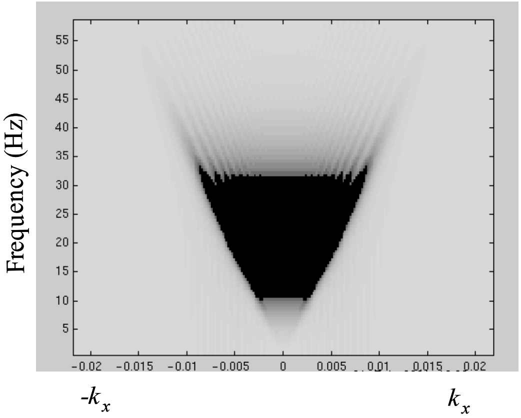

Figure 2.33. Primary in the *f-k* domain after applying equation (2.25) to the modeled primary and ghost record in the *f-k* domain (Figure 2.28).

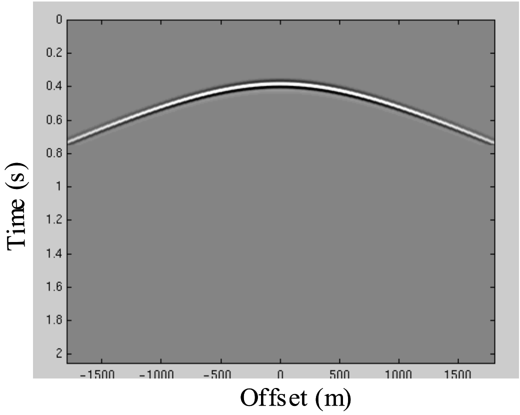

Figure 2.34. Primary in the *t-x* domain after applying 2D inverse Fourier transformation to Figure 2.33.

2.5 Summary

Most of above methods described above were developed early and applied to the common-shot gather for land data. They have different limitations, and the degree of success of these methods generally depends on how well the recorded data agree with the assumptions that are made about them. In OBS data, the acquisition geometry is different from that of land data. The OBS survey uses relatively few receivers and a great number of shots whereas a land survey uses a large number of receivers and few shots. For OBS data, we need to look at the common-receiver gather. A straightforward method for working on common-receiver gathers for multiple attenuation is the dual-sensor method.

Chapter 3: Dual-sensor summation

3.1 Introduction

According to the direction of arrivals at an OBS receiver, seismic events can be classified as downgoing and upgoing arrivals. Downgoing arrivals include the direct wave, subsequent water-column reverberations and receiver-side multiples (Figure 3.1), while the upgoing arrivals include all the primaries, source-side multiples and many of the interbed multiples (Figure 3.2).

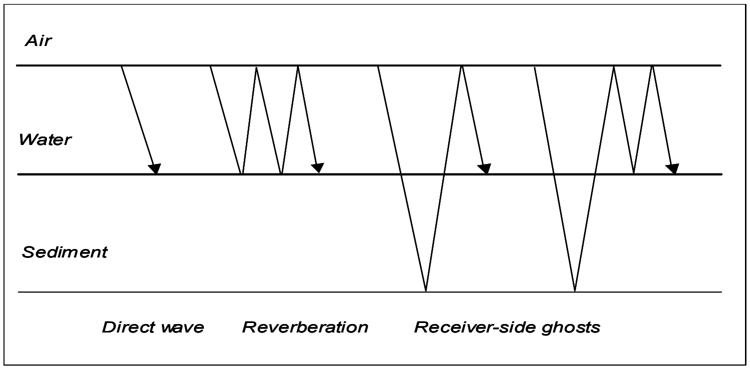

Figure 3.1. Examples of downgoing waves in OBS data.

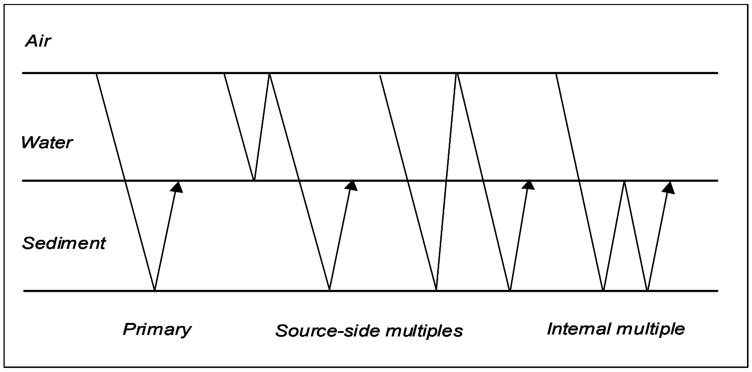

Figure 3.2. Examples of upgoing waves in OBS data.

The basic content of the dual-sensor method is, assuming the SEG recording-polarity standard has been followed (Brown et al., 2002), that upgoing P-wave arrivals will register with the same polarity on a hydrophone and vertical geophone, whereas, downgoing P-wave arrivals will register with the opposite polarity on the two instruments. This presents the theoretical opportunity to scale and sum the two types of gather, as described below, and eliminate the multiples and reinforce the primaries (Brown and Yan, 1999; Barr and Sanders, 1989). To achieve cancellation effectively, it is crucial to scale the geophone and hydrophone so as to match their amplitude and phase responses (Bale, 1998).

There are many methods of calculating the scaling factor in the literature on OBS techniques (e.g., Barr and Sanders, 1989; Dragoset and Barr, 1994; Paffenholz and Barr, 1995; Ball and Corrigan, 1996; Bale, 1998). Early work on summation of hydrophone and geophone to attenuate the receiver-side multiples came from Barr and Sanders (1989). They shoot the source array directly over each pair of pressure (hydrophone) and velocity (geophone) detectors in the water-bottom receiver modules and record direct arrivals to determine the required scaling factor for vertical-incidence reverberations. The scaling factor was taken as the ratio of the first-break amplitude of the hydrophone and geophone signals. A separate 'calibration' survey is used to measure the ocean-bottom reflectivity. According to Dragoset and Barr (1994), calibration shooting can add 10% or more to the cost of a survey. They present an autocorrelation method that extracts a scaling factor that best whitens the summed data.

The above methods for processing dual-sensor data assume that the recorded data are composed of noise-free signals recorded by ideal hydrophones and geophones, the latter being well coupled to the seafloor. Real seismic data are contaminated by source-side reverberation as well as both random and coherent noise (Ball and Corrigan, 1996). Ball and Corrigan provide a means of analyzing dual-sensor data in the presence of source-side multiples and noise differentially recorded on the geophone and hydrophone.

The detrimental effects of noise on this analysis can be minimized by stacking of correlations and using an indirect estimate of the geophone autocorrelation. The water-bottom reflection coefficient can be estimated by construction of a function having the property that it is unbiased by the effects of source-side multiples. The resulting reflection coefficient may be used to optimally weight the geophone and hydrophone so that receiver-side multiples can be attenuated.

In this chapter, three methods of calculating the scaling factor are addressed. A new method of estimating the scaling factor, based on cross-correlation of hydrophone and geophone data is presented. This method has been tested experimentally and compared to two other methods. Both synthetic data and real data results show: this method can effectively attenuate the downgoing waves without any assumption that hydrophone data and geophone data should be phase matched, and this method can be extended to larger offset.

3.2 Method Descriptions

3.2.1 Method I (Bale, 1998)

The theory of dual-sensor methods is based on the vertical-incidence situation without regard to angular dependence. According to Bale (1998), the estimation of the scaling factor is particularly sensitive to offset. He presents a method to use plane-wave decomposition to extend the method to larger offsets, both for the estimation of the scaling factor and for the summation itself. Based on wave theory, when a wave propagates at an angle of incidence θ (Figure 3.3), both the traveltime through the water layer and the amplitude on the vertical-velocity component are dependent on the cosine of the angle of incidence θ, which is simply related to the ray parameter, p, and the water velocity, α_1, by: $\cos\theta = \sqrt{1 - p^2\alpha_1^2}$.

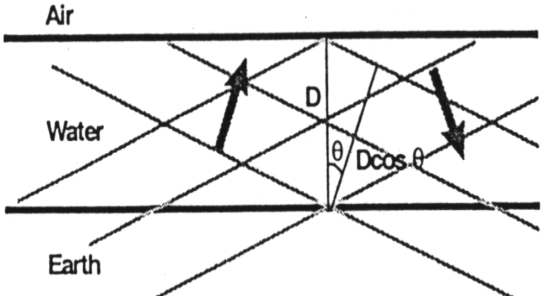

Figure 3.3. Plane-wave analysis (Bale, 1998).

In terms of this cosine, the relationship between the vertical component of velocity, V_Z and hydrophone component, W, after removal of the direct wave, was given by Amundsen (1993):

$$\{1+\exp[i\omega(2D/\alpha_1)\cos\theta]\}V_z = \{1-\exp[i\omega(2D/\alpha_1)\cos\theta]\}\frac{\cos\theta}{\rho\alpha_1}W, \tag{3.1}$$

where ρ is density of water. Theoretically, from the above equation, we can get the scaling function for the vertical geophone, V_Z, and hydrophone component, W. Then the summation of the two components should give the upgoing wavefield. In practice, due to imperfect geophone coupling and instrument sensitivity, the equation above can not be satisfied. Instead, we choose the λ that minimizes the objective function:

$$S = (1+z)V_z - \lambda(1-z)W\cos\theta, \tag{3.2}$$

where, $z = \exp[i\omega(2D/\alpha_1)\cos\theta]$. Then, the upgoing wavefield can be obtained by (Bale, 1998):

$$\begin{aligned} U_w &= \frac{1}{2}[W + (\frac{1+r}{1-r})\frac{V_z}{\lambda\cos\theta}], \\ U_{V_z} &= \frac{1}{2}[V_z + \lambda\cos\theta(\frac{1-r}{1+r})W]. \end{aligned} \tag{3.3}$$

where r is water-bottom reflectivity coefficient.

After applying the above equations, the receiver-side multiples can be removed. This method can handle larger angles of incidence, but requires estimation of further parameters such as water-bottom reflection coefficient, etc. It is also sensitive to the water depth (Bale, 1998).

3.2.2 Method II (R. J. Brown, personal communication)

If we only consider the vertical incidence situation or small incidence angle situation, and assuming the hydrophone and vertical geophone data are phase-matched, then the Method I (equation 3.3) can be simplified as:

$$
\begin{aligned}
U_W &= \frac{1}{2}[W + (\frac{1+r}{1-r})V_Z], \\
U_{V_z} &= \frac{1}{2}[V_Z + (\frac{1-r}{1+r})W].
\end{aligned}
\tag{3.4}
$$

According to Barr and Sanders (1989), the sandy water-bottom reflection coefficient, *r*, is remarkably stable between normal incidence and critical angle. A plot of the ratio $\frac{1+r}{1-r}$ is shown in Figure 3.4 for a normal, sandy water bottom characterized by a vertical-incidence reflection coefficient of 0.32 and a P_wave velocity of 1695 m/s.

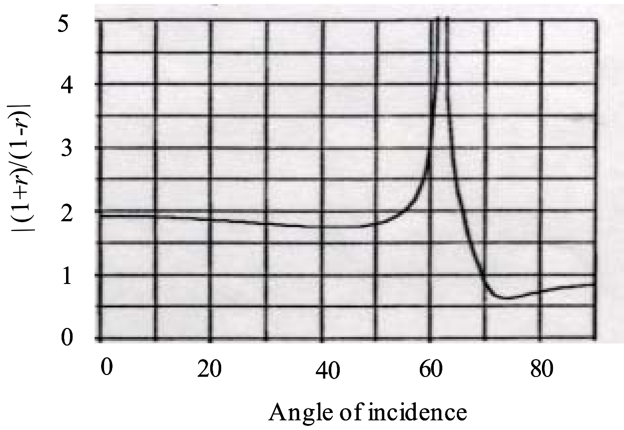

Figure 3.4. $\frac{1+r}{1-r}$ stability between normal incidence and critical angle (after Barr and Sanders, 1989).

Since $\frac{1+r}{1-r}$ is remarkably stable, then the scaling relationship between geophone and hydrophone now is a simple scaling relationship. In this case, the up-going wavefield can be obtained in another way. Gidlow and Sonnier (2001) proposed a method based on the sign of the recorded amplitudes. Following the sign convention for the geophone data, they defined the upgoing movement of the vertical geophone as a positive number and the downgoing movement as a negative number. For the hydrophone data, they define every compression as a positive number, and every rarefaction as a negative number then, by combining the geophone vector response with the response of the hydrophone, the upgoing wavefields are identified and extracted from the recorded total wavefield. Using a similar strategy, Method II is introduced.

Since hydrophone data (W) and geophone data (V_z) have the same polarity for upgoing waves, but the opposite polarity for downgoing waves, the scaling factor can be determined by comparing their polarities. Therefore, if we calculate the values of this expression: $\frac{V_{z_i}}{|V_{z_i}|} \cdot \frac{W_i}{|W_i|}$, then for each pair of hydrophone trace and geophone trace, we can get a series of values, such as {-1,...-1,...1,...1,...-1,...-1,...1,...1}, where, the negative values (-1, ...-1...) correspond to the downgoing waves, while positive values (1,...1...) correspond to the upgoing waves. If the series of values is increased by 1 and then divided by 2, then they become {0,...0...1,...1...0,...0...1,...1...}, in which the values (0, 0..) correspond to the downgoing waves, while values (1,1...) correspond to the upgoing waves. Taking these values as a sort of filter, $f(t)$, to multiply the hydrophone data and geophone data respectively, then we get the upgoing wavefields:

$$U_z = f(t) \cdot V_z(t), \qquad U_w = f(t) \cdot W(t). \tag{3.5}$$

An important and critical assumption required for this method to work is that both the hydrophone and vertical geophone data are phase matched and have the same coupling and impulse response of the measuring devices. However, in practice, this assumption is usually severely violated, and therefore, the summation of hydrophone and scaled geophone traces may produce undesirable results.

3.2.3 Method III

Method II simply determines the scaling factor by comparing the polarities of hydrophone and vertical geophone on each pair of samples. Instead of comparing the polarity of each pair of samples, I present here a new method of calculating the crosscorrelation for each pair of traces, hydrophone and geophone data, in each window to determine the scaling factor. Using this method, the comparison can be done within a window. First the crosscorrelation in each window can be calculated using the following expression:

$$\Psi_{v_z w}(j) = \frac{\sum_{i=1}^{L} V_{z_i} W_{i+j}}{\sqrt{\sum_{i=1}^{L} V_{z_i}^2 \sum_{i=1}^{L} W_i^2}} \ . \tag{3.6}$$

where, $\Psi_{v_z w}(j)$ is the cross-correlation of hydrophone and geophone data in each boxcar window and L is the window length (less than the periodicity of the multiples). The increment between two consecutive windows can be chosen less than L (overlapping windows) or the same size as L (consecutive windows), and j is the lag number. For downgoing waves, the hydrophone and geophone polarities are opposite. If they are exactly phase-matched, the value of $\Psi_{v_z w}(j=0)$ should be –1. For upgoing waves, their polarities are the same. If they are exactly phase-matched, the value of $\Psi_{v_z w}(j=0)$ should be 1. If the hydrophone and geophone data are not phase-matched, the values of $\Psi_{v_z w}(j=0)$ are between –1 and 1. So, according to the values of cross-correlation, we can choose a threshold to determine the value of the scaling factor, F.

$$\begin{aligned} &F = 1 && \Psi_{v_z w}(j=0) > -0.3, \\ &F = 0.1 && \text{-}0.5 \le \Psi_{v_z w}(j=0) \le -0.3, \\ &F = 0.01 && \Psi_{v_z w}(j=0) < -0.5. \end{aligned} \tag{3.7a}$$

Then, we use the formulae:

$$U_{v_z} = F \cdot V_Z(t) \text{ and } U_W = F \cdot W(t) \tag{3.7b}$$

to obtain the upgoing wavefields. This method does not require that the hydrophone data and geophone data be exactly phase-matched.

3.3 Numerical example

3.3.1 Direct comparison

The three methods are tested on the same synthetic data. The model is 2D, with a 500-m water layer and two further reflectors at depths of 1250 m and 2050 m. The P-wave velocities of the three layers are 1500 m/s, 3000 m/s, and 4000 m/s, respectively.

Both hydrophone and vertical-geophone synthetic data (Figure 3.5) are generated by OSIRIS – Precise Seismic Modeling software. Note that primaries are present for events at approximately 0.83 and 1.23 s. They arrive with the same polarities and are relatively reinforced after application of all three methods. The downgoing reverberations are present for events at approximately 1.01 and 1.67 s. They arrive with opposite polarities and are attenuated. Also notice that multiples associated with primary reflections and arriving from above and below at approximately 1.5 and 1.9 s are attenuated on the hydrophone component after application of Method I. But for the vertical-geophone component, since these two contributions have opposite polarities, they are partly attenuated by destructive interference and tend to be stronger after applying Method I. For more detail, the first trace is taken from the hydrophone data and a comparison of the results by the three methods is shown in Figure 3.6. The whole hydrophone dataset and the comparative results of the three methods are shown in Figure 3.7. The first trace taken from the geophone data and comparative results of the three methods are shown in Figure 3.8. The whole geophone dataset and the comparative results of the three methods are shown in Figure 3.9.

After all the three methods have been applied, the multiples at approximately 1.5 and 1.9 s still exist, especially, in the results of Method II and Method III (Figure 3.7 and Figure 3.9). For attenuating these multiple events, a predictive deconvolution can be applied. Using the result of Method III in Figure 3.9 as the input data, we can calculate the period of these multiples (about 0.667 s) according to their propagation paths. Then a predictive deconvolution (predictive lag = 0.667 s) is applied. The deconvolution result is shown in Figure 3.10. We can see that the predictive deconvolution has effectively eliminated the multiple energy and significantly sharpened the primary reflectivity.

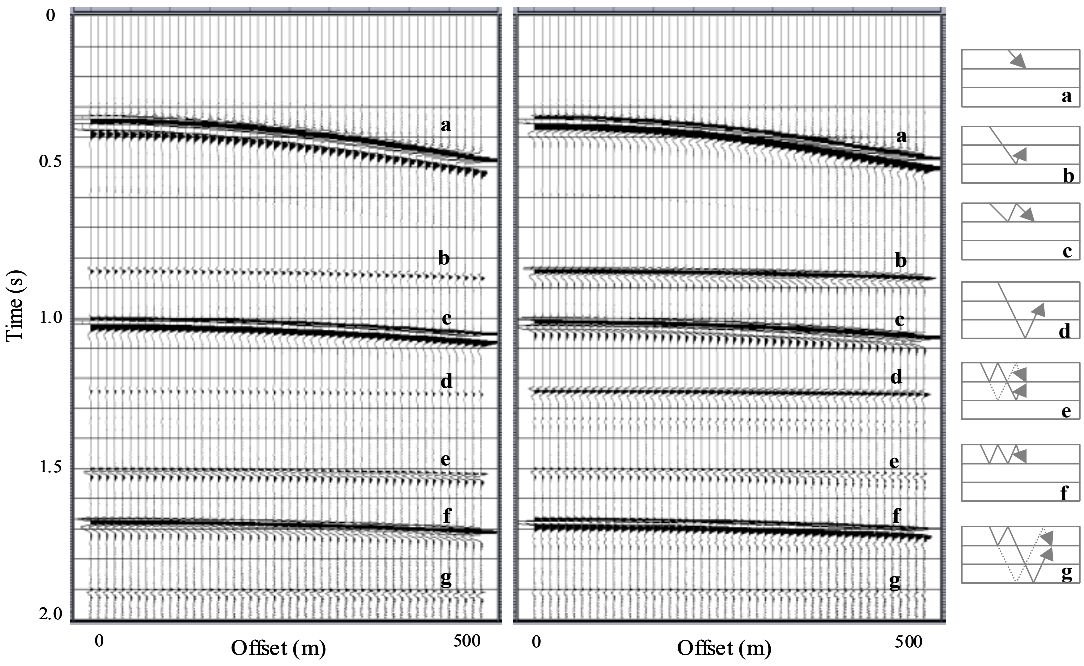

Figure 3.5. Synthetic hydrophone (left) and vertical geophone (right) data generated by OSIRIS.

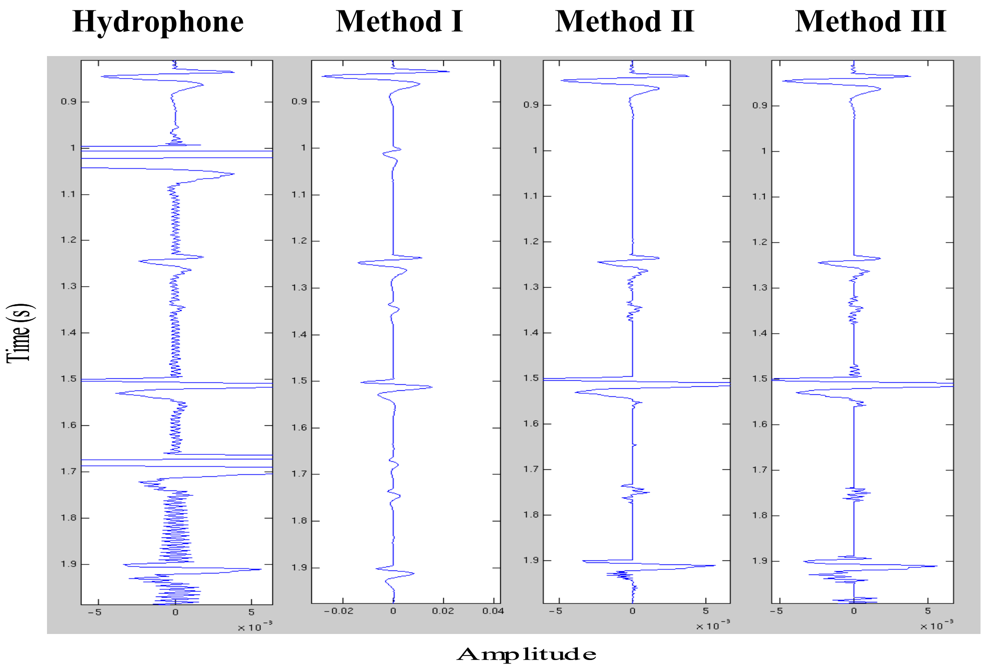

Figure 3.6. First trace of hydrophone data and comparative results of the three methods.

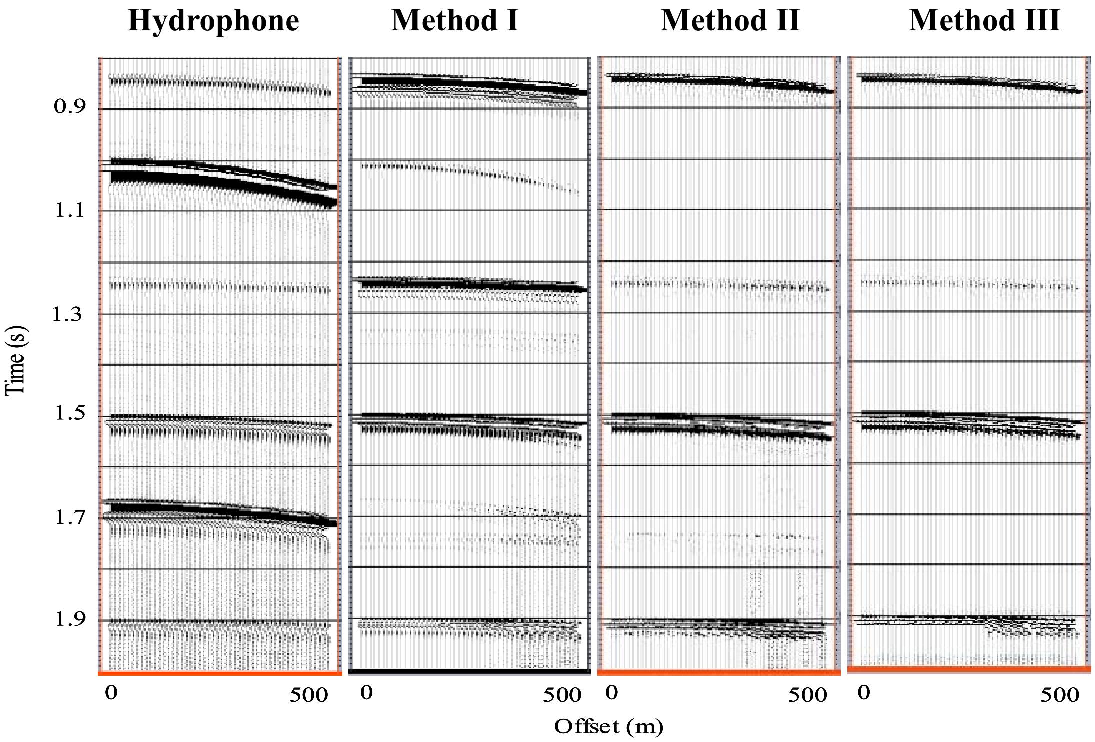

Figure 3.7. Hydrophone data and comparative results of the three methods.

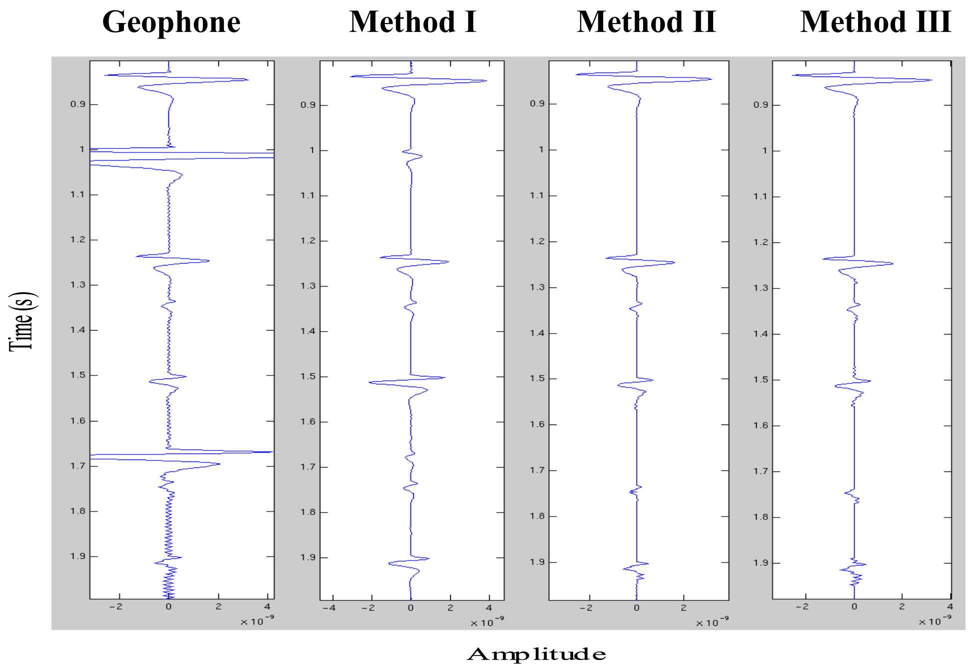

Figure 3.8. First trace of geophone data and comparative results of the three methods.

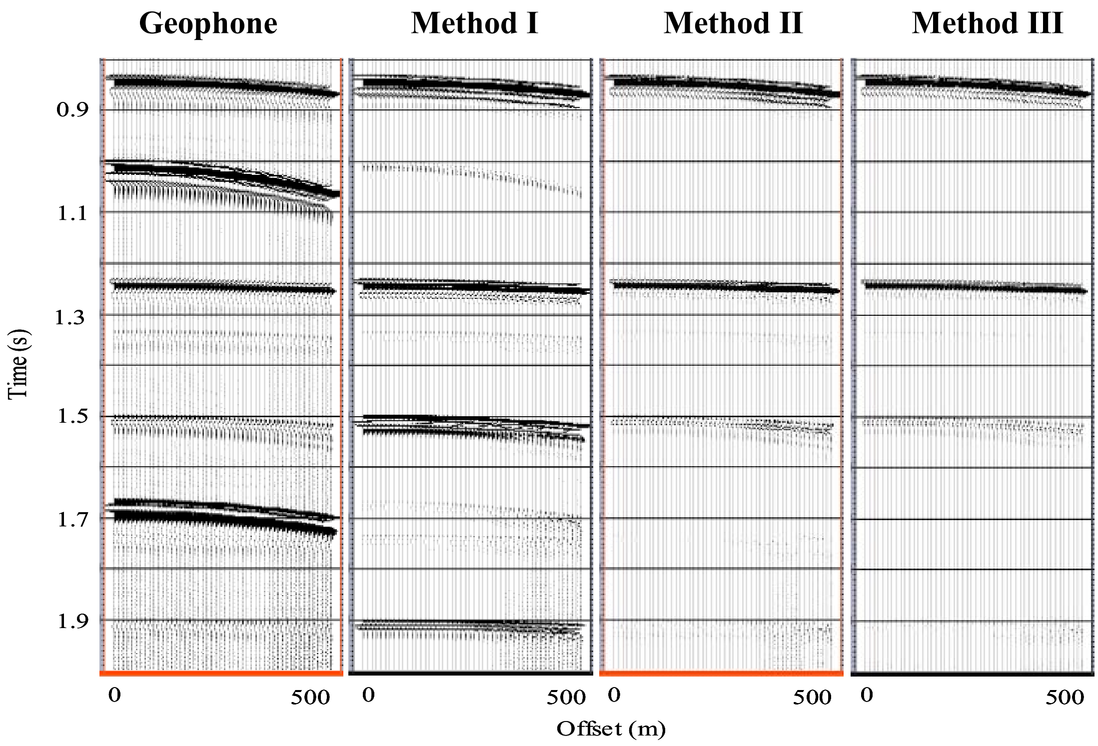

Figure 3.9. Geophone data and comparative results of the three methods.

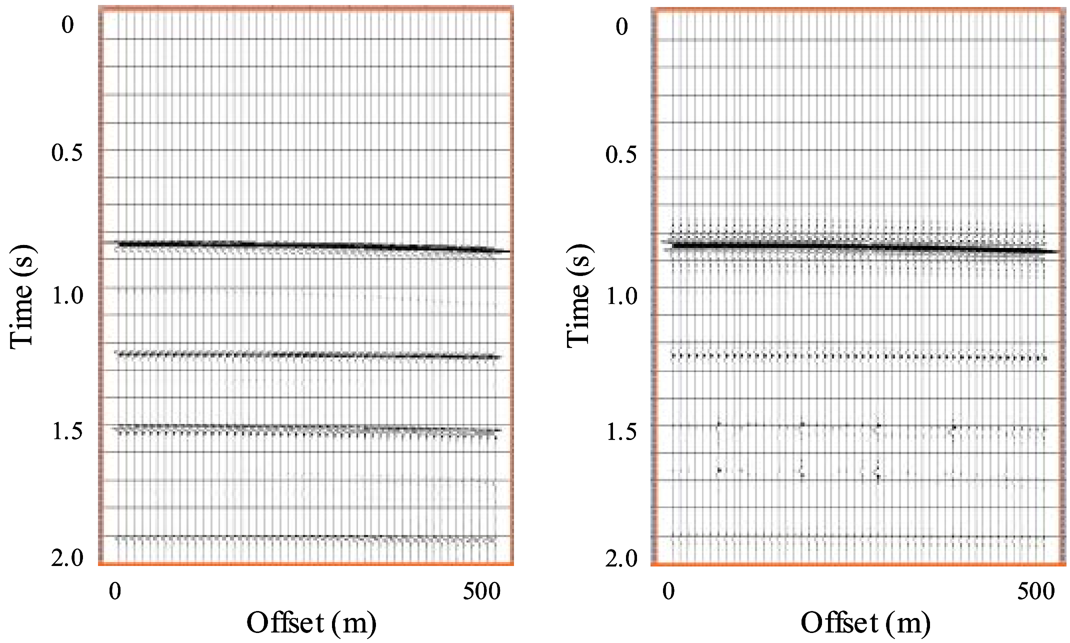

Figure 3.10. The data of Method III in Figure 3.9 (left), after application of the predictive deconvolution (right).

3.3.2 Adding random noise

To test the validity of the three methods on noisy data, I used the 'rnoise' function of Matlab to add normally distributed random noise ($S/N = 4$) to both hydrophone and vertical-geophone synthetic data (Figure 3.11). Compared with the multiples, the primary events are very weak. After adding noise, they can not be seen clearly in the hydrophone data at around 0.83 and 1.23 s, although, they are actually there.

The three methods still work reasonably well even though the data are contaminated by noise. The downgoing waves at about 1.01 and 1.67 s are attenuated and the upgoing waves at about 0.83 and 1.23 s are reinforced. At about 1.5 and 1.9 s, the multiples having both contributions from above and below are attenuated on hydrophone component by Method I, but they remain after Method II and Method III. This test shows that the three methods are not very sensitive to this level of noise.

The first trace of the hydrophone data and a comparison of results by the three methods are shown in Figure 3.12, and the entire dataset is shown in Figure 3.13. The first trace of geophone data and a comparison of results by the three methods is shown in Figure 3.14, and the entire dataset is shown in Figure 3.15.

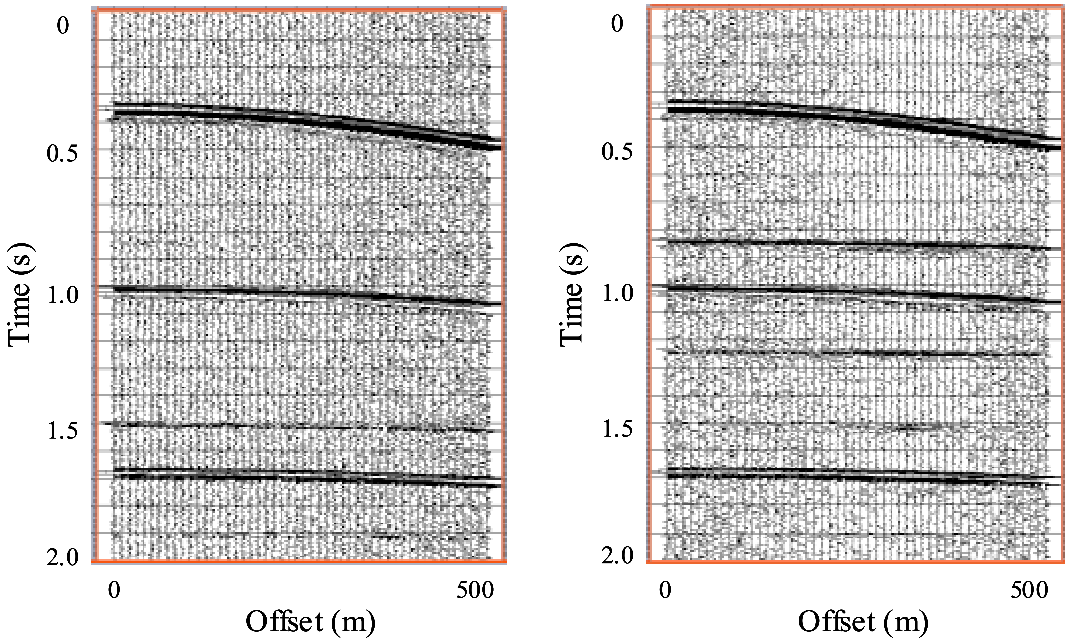

Figure 3.11. Hydrophone and geophone data with noise, $S/N = 4$.

3.3.3 Time shift

Since in practice the assumptions, e.g., that both the hydrophone and geophone data are phase-matched, are often violated, I now test the three methods when the hydrophone and geophone data are not phase-matched. I keep the geophone data the same, and make a small time shift of one sample, 8 ms, to the hydrophone data, so they are no longer phase-matched.

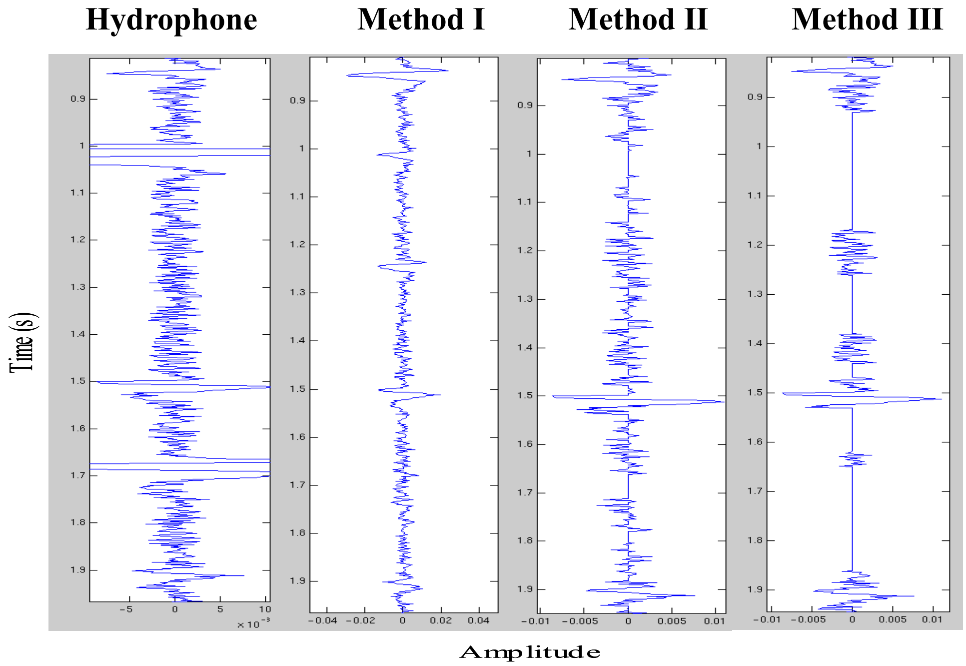

Figure 3.12. First trace of hydrophone data and comparative results of three methods for $S/N = 4$.

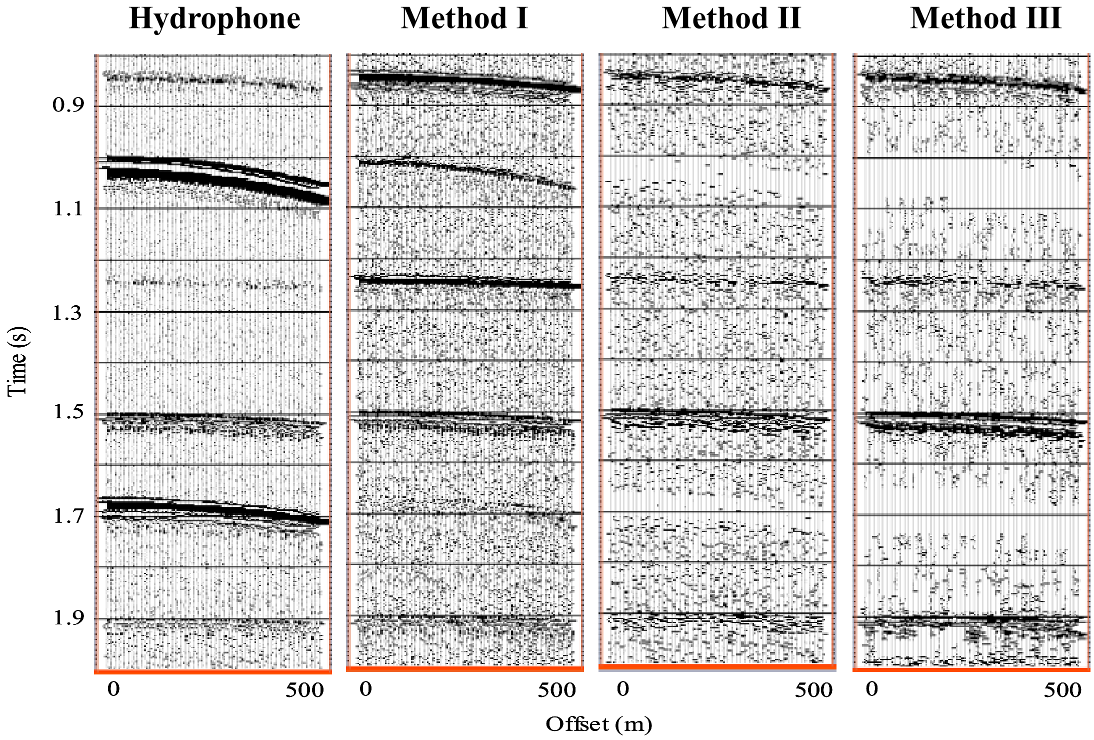

Figure 3.13. Hydrophone data and comparative results of the three methods for $S/N = 4$.

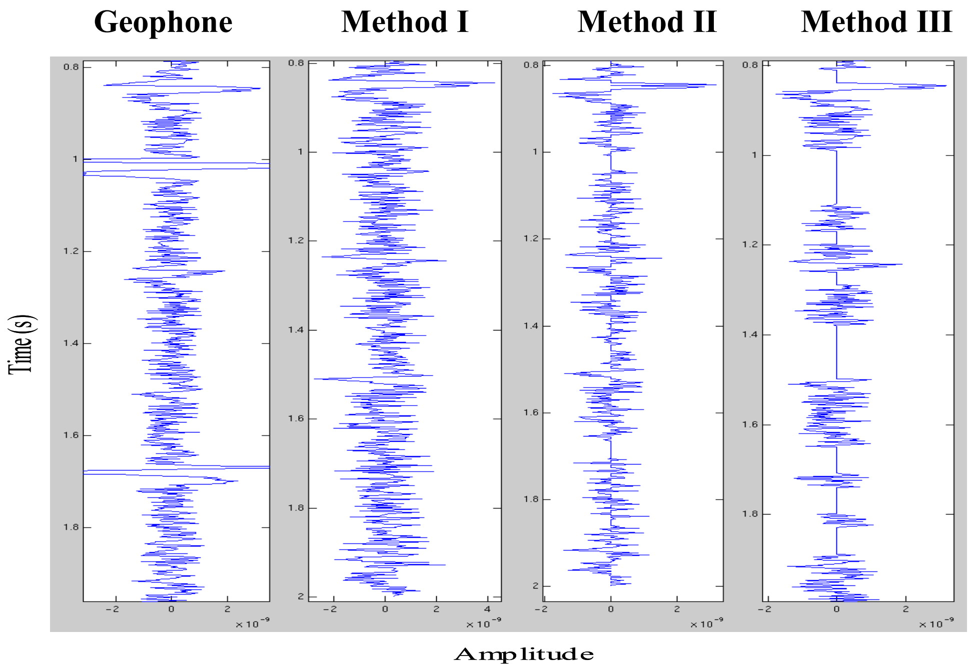

Figure 3.14. First trace of geophone data and comparative results of the three methods for $S/N = 4$.

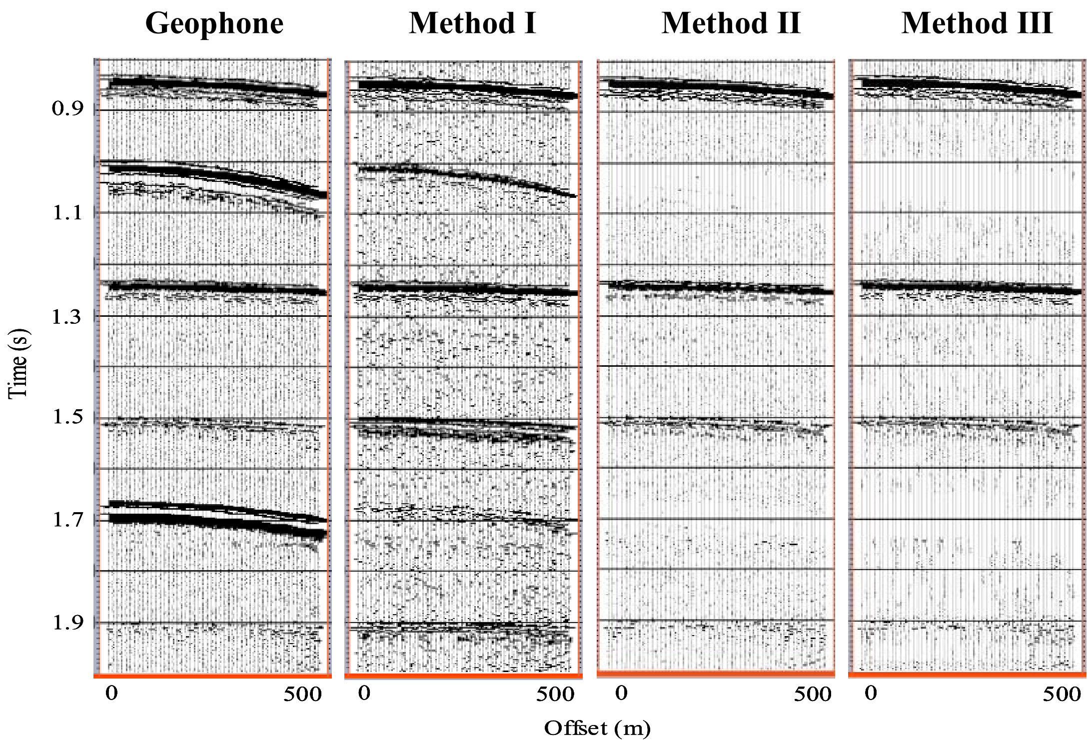

Figure 3.15. Geophone data and comparative results of the three methods for $S/N = 4$.

Figure 3.16 is the first trace taken from hydrophone data and a comparison of results by the three methods. The downgoing waves still exist in the results of Method I and Method II, but they are removed in the results of Method III. The multiples at about 1.5 and 1.9 s remain in the results of Method II and Method III, but they are attenuated in the hydrophone results of Method I. The whole dataset is shown in Figure 3.17. For the geophone data, the results are nearly the same (Figures 3.18 and 3.19).

3.4 Real data example

I next tested these three methods on a real receiver gather acquired over Mahogany Field in the Gulf of Mexico. The quality of data (Figure 3.20) is degraded by multiples. The water-column reverberation arriving after the direct arrival, and those multiples associated with primary reflections, contaminate the whole section. The water depth at the Mahogany field is about 120 m, so the water-column reverberation period is about 0.16 s. Based on the processing report provided by Sensor Geophysical Inc., the period of the multiples, and the arrival times of events, primary events are recognized at approximately 0.66 s and 0.96 s, and water-column reverberations after direct arrival at about 0.25 s, 0.41 s, and 0.57 s for zero offset. Notice also that the source-side multiple appears at about 1.26 s. The spectral analysis of the first traces of the two-component data is shown in Figure 3.21.

First, a bandpass filter (5-8-40-45 Hz) is applied to both hydrophone and geophone data. In addition, an automatic gain control (AGC) is applied to compensate the energy attenuation from the shallow to the deep subsurface and first breaks with high amplitude are muted (Figure 3.22). After these initial processing, the spectrum of the first trace of the hydrophone and geophone data is plotted again (Figure 3.23). Then this data is taken as the input data for three methods.

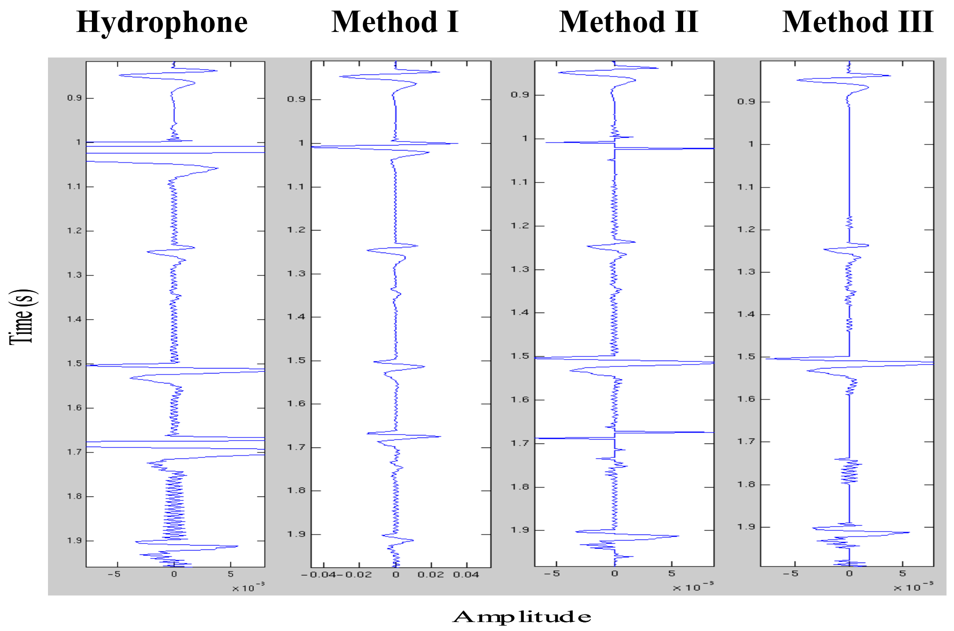

Figure 3.16. First trace of hydrophone data and comparative results of the three methods for 8-ms time shift.

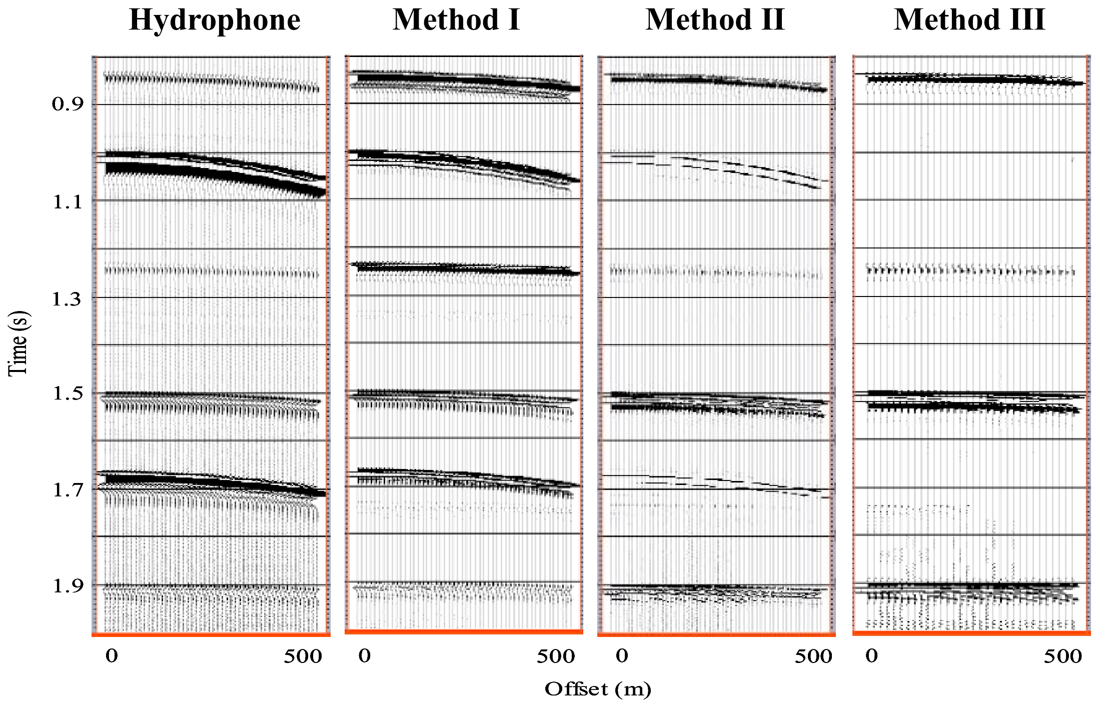

Figure 3.17. Hydrophone data and comparative results of the three methods for 8-ms time shift.

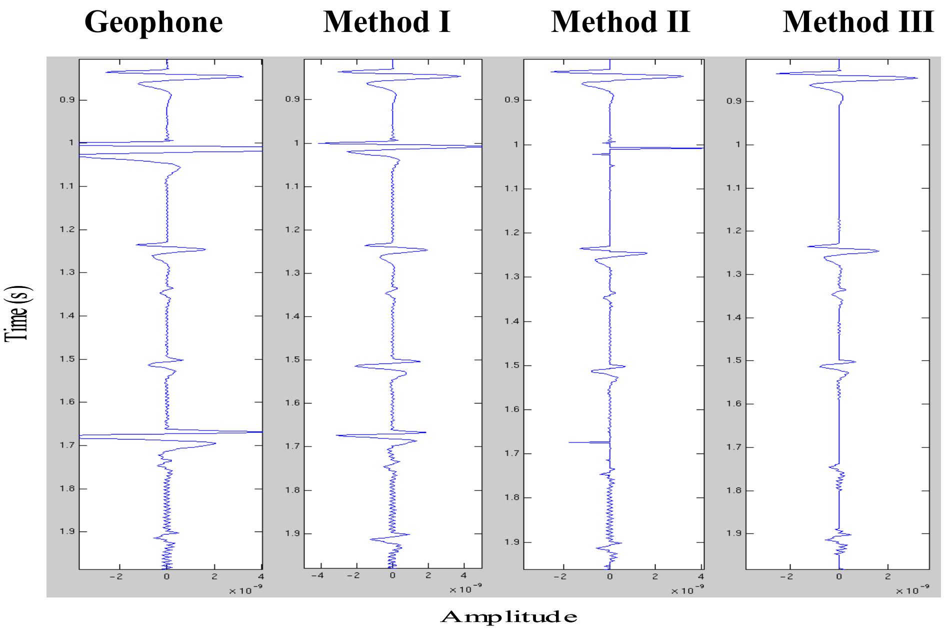

Figure 3.18. First trace of geophone data and comparative results of the three methods for 8-ms time shift.

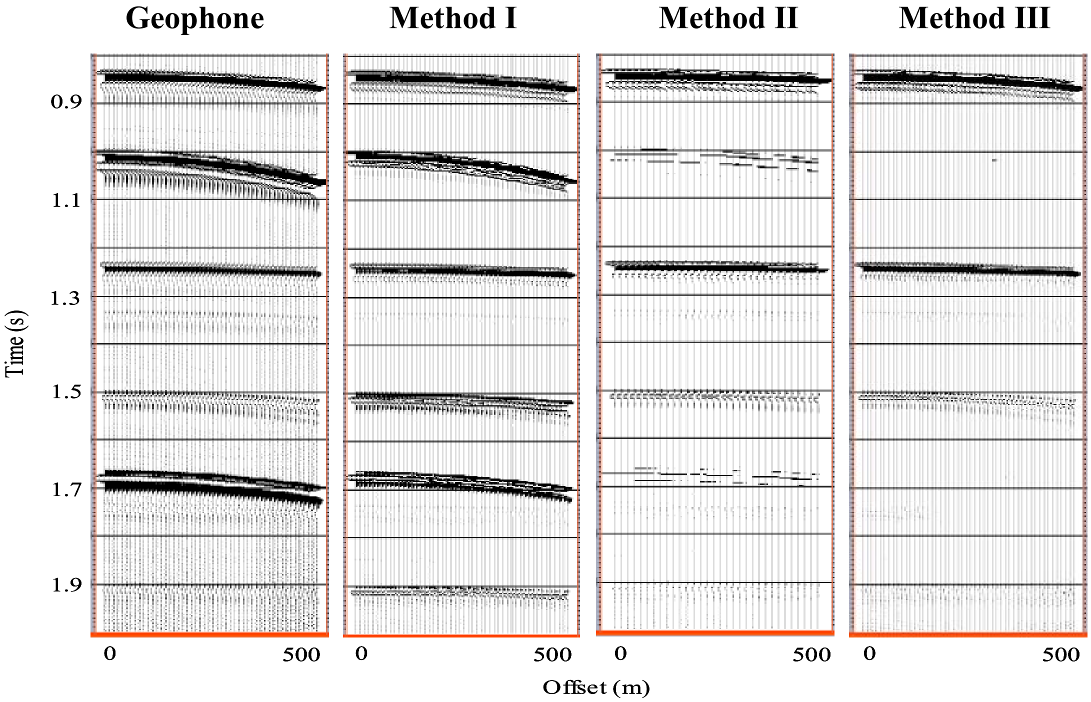

Figure 3.19. Geophone data and comparative results of the three methods for 8-ms time shift.

The results of three methods are shown in Figures 3.24, and 3.25. After the three methods are applied, the multiples at about 0.25 s, 0.41 s, and 0.57 s are attenuated and primaries at about 0.66 s and 0.96 s are relatively enhanced. In practice, due to measurement imperfection, the hydrophone and vertical-geophone data are usually phase mismatched. Since Method III is not sensitive to the phase matching requirement, the accomplish is a relatively better multiple suppression than Method I and Method II.

However, as expected, the source-side multiple energy (around 1.26 s) remains in the output (Figure 3.25, Method III). To eliminate this residual multiple energy, a predictive deconvolution is applied. The predictive lag of deconvolution used is 0.16 s. Result shows that this residual multiple energy is attenuated (Figure 3.26).

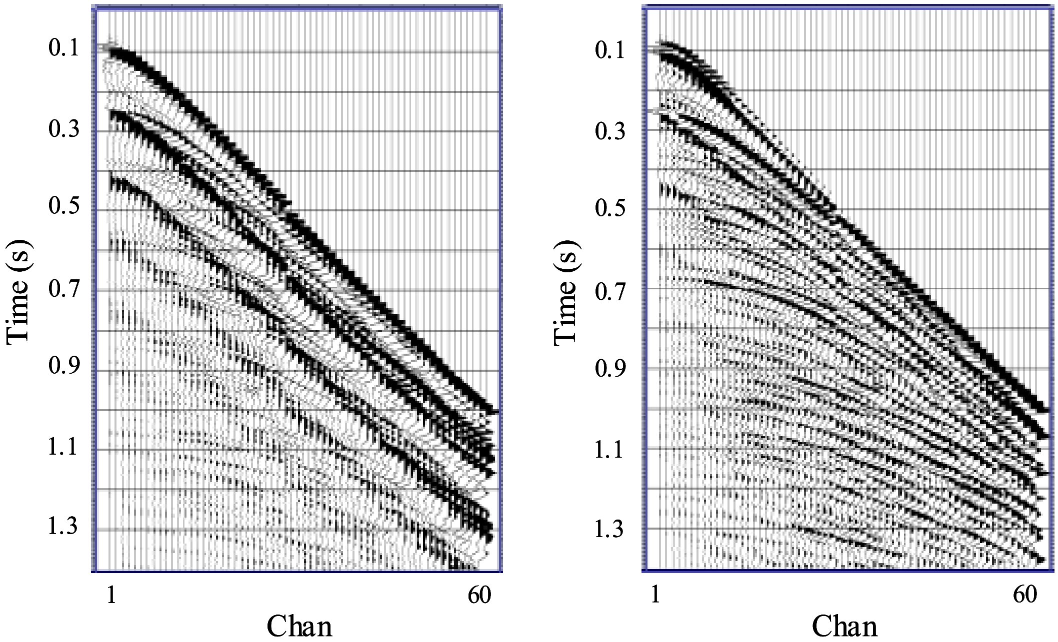

Figure 3.20. Mahogany hydrophone data (left) and geophone data (right).

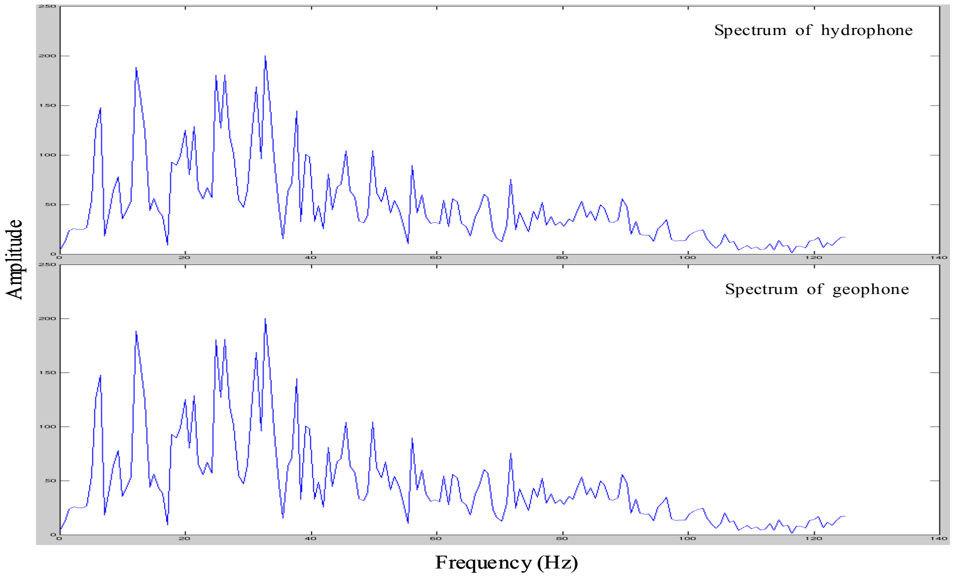

Figure 3.21. Spectrum of the first trace of the Mahogany hydrophone and geophone data.

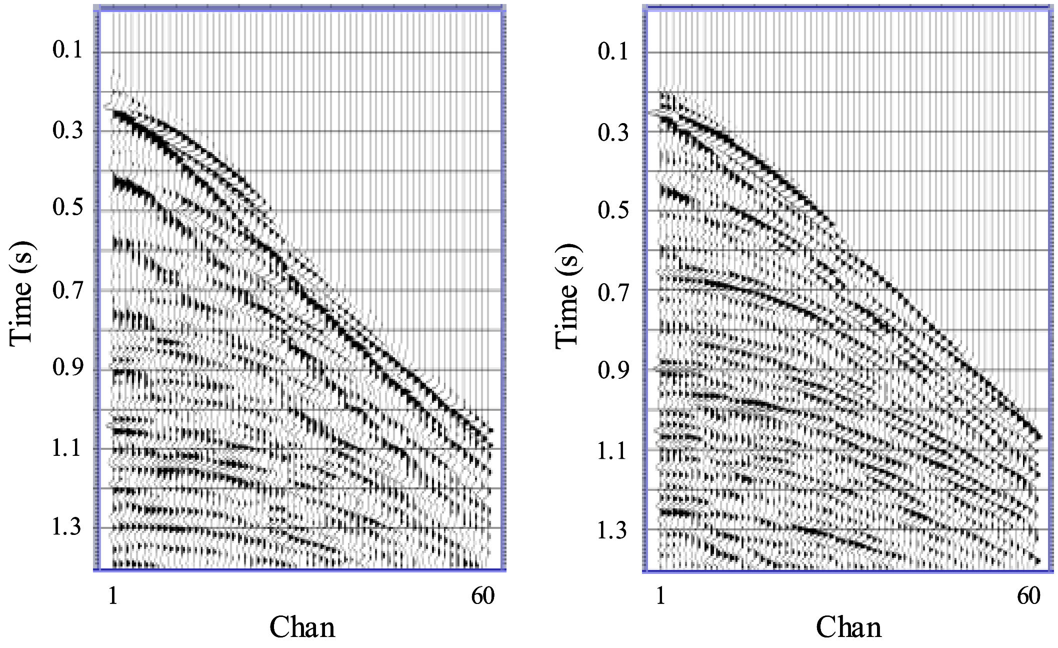

Figure 3.22. Mahogany hydrophone and geophone data after initial processing: bandpass filtering, AGC, and first-break mute.

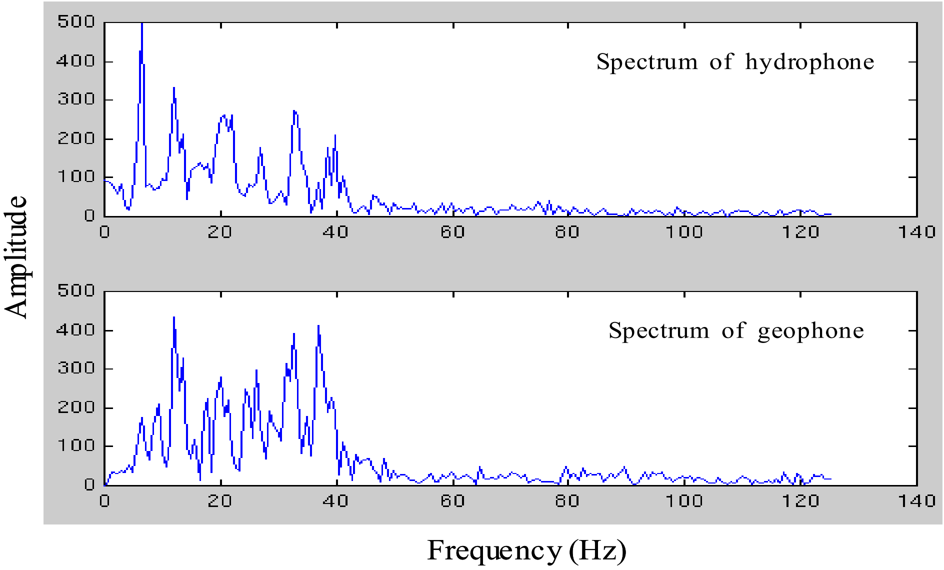

Figure 3.23. Spectrum of the first trace of the Mahogany hydrophone data and geophone data after initial processing.

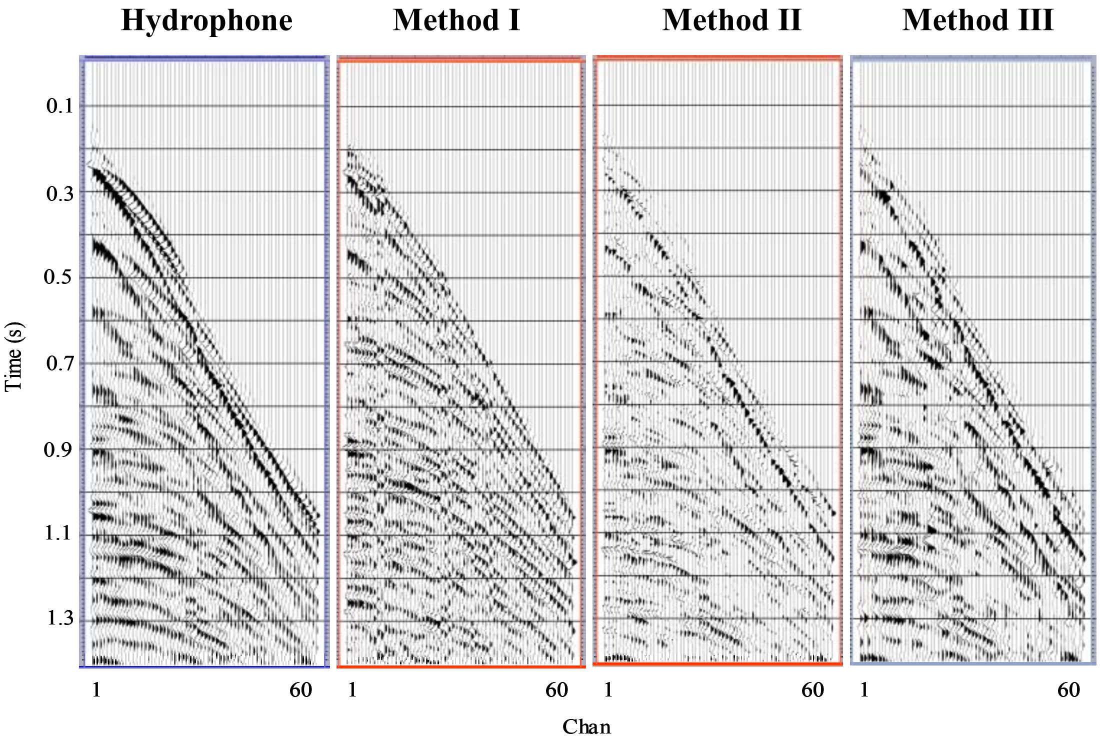

Figure 3.24. Mahogany hydrophone data and comparative results of the three methods.

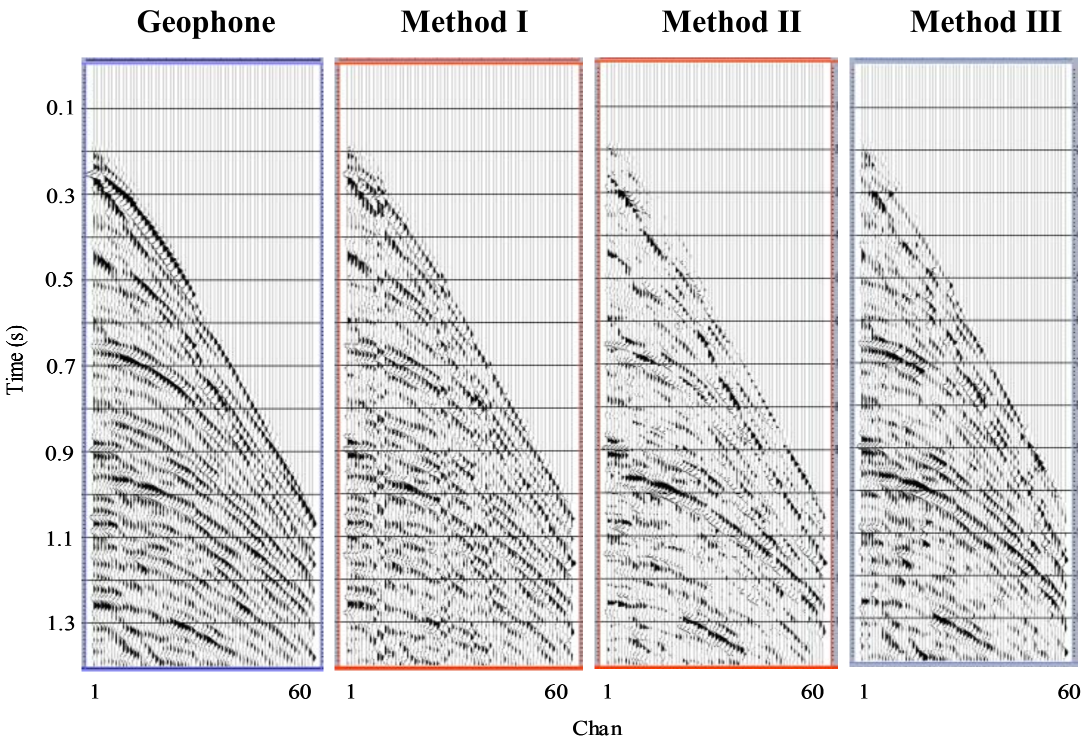

Figure 3.25. Mahogany geophone data and comparative results of the three methods.

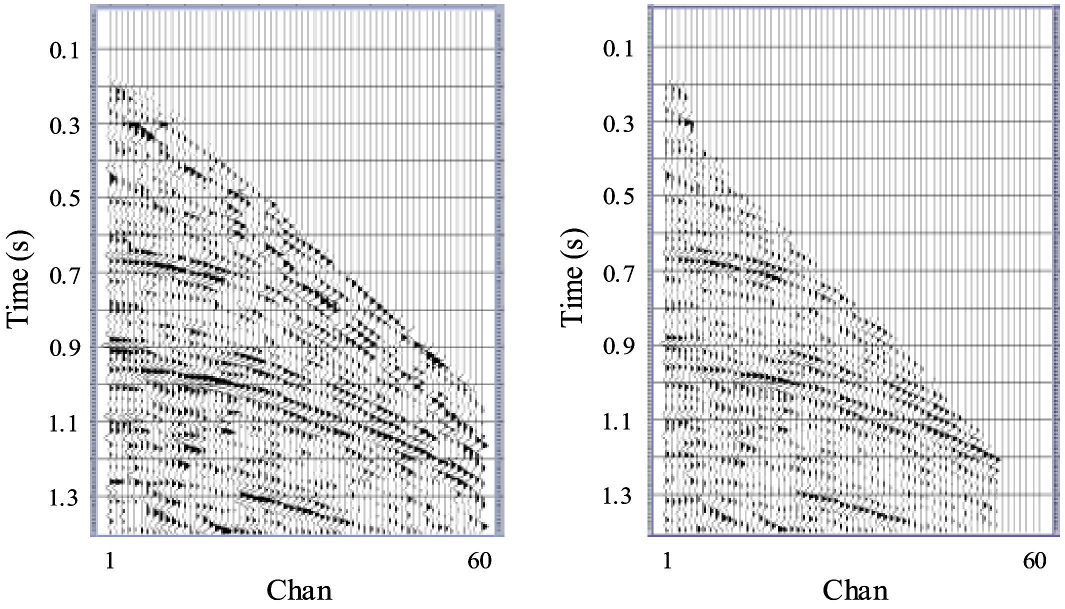

Figure 3.26. The data of Method III in Figure 3.25 (left) application of the predictive deconvolution (right).

3.5 Summary

The dual-sensor method is based on the fact that hydrophone and vertical geophone should record signals with the same polarity for upgoing waves, but with the opposite polarity for downgoing waves. So, with a proper scaling factor, the summation of these two data components recorded at the same station should be able to attenuate the downgoing waves. A new method of estimating the scaling factor, based on cross-correlation of hydrophone and geophone data, is reported. Experimental tests and comparison with two other methods have been performed on both synthetic data and field data. Test results show that all three methods perform very well when the hydrophone and geophone data are exactly phase-matched. When the hydrophone and geophone data are not exactly in phase, Method III performs the best of the three methods. For the water-column multiples that reverberate purely in the water-column and arrive from above as downgoing energy, Methods II and III work very well. For multiples that are associated with primary reflections from subseafloor horizons, Method I works best. None of the three methods is very sensitive to noise at the level applied (S/N=4).

The dual-sensor method is a simple and effective method for water-column multiple attenuation, it only utilizes two components: hydrophone and vertical geophone. In most actual OBS seismic surveys, three or four components are involved. This provides new possibilities for combining of components to attenuate the downgoing waves. As a result, the multicomponent wavefield-decomposition technique for water-column multiple attenuation has been developed.

Chapter 4: Multicomponent wavefield decomposition

4.1 Introduction

Multicomponent seafloor recording techniques have evolved continuously during the last decade and achieved promising results in the seismic exploration industry. Seafloor recording tools usually consist of a three-component (x, y, z) velocity-field measurement in the seafloor material by measure of geophones and a pressure measurement in the water by measure of hydrophone (Berg et al., 1994).

A serious problem in marine seismic data is that the measurements are contaminated by multiple reflections. Many schemes for combining different components to obtain the demultipled datasets have been presented in the literature. According to Osen et al. (1999), White (1965) pointed out, almost four decades ago, the possible usefulness to geophysical prospecting and oceanographic research of deploying a composite detector at the seafloor. His algorithm for attenuating water-column reverberations in the pressure recording was later reformulated and implemented by Barr and Sanders (1989), who designed a dual-sensor summation method to attenuate the downgoing waves.

Amundsen and Reitan (1994) presented an algorithm for decomposing multicomponent seafloor data generated by a marine source into upgoing and downgoing P- and S-waves. The algorithm is formulated and operated in the slowness-frequency domain using the axial symmetry, assuming that the fields are recorded along a line at the seafloor.

Osen et al. (1999) also gave the multicomponent wavefield-decomposition formulas derived for the more general case of having the records extending over an area of the sea bottom. The seafloor is assumed to be locally flat with constant medium parameters and Cartesian coordinate system is used. According to Osen et al. (1999), the essence of wavefield decomposition techniques is to combine the hydrophone with the horizontal- and vertical-geophone components to obtain the upgoing and downgoing wavefields after application of the appropriate decomposition operator to each of components.

Several researchers (e.g., Carvalho et al., 1991; Verschuur et al., 1998; Schalkwijk et al., 1999) have worked on wavefield decomposition and have combined multicomponent data in different ways to lead to different wavefield-decomposition formulae for various applications.

This chapter will give a comprehensive review and further investigation of wavefield-decomposition theory. The algorithm for attenuating the water-column multiples on each of three recorded components (hydrophone, vertical geophone, and inline geophone) just below the seafloor is implemented in *f*-*k* domain. Numerical data and real data examples are provided for illustration.

4.2 Wavefield-decomposition theory

Since the recorded wavefield is composed of the waves both in water recorded by hydrophones (just above the seafloor) and elastic media recorded by geophones (just below the seafloor), we can perform the wavefield decomposition in water (acoustic decomposition) and in the elastic media (elastic decomposition), respectively.

4.2.1 Acoustic decomposition just above the seafloor

In water, the upgoing and downgoing pressure wavefields can be computed from the hydrophone component and the vertical component of the particle velocity vector (Amundsen and Reitan, 1994) as:

$$U_P^W(z_1^-) = \frac{1}{2}[W(z_1^-) + \frac{\rho_1}{q_{\alpha_1}} V_z(z_1^+)], \tag{4.1}$$

and

$$D_P^W(z_1^-) = W(z_1^-) - U_P^W(z_1^-). \tag{4.2}$$

where q_{α_1} is vertical slowness in the water layer and $q_{\alpha_1} = \sqrt{(\alpha_1{}^{-2} - p^2)}$. α_1 is P-wave velocity in the water. p is horizontal slowness. ρ_1 is the density of water, z_1^- denotes a depth just above the sea floor, and z_1^+ denotes a depth just below the sea floor. W is the hydrophone component, and V_z is the vertical component of particle velocity. U_P^W is the upgoing P-wave pressure wavefield and D_P^W is the downgoing P-wave pressure wavefield, the subscript indicating the wave type and the superscript indicating the component type.

4.2.2 Elastic decomposition just below the seafloor

The elastic wave equation for homogenerous, isotropic media can be expressed in the form of a first-order ordinary differential equation in stress and velocity (Aki and Richards, 1980):

$$\frac{d}{dz}\mathbf{B} = -i\omega\mathbf{AB}, \tag{4.3}$$

where **B** is the vector that contains the stress and velocity variables across a plane elastic/elastic interface, and

$$\mathbf{B} = (V_z, S_x, S_y, S_z, V_x, V_y)^{\mathrm{T}}. \tag{4.4}$$

In equation (4.4), V_i are Fourier transformed components of particle velocity: V_x and V_y are horizontal components and V_z is the vertical component. S_z is the normal component of the traction in the solid, S_x and S_y are the shear components of the traction, z is depth, positive downward, ω is angular frequency. **A** is the system matrix defined as:

$$\mathbf{A} = \begin{bmatrix} 0 & \mathbf{A_1} \\ \mathbf{A_2} & 0 \end{bmatrix}, \tag{4.5}$$

where

$$\mathbf{A_1} = \begin{bmatrix} \dfrac{1}{\lambda+2\mu} & \dfrac{\lambda p_1}{\lambda+2\mu} & \dfrac{\lambda p_2}{\lambda+2\mu} \\ \dfrac{\lambda p_1}{\lambda+2\mu} & \rho - \dfrac{4\mu(\lambda+\mu)p_1^2}{\lambda+2\mu} - \mu p_2^2 & -\dfrac{\mu(3\lambda+2\mu)p_1 p_2}{\lambda+2\mu} \\ \dfrac{\lambda p_2}{\lambda+2\mu} & -\dfrac{\mu(3\lambda+2\mu)p_1 p_2}{\lambda+2\mu} & \rho - \dfrac{4\mu(\lambda+\mu)p_1^2}{\lambda+2\mu} - \mu p_1^2 \end{bmatrix} \tag{4.6}$$

and

$$\mathbf{A_2} = \begin{bmatrix} \rho & p_1 & p_2 \\ p_1 & \mu^{-1} & 0 \\ p_2 & 0 & \mu^{-1} \end{bmatrix}, \tag{4.7}$$

where λ and μ are the Lamè coefficients, p_x and p_y are horizontal slowness. The p_x and p_y have to satisfy the relation:

$$p^2 = p_x^2 + p_y^2 . \tag{4.8}$$

where p is slowness in elastic media. The wavefield separation can be obtained by eigendecomposition of the matrix **A**, i.e., $\mathbf{A} = \mathbf{L}^{-1}\,\Lambda\,\mathbf{L}$, where **L** is the matrix composed of eigenvectors of matrix **A** and Λ is the diagonal matrix composed of the eigenvalues of **A**. Then, equation (4.3) can be written as:

$$\frac{d}{dz}\mathbf{B} = -i\omega \mathbf{L}^{-1}\mathbf{\Lambda} \mathbf{L}\mathbf{B}. \tag{4.9}$$

It can be shown that Λ can be written as:

$$\Lambda = diag\left(q_P, q_{SV}, q_{SH}, -q_P, -q_{SV}, -q_{SH}\right). \tag{4.10}$$

The physical meaning of equation (4.10) is that eigenvalues q_P, q_{SV}, and q_{SH} correspond to the upgoing waves, whereas eigenvalues $-q_P$, $-q_{SV}$, and $-q_{SH}$ correspond to the downgoing waves. Therefore, equation (4.9) can be further decomposed into two equations that correspond to up- and downgoing waves, respectively, i.e.:

$$\frac{d}{dz}\mathbf{B}^U = -i\omega\mathbf{L}^{-1}\mathbf{\Lambda}_1\mathbf{LB} \quad \text{and} \quad \frac{d}{dz}\mathbf{B}^D = -i\omega\mathbf{L}^{-1}\mathbf{\Lambda}_2\mathbf{LB}, \tag{4.11}$$

where $\mathbf{\Lambda}_1 = diag\left(q_P, q_{SV}, q_{SH}, 0,0,0\right)$. $\mathbf{\Lambda}_2 = diag\left(0,0,0,-q_P, -q_{SV}, -q_{SH}\right)$. The superscripts U and D indicate upgoing and downgoing, respectively.

In order to solve equation (4.11), boundary conditions are needed. At the boundary between two solid media in welded contact, the components of particle velocity (or displacement) and traction are continuous over the boundary (e.g., Aki and Richards 1980). However, across the boundary between an inviscid fluid and a solid (e.g., the ocean bottom), only the vertical component of the particle-velocity is continuous; the horizontal components of particle velocity can be discontinuous, because that slip can occur parallel to the boundary. Further, the pressure in the fluid is equal to the vertical component of the traction in the solid, while the horizontal components of the traction in the solid vanish at the interface. So, at the seafloor, $z_1^+ = z_1 + \varepsilon$ and $z_1^- = z_1 - \varepsilon$ as $\varepsilon \to 0$, and we have:

$$\begin{gathered} S_x(z_1^+) = S_x(z_1^-) = 0; \; S_y(z_1^+) = S_y(z_1^-) = 0; \\ S_z(z_1^+) = W(z_1^-); \;\; V_z(z_1^+) = V_z(z_1^-). \end{gathered} \tag{4.12}$$

After applying the boundary conditions, we have the upgoing and downgoing P- and S-wave vertical traction components (Amundsen and Reitan, 1994):

$$U_P^{Sz}(z_1^+) = \frac{1}{2}(1-2p^2\beta_2^2)S_z(z_1^+) + \frac{\rho_2}{2q_{\alpha_2}}(1-2p^2\beta_2^2)^2 V_z(z_1^+) + ip\mu_2(1-2p^2\beta_2^2)V_r(z_1^+),$$

$$D_P^{Sz}(z_1^+) = \frac{1}{2}(1-2p^2\beta_2^2)S_z(z_1^+) - \frac{\rho_2}{2q_{\alpha_2}}(1-2p^2\beta_2^2)^2 V_z(z_1^+) + ip\mu_2(1-2p^2\beta_2^2)V_r(z_1^+),$$

$$U_S^{Sz}(z_1^+) = (p\beta_2)^2 S_z(z_1^+) + 2(p\beta_2)^2 \mu_2 q_{\beta_2} V_z(z_1^+) - ip\mu_2(1-2p^2\beta_2^2)V_r(z_1^+),$$

$$D_S^{Sz}(z_1^+) = (p\beta_2)^2 S_z(z_1^+) - 2(p\beta_2)^2 \mu_2 q_{\beta_2} V_z(z_1^+) - ip\mu_2(1-2p^2\beta_2^2)V_r(z_1^+).$$

(4.13)

where α_2, the P-wave velocity in the subsea solid, and β_2, the S-wave velocity in the subsea solid, are defined as:

$$\alpha_2 = \sqrt{\lambda_2 + 2\mu_2} \quad \text{and} \quad \beta_2 = \sqrt{\mu_2 / \rho_2}, \tag{4.14}$$

ρ_2 is the density in the subsea solid, λ_2 and μ_2 are the Lamè coefficients in the subsea solid. The vertical ray parameters are defined as:

$$q_{\alpha_2} = \sqrt{\alpha_2^{-2} - p^2}, \; q_{\beta_2} = \sqrt{\beta_2^{-2} - p^2}. \tag{4.15}$$

The upgoing and downgoing P- and S-wave vertical particle-velocity components (Amundsen and Reitan, 1994) are:

$$U_P^{V_z}(z_1^+) = -\frac{q_{\alpha_2}}{2\rho_2}S_z(z_1^+) - \frac{1}{2}(1-2p^2\beta_2^2)V_z(z_1^+) - ip\beta_2^2 q_{\alpha_2} V_r(z_1^+),$$

$$D_P^{V_z}(z_1^+) = -\frac{q_{\alpha_2}}{2\rho_2}S_z(z_1^+) + \frac{1}{2}(1-2p^2\beta_2^2)V_z(z_1^+) - ip\beta_2^2 q_{\alpha_2} V_r(z_1^+),$$

$$\begin{aligned}
U_S^{V_z}(z_1^+) &= -\frac{p^2}{2\rho_2 q_{\beta_2}} S_z(z_1^+) - (p\beta_2)^2 V_z(z_1^+) + \frac{ip}{q_{\beta_2}}(1-2p^2\beta_2^2)V_r(z_1^+), \\
D_S^{V_z}(z_1^+) &= -\frac{p^2}{2\rho_2 q_{\beta_2}} S_z(z_1^+) + (p\beta_2)^2 V_z(z_1^+) + \frac{ip}{q_{\beta_2}}(1-2p^2\beta_2^2)V_r(z_1^+).
\end{aligned} \tag{4.16}$$

The upgoing and downgoing P- and S-wave horizontal particle-velocity components (Amundsen and Reitan, 1994) are:

$$\begin{aligned}
U_P^{V_r}(z_1^+) &= -\frac{ip}{2\rho_2} S_z(z_1^+) - \frac{ip}{2q_{\alpha_2}}(1-2p^2\beta_2^2)V_z(z_1^+) + (p\beta_2)^2 V_r(z_1^+), \\
D_P^{V_r}(z_1^+) &= -\frac{ip}{2\rho_2} S_z(z_1^+) + \frac{ip}{2q_{\alpha_2}}(1-2p^2\beta_2^2)V_z(z_1^+) + (p\beta_2)^2 V_r(z_1^+), \\
U_S^{V_r}(z_1^+) &= \frac{ip}{2\rho_2} S_z(z_1^+) + ip\beta_2^2 q_{\beta_2} V_z(z_1^+) + \frac{1}{2}(1-2p^2\beta_2^2)V_r(z_1^+), \\
D_S^{V_r}(z_1^+) &= \frac{ip}{2\rho_2} S_z(z_1^+) - ip\beta_2^2 q_{\beta_2} V_z(z_1^+) + \frac{1}{2}(1-2p^2\beta_2^2)V_r(z_1^+).
\end{aligned} \tag{4.17}$$

The above decomposition procedure for separating multicomponent ocean-bottom data into up- and downgoing P and S waves is proposed by Amundsen and Reitan (1994). Their derivation is based on the assumption that the Earth consists of homogeneous plane layers and the axial symmetry is applied in cylindrical coordinates. Assuming that the fields are recorded along a line at the seafloor, they used the Fourier-Bessel transform for obtaining the decomposition formulae in the slowness domain. Following their investigation, Osen et al. (1999) revised the corresponding elastic decomposition formulae for each component for more practical application, with the assumption that the seafloor is locally flat, with constant medium parameters. The Fourier transform is applied in a Cartesian coordinate system.

4.3 Wavefield decomposition of each component

If Amundsen and Reitan's (1994) decomposition equations, (4.13), (4.16), and (4.17) are rewritten in Cartesian coordinates, we have the following decomposition equations for each of the components (hydrophone, vertical, inline and crossline geophones).

4.3.1 Hydrophone component

The upgoing and downgoing P- and S-wavefield decomposition formulae for the vertical traction component (after Amundsen and Reitan, 1994; Osen et al., 1999):

$$U_P^{S_z}(z_1^+) = \frac{1}{2}(1-2p^2\beta_2^2)S_z(z_1^+) + \frac{\rho_2}{2q_{\alpha_2}}(1-2p^2\beta_2^2)^2 V_z(z_1^+) - \rho_2\beta_2^2(1-2p^2\beta_2^2)(p_xV_x(z_1^+) + p_yV_y(z_1^+)),$$

$$D_P^{S_z}(z_1^+) = \frac{1}{2}(1-2p^2\beta_2^2)S_z(z_1^+) - \frac{\rho_2}{2q_{\alpha_2}}(1-2p^2\beta_2^2)^2 V_z(z_1^+) - \rho_2\beta_2^2(1-2p^2\beta_2^2)(p_xV_x(z_1^+) + p_yV_y(z_1^+)),$$

$$U_{SV}^{S_z}(z_1^+) = (p\beta_2)^2 S_z(z_1^+) + 2(p\beta_2)^2 \mu_2 q_{\beta_2} V_z(z_1^+) + \rho_2\beta_2^2(1-2p^2\beta_2^2)(p_xV_x(z_1^+) + p_yV_y(z_1^+)),$$

$$D_{SV}^{S_z}(z_1^+) = (p\beta_2)^2 S_z(z_1^+) - 2(p\beta_2)^2 \mu_2 q_{\beta_2} V_z(z_1^+) + \rho_2\beta_2^2(1-2p^2\beta_2^2)(p_xV_x(z_1^+) + p_yV_y(z_1^+)).$$

(4.18)

After applying one of the boundary conditions in equations (4.12): $S_z(z_1^+) = W(z_1^-)$, the upgoing wavefield (summing P- and S-waves) for the hydrophone component can be obtained using the formula below (Osen et al., 1999):

$$U^W(z_1^+) = \frac{1}{2}\{W(z_1^-) - \frac{\rho_2}{q_{\alpha_2}}[(1-2p^2\beta_2^2)^2 + 4p^2\beta_2^4 q_{\alpha_2} q_{\beta_2}]V_Z(z_1^+)\}. \quad (4.19)$$

4.3.2 Vertical-geophone component

The upgoing and downgoing P- and S-wavefield decomposition formulae for the vertical particle-velocity geophone component (after Amundsen and Reitan, 1994; Osen et al., 1999) are:

$$U_P^{V_z}(z_1^+) = -\frac{q_{\alpha_2}}{2\rho_2} S_z(z_1^+) - \frac{1}{2}(1-2p^2\beta_2^2)V_z(z_1^+) + \beta_2^2 q_{\alpha_2}(p_x V_x(z_1^+) + p_y V_y(z_1^+)),$$

$$D_P^{V_z}(z_1^+) = -\frac{q_{\alpha_2}}{2\rho_2} S_z(z_1^+) + \frac{1}{2}(1-2p^2\beta_2^2)V_z(z_1^+) + \beta_2^2 q_{\alpha_2}(p_x V_x(z_1^+) + p_y V_y(z_1^+)),$$

$$U_{SV}^{V_z}(z_1^+) = -\frac{p^2}{2\rho_2 q_{\beta_2}} S_z(z_1^+) - (p\beta_2)^2 V_z(z_1^+) - \frac{1}{2q_{\beta_2}}(1-2p^2\beta_2^2)(p_x V_x(z_1^+) + p_y V_y(z_1^+)),$$

$$D_{SV}^{V_z}(z_1^+) = -\frac{p^2}{2\rho_2 q_{\beta_2}} S_z(z_1^+) + (p\beta_2)^2 V_z(z_1^+) - \frac{1}{2q_{\beta_2}}(1-2p^2\beta_2^2)(p_x V_x(z_1^+) + p_y V_y(z_1^+)).$$

(4.20)

Using similar strategy for the pressure component, we can get the upgoing wavefield (summing P- and S-waves) for the vertical-geophone component as follows (Osen et al., 1999):

$$U^{V_z}(z_1^+) = \frac{1}{2}\{V_z(z_1^+) + [1-2\beta_2^2(p^2+q_{\alpha_2}q_{\beta_2})][\frac{p_x}{q_{\beta_2}}V_x(z_1^+) + \frac{p_y}{q_{\beta_2}}V_y(z_1^+)] - \frac{1}{\rho_2 q_{\beta_2}}(p^2+q_{\alpha_2}q_{\beta_2})W(z_1^-)\}.$$

(4.21)

4.3.3 Inline-geophone component

The upgoing and downgoing P- and S-wavefield decomposition formulae for the inline particle-velocity geophone component (after Amundsen and Reitan, 1994; Osen et al., 1999) are:

$$U_P^{V_x}(z_1^+)=\frac{p_x}{2\rho_2}S_z(z_1^+)+\frac{p_x}{2q_{\alpha_2}}(1-2p^2\beta_2^2)V_z(z_1^+)+(p_x\beta_2)^2(p_xV_x(z_1^+)+p_yV_y(z_1^+)),$$

$$D_P^{V_x}(z_1^+)=\frac{p_x}{2\rho_2}S_z(z_1^+)-\frac{p_x}{2q_{\alpha_2}}(1-2p^2\beta_2^2)V_z(z_1^+)+(p_x\beta_2)^2(p_xV_x(z_1^+)+p_yV_y(z_1^+)),$$

$$U_S^{V_x}(z_1^+)=-\frac{p_x}{2\rho_2}S_z(z_1^+)-p_x\beta_2^2q_{\beta_2}V_z(z_1^+)+\frac{p_x}{2p^2}(1-2p^2\beta_2^2)(p_xV_x(z_1^+)+p_yV_y(z_1^+)),$$

$$D_S^{V_x}(z_1^+)=-\frac{p_x}{2\rho_2}S_z(z_1^+)+p_x\beta_2^2q_{\beta_2}V_z(z_1^+)+\frac{p_x}{2p^2}(1-2p^2\beta_2^2)(p_xV_x(z_1^+)+p_yV_y(z_1^+)),$$

$$U_{SH}^{V_x}(z_1^+)=D_{SH}^{V_x}(z_1^+)=\frac{p_y}{2p^2}(p_yV_x(z_1^+)-p_xV_y(z_1^+)).$$

(4.22)

The upgoing wavefield (summing P and S waves) for the inline geophone component is given by (Osen et al., 1999):

$$U^{V_x}(z_1^+)=\frac{1}{2}\{V_x(z_1^+)-\frac{p_x}{q_{\alpha_2}}[1-2\beta_2{}^2(p^2+q_{\alpha_2}q_{\beta_2})]V_z(z_1^+)\}. \qquad (4.23)$$

4.3.4 Crossline-geophone component

The upgoing and downgoing P- and S-wavefield decomposition formulae for the crossline particle-velocity component (after Amundsen and Reitan, 1994; Osen et al., 1999) are:

$$U_P^{V_y}(z_1^+)=\frac{p_y}{2\rho_2}S_z(z_1^+)+\frac{p_y}{2q_{\alpha_2}}(1-2p^2\beta_2^2)V_z(z_1^+)+(p_y\beta_2)^2(p_xV_x(z_1^+)+p_yV_y(z_1^+)),$$

$$D_P^{V_y}(z_1^+)=\frac{p_y}{2\rho_2}S_z(z_1^+)-\frac{p_y}{2q_{\alpha_2}}(1-2p^2\beta_2^2)V_z(z_1^+)+(p_y\beta_2)^2(p_xV_x(z_1^+)+p_yV_y(z_1^+))$$

$$U_{SV}^{V_y}(z_1^+) = -\frac{p_y}{2\rho_2}S_z(z_1^+) - p_y\beta_2^2 q_{\beta_2}V_z(z_1^+) + \frac{p_y}{2p^2}(1-2p^2\beta_2^2)(p_xV_x(z_1^+) + p_yV_y(z_1^+)),$$

$$D_{SV}^{V_y}(z_1^+) = -\frac{p_y}{2\rho_2}S_z(z_1^+) + p_y\beta_2^2 q_{\beta_2}V_z(z_1^+) + \frac{p_y}{2p^2}(1-2p^2\beta_2^2)(p_xV_x(z_1^+) + p_yV_y(z_1^+)),$$

$$U_{SH}^{V_y}(z_1^+) = D_{SH}^{V_x}(z_1^+) = \frac{p_x}{2p^2}(p_xV_y(z_1^+) - p_xV_y(z_1^+)).$$

(4.24)

The upgoing wavefield (summing P and S waves) for crossline geophone component is (Osen et al., 1999):

$$U^{V_y}(z_1^+) = \frac{1}{2}\{V_y(z_1^+) - \frac{p_y}{q_{\alpha_2}}[1-2\beta_2{}^2(p^2 + q_{\alpha_2}q_{\beta_2})]V_z(z_1^+)\}. \tag{4.25}$$

After applying equations (4.19), (4.21), (4.23) and (4.25), the upgoing wavefields for the four components can be obtained separately.

Now we look at equation (4.19) again, noting that only hydrophone and vertical velocity components are involved in this equation. We can also see that the upgoing wavefield for hydrophone can be obtained just by combining the hydrophone and scaled vertical particle-velocity components. We can also see that the hydrophone wavefield and the vertical velocity wavefield can be expressed by each other. This demultiple scheme just uses a scaling relationship between the two components. If we rewrite this scaling relationship using the reflection coefficient of the seafloor, we have:

$$U^W(z_1^+) = \frac{1}{2}\{W(z_1^-) + \frac{\rho_1\alpha_1}{\cos\theta}\frac{(1+r)}{(1-r)}V_z(z_1^+)\}. \tag{4.26}$$

This is actually the dual-sensor method (Barr and Sanders, 1989). Therefore, we can take the dual-sensor method as a simple kind of wavefield-decomposition technique.

4.4 Source-side multiple suppression

After applying the wavefield-decomposition technique, given above, the upgoing wavefields for each of thecomponents can be obtained and downgoing multiples, such as the direct wave, receiver-side multiples and reverberations, are hopefully suppressed. However, simply extracting the upgoing wavefields cannot eliminate the upgoing source-side multiples. In the case of lateral homogeneity, source-side multiples will have raypaths that are equivalent in length to those of corresponding receiver-side multiples, so the two types of multiples are recorded simultaneously. In vertical-geophone data, these two contributions can have comparable energies but opposite polarities, which partly attenuates the multiples by destructive interference before any wavefield decomposition (Brown and Yan, 1999). Then a source-side free-surface multiple would be stronger on the upgoing vertical-geophone trace after decomposition than on the actual recorded trace. Such strong source-side multiples in the upgoing wavefield need to be suppressed by other means.

4.4.1 Source-side multiple identification

The schemes for attenuating the upgoing multiples have been presented by Carvalho et al., 1991; Berkhout, 1982; Weglein et al., 1997; Verschuur et al., 1998. Here, a simple way is adopted to achieve this, through a crosscorrelation technique.

In laterally homogeneous cases (uniform water depth), there exists certain receiver-side multiples with raypaths that are equivalent in length to those of corresponding source-side multiples on the vertical geophone records. These two types of multiples arrive from above and below, respectively, at the same time (Figures 4.1, 4.2).

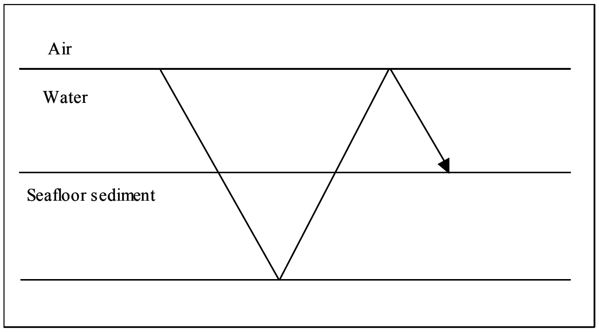

Figure 4.1. The raypath of one type of receiver-side multiples on the vertical-geophone records in laterally homogeneous medium.

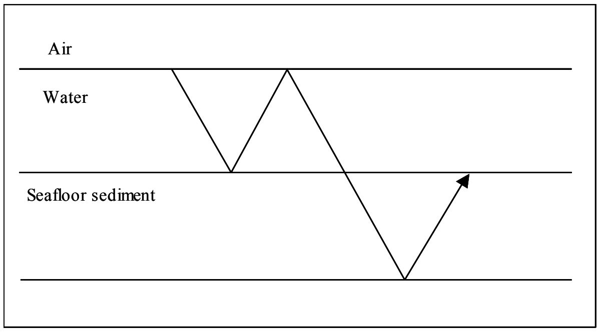

Figure 4.2. The raypath of corresponding source-side multiples on the vertical-geophone records in laterally homogeneous medium.

These two contributions have comparable energy but with opposite polarities on the vertical-component geophone. This case is similar to the dual-sensor method (Chapter 3) when hydrophone and vertical-geophone record downgoing waves with opposite polarity. This gives us the opportunity to use cross-correlation to identify the source-side multiple.

In some window, the cross-correlation function of the upgoing- wavefield data with the downgoing-wavefield data for the vertical- component geophone is calculated using the expression:

$$\psi_{UD}(j) = \frac{\sum_{i=1}^{L} U_i D_{i+j}}{\sqrt{\sum_{i=1}^{L} U_i^2 \sum_{i=1}^{L} D_i^2}}, \tag{4.27}$$

where, $\psi_{UD}(j)$ is the cross-correlation of the upgoing wavefield, U, with the downgoing wavefield, D, in each window. L is the length of the window, j is number of samples of a lag. In view of the identical arrival times (assuming lateral homogeneity) we focus our attention at zero lag. Then the cross-correlation coefficients at samples where the source-side multiples appear should approach –1, depending on how close to equality the amplitudes are of the upgoing and downgoing contributions to the multiple. Such large negative values is used as indicators of source-side multiple energy. The indicated sample positions of source-side multiples on the vertical geophone then are in turn used to identify the positions of multiples in the upgoing wavefields of all the components.

4.4.2 Source-side multiple elimination

Since the positions of the source-side multiples are identified on each of components, we can extract the source-side multiples from each of components, then subtract them from corresponding upgoing wavefields, respectively, to gain the upgoing wavefields without source-side multiples on each of components. However, when primary and multiple arrivals overlap, this simple subtraction would also eliminate some primary information. Also, the feature used for identifying the source-side multiples exist in laterally homogeneous cases including uniform water depth. In case of lateral heterogeneity, i.e., dipping seafloor and /or reflector, one would have to include lags other than zero in the analysis and it will be more difficult to identify the source-side multiples. Further consideration of lateral heterogeneity is beyond the scope of this thesis and represent a topic of further research.

4.5 Estimation of elastic parameters

Decomposition equations (4.19), (4.21), (4.23) and (4.25) all require an estimate of the elastic parameters of the seafloor materials. Estimation of seafloor parameters can be performed by amplitude-versus-offset (AVO) analysis (Amundsen and Reitan, 1995). Schalkwijk et al. (1999) also present a method of estimating the elastic parameters by a two-step wavefield decomposition method. In their scheme, instead of going from the measured data directly to the end result – up- and downgoing P and S waves – they use several intermediate decomposition results before coming to the final result and each intermediate result allows for the estimation of some unknown parameters.

Using a similar technique, Osen et al., (1999) performed the estimation of elastic parameter by applying equations (4.19), (4.21), (4.23) and (4.25) to the direct wave. Assuming that no upgoing waves interfere with the direct wave within a certain time window and offset range, they estimate the seafloor parameters from equations (4.19), (4.21), (4.23) and (4.25) by requiring that upgoing wavefield $U = 0$, e.g., for equation (4.19), when a single plane wave propagates directly from the source to the receiver in a direction perpendicular to a horizontal sea bottom, this equation can be written as:

$$U^W(z_1^+) = \frac{1}{2}[W(z_1^-) + \rho_2\alpha_2 V_z(z_1^+)]. \tag{4.28}$$

The scaling factor between the hydrophone and vertical geophone in equation (4.28) equals the P-wave impedance of the seafloor materials ($\rho_2\alpha_2$). By comparing the direct waves on the zero-offset traces on the hydrophone and vertical geophone, an estimate of the impedance, $\rho_2\alpha_2$, can be obtained.

To test this strategy, the hydrophone and vertical-geophone traces recorded at the acoustic/elastic interface was modeled in a model between a water layer and a semi-infinite half-space with elastic parameters α_2 = 2100 m/s, β_2 = 700 m/s and ρ_2 = 2098 kg/m^3 using ElMo, an elastic modelling program based on the phase-shift-cascade method (Silawongsawat and Margrave, 1998). The explosive point source was placed at 5-m depth and the thickness of the water was set to 500 m. When source depth is small compared to the water-layer thickness, the effect of the source ghost does not degrade the analysis (Osen et al., 1999).

Figure 4.3 shows the direct wave on the zero-offset hydrophone (*W*) trace, while the corresponding direct-wave arrival on the vertical velocity (V_z) trace is shown in Figure 4.4. For comparison, the vertical-geophone trace is plotted with reversed polarities.

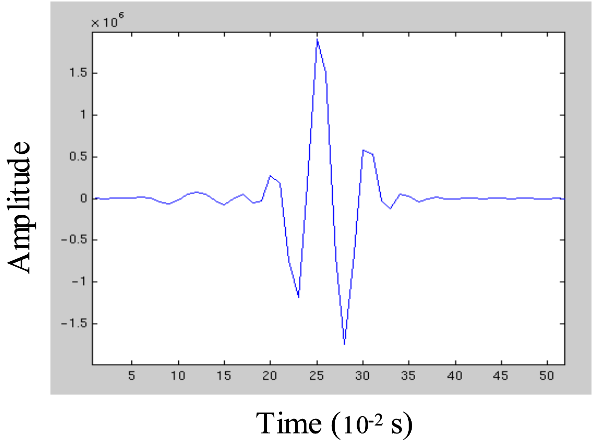

Figure 4.3. The zero-offset trace for the direct wave on the hydrophone.

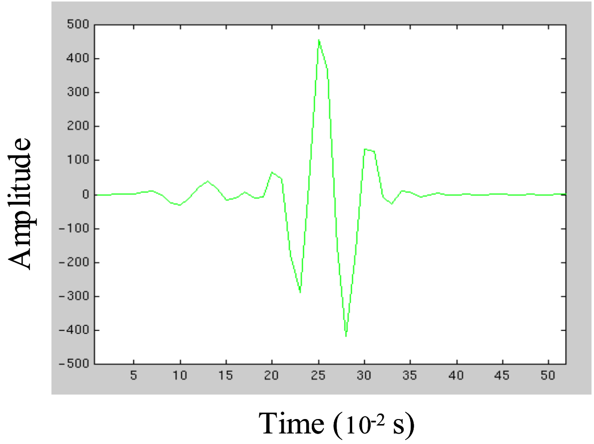

Figure 4.4. The zero-offset trace for the direct wave on the vertical geophone.

For estimating the value of impedance, $\rho_2\alpha_2$, from equation (4.28), we require the upgoing wavefield, *U*, to vanish. Then we have:

$$W(z_1^-) = \rho_2 \alpha_2 V_z(z_1^+). \tag{4.29}$$

By comparing the zero-offset trace for the direct wave on the hydrophone (Figure 4.3) with the corresponding trace for the direct wave on the vertical geophone (Figure 4.4), we obtain the estimated value of the impedance $\rho_2\alpha_2$ = 4395 kg/sm^2. Comparing with the real parameters used for generating the synthetic data, for which $\rho_2\alpha_2$ = 4405.8 kg/sm^2, it shows excellent agreement. We can conclude that this method of estimation is sound.

This good agreement is also illustrated. Figure 4.5 shows the scaled geophone trace after using the estimated value of impedance as the scaling factor.

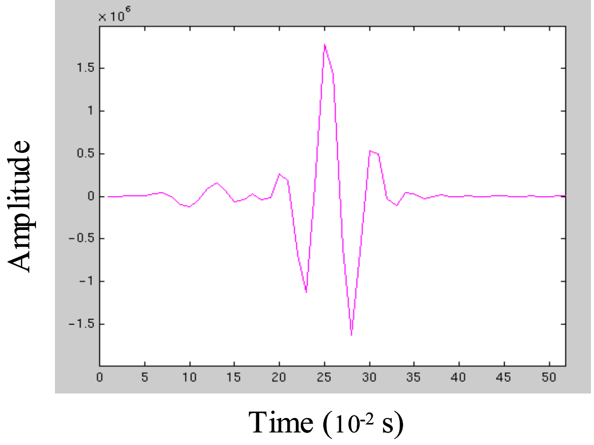

Figure 4.5. The scaled vertical-velocity trace.

When the synthetic zero-offset hydrophone trace, zero-offset vertical-geophone trace, and the $\rho_2\alpha_2$-scaled vertical-geophone trace together is plotted (Figure 4.6), we can see that the vertical-geophone trace has very small amplitude compared with that of the hydrophone trace. After using the estimated value of impedance as the scaling factor, they have almost the same amplitude. It demonstrates again that the medium parameter estimation is very good.

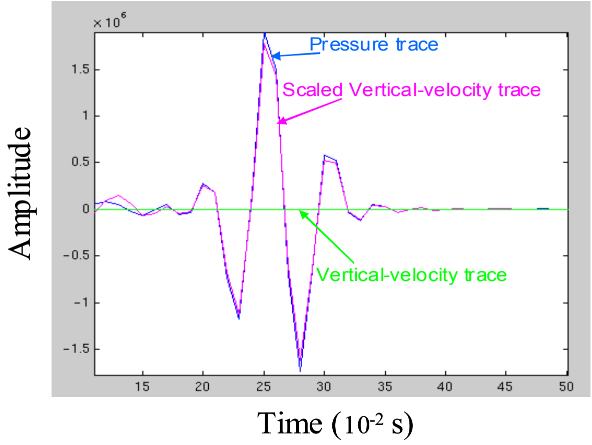

Figure 4.6. Superposition of pressure trace, vertical-geophone trace and scaled vertical-geophone trace.

For further estimating other elastic parameters, the estimated P-wave impedance, $\rho_2\alpha_2$, can be used as a constraint in minimizing the equations (4.21), (4.23) and (4.25) with respect to the elastic parameters (or requiring that $U = 0$), in a window containing the direct wave at a specific offset.

4.6 Synthetic data example

To test the performance of equations (4.19), (4.21), (4.23) and (4.27), I use synthetic seismograms modeled in a plane-layered medium. This is a 2D model with a 500-m water layer and two further reflectors at depths of 750 m and 900 m. P-wave velocities are 1500 m/s, 2100 m/s and 2500 m/s, S-wave velocities are 1.5 m/s, 700 m/s and 850 m/s, densities are 1000 kg/m^3, 2000 kg/m^3 and 2200 kg/m^3 in layers 1, 2 and 3, respectively. The synthetic data are generated by ElMo, an elastic modeling program based on the phase-shift-cascade method (Silawongsawat and Margrave, 1998). The synthetic hydrophone, vertical-geophone, and horizontal-geophone gathers are shown in Figures 4.7, 4.8 and 4.9, respectively. Note that primaries are present for events at approximately 0.59 and 0.72 s. The downgoing direct arrival and its reverberations are present for events at approximately 0.33, 1.01 and 1.67 s, respectively. Also notice that source-side multiples arrive at approximately 1.27 s.

After application of wavefield-separation equations (4.19), (4.21) and (4.23), the upgoing wavefields for each component are shown in Figures 4.10, 4.11 and 4.12. Comparing with Figures 4.7, 4.8 and 4.9, we can see that the multiples belonging to downgoing waves are successfully suppressed. However, the source-side multiple, an upgoing waves, still exists in the upgoing wavefields around 1.27s.

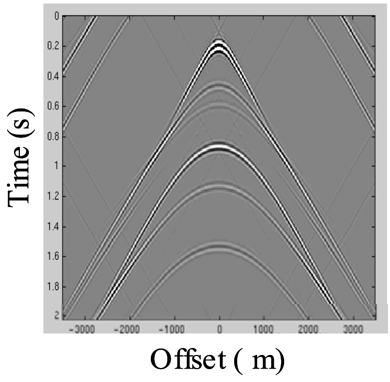

Figure 4.7. Modeled total wavefield for hydrophone component.

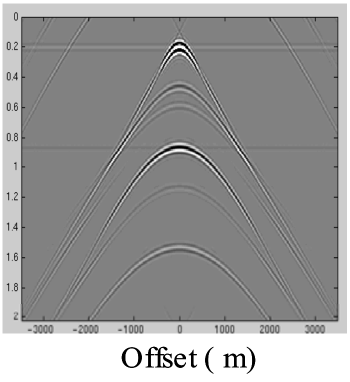

Figure 4.8. Modeled total wavefield for vertical-geophone component .

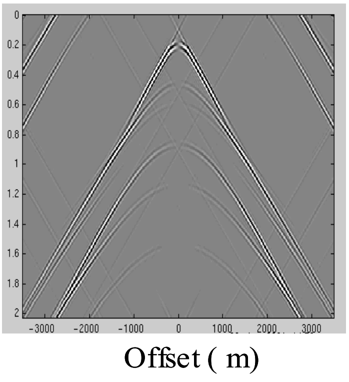

Figure 4.9. Modeled total wavefield for inline-geophone component.

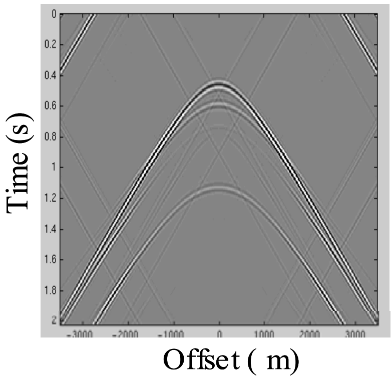

Figure 4.10. Decomposed upgoing hydrophone wavefield.

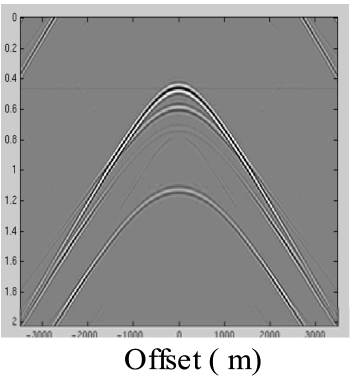

Figure 4.11. Decomposed upgoing vertical-geophone wavefield.

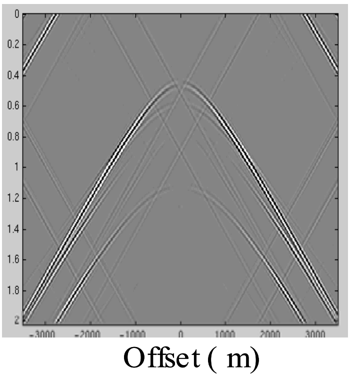

Figure 4.12. Decomposed upgoing inline-geophone wavefield.

After applying the cross-correlation method [equation (4.27)], this multiple is sufficiently suppressed and the final upgoing wavefields are shown in Figures 4.13, 4.14 and 4.15, respectively, where only the primaries are preserved.

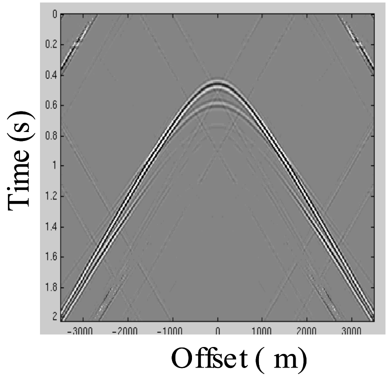

Figure 4.13. Eliminating the source-side multiple (hydrophone).

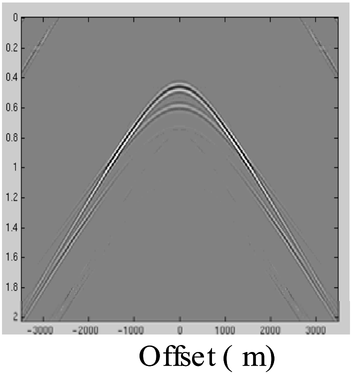

Figure 4.14. Eliminating the source-side multiple (vertical-geophone).

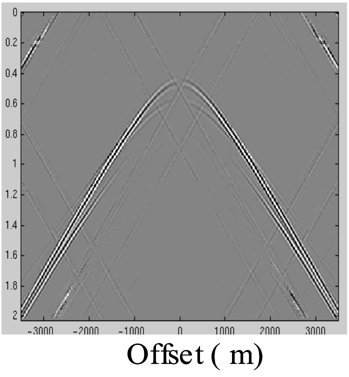

Figure 4.15. Eliminating the source-side multiple (inline-geophone).

For comparison, Barr and Sanders's dual-sensor method is also applied on this synthetic data. Input data are hydrophone data (Figure 4.16) and vertical geophone data (Figure 4.17). After applying the Barr and Sanders dual-sensor method, the result is showed in Figure 4.18. Comparing with the wavefield decomposition result (Figure 4.10), we can see these two decomposed results are virtually identical.

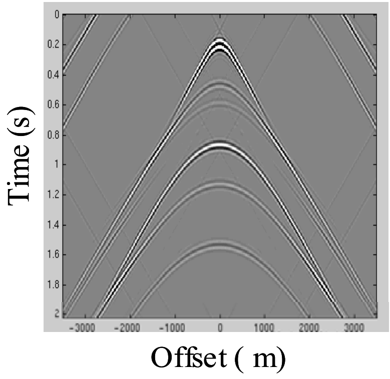

Figure 4.16. Modeled total wavefield for hydrophone component.

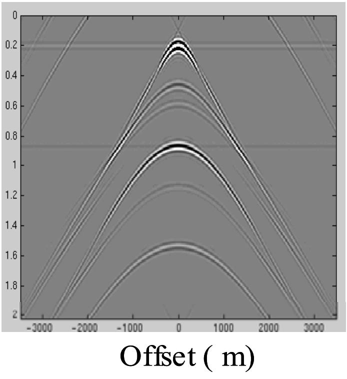

Figure 4.17. Modeled total wavefield for vertical-geophone component.

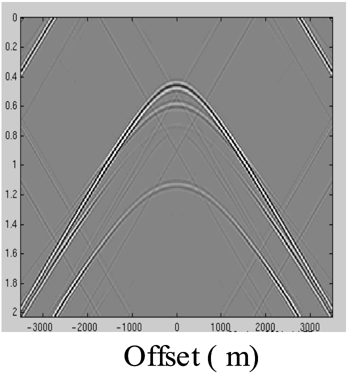

Figure 4.18. The upgoing wavefield by dual-sensor summation method

4.7 Real data example

The real OBS seismic data was acquired by Schlumberger company over the Mahogany Field in the Gulf of Mexico in 1996. The data was resampled at 4 ms and group interval was 25 m. From the dataset, a receiver position at the seafloor was selected where the pressure, vertical-particle velocity, and inline-particle velocity has been measured. Then we have the hydrophone, vertical-geophone, and inline-geophone common-receiver gathers. Prior to applying the multicomponent wavefield-decomposition technique for these gathers, some initial processing has been performed.

4.7.1 Polarity determination

Before any processing, first we should decide whether the datasets have normal or reverse polarity. How to ensure it? Brown et al. (2002) gave detailed guidelines. According to them, to ensure positive or normal polarity for the vertical component, the direct downgoing P should have positive onsets. For normal polarity on the hydrophone component, the direct P should then have negative onsets. For normal polarity on the inline component, the direct P should have positive onsets. This normally means flipping the inline component polarity for negative offsets (Brown et al., 2002).

Figure 4.19 shows the vertical-component common-receiver gather. The first breaks, due to direct downgoing P, are seen at zero offset at about 80 ms. This arrival has a positive break. For the hydrophone-component common-receiver gather (Figure 4.20), the direct P is seen to have negative break, as it should. Figure 4.21 shows the inline-component common-receiver gather. Note that positive-offset traces and negative-offset traces have the opposite polarity, after flipping polarity for negative offsets, the direct P wave now has a positive break for all offsets (Figure 4.22).

Figure (4.19), (4.20) and (4.21) show very noisy dataset. The water-column reverberation arriving after the direct arrival, and those multiples associated with primary reflections, contaminate the whole section. Primary events are difficult to identify on both hydrophone data and geophone data.

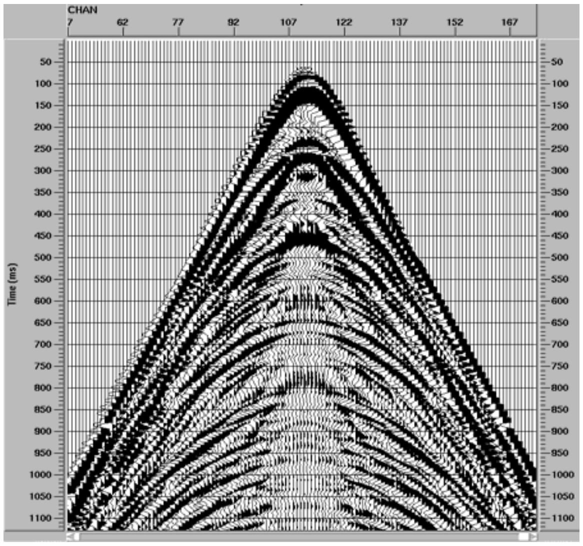

Figure 4.19. A vertical-component common-receiver gather from Mahogany.

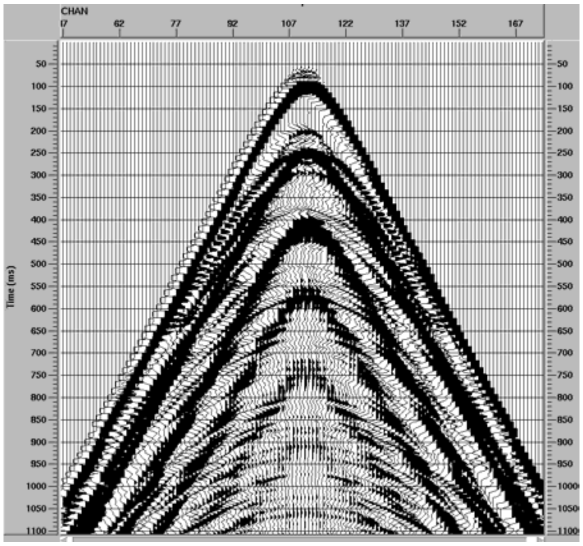

Figure 4.20. A hydrophone-component common-receiver gather from Mahogany.

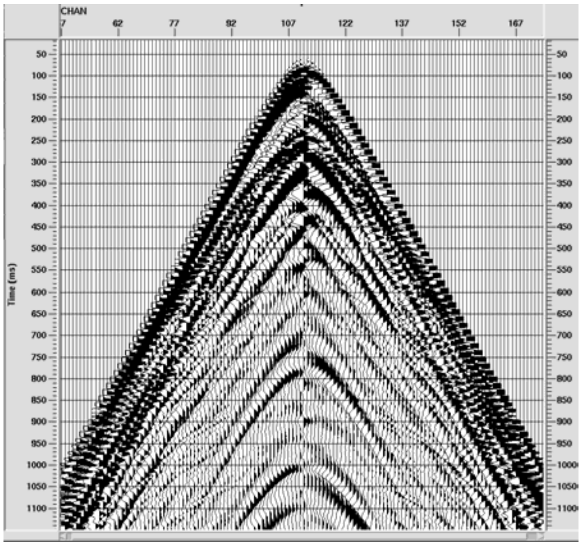

Figure 4.21. Inline-component common-receiver gather from Mahogany. Positive-offset traces have opposite polarity to that of negative-offset traces.

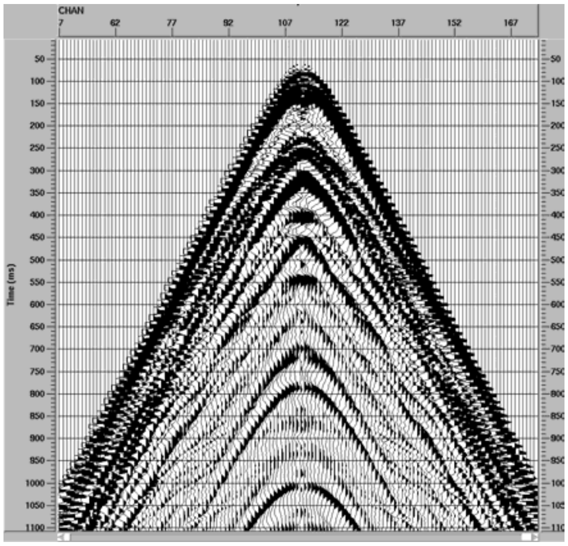

Figure 4.22. Inline-component common-receivergather (Figure 4.21) after flipping polarity for negative offsets. Note that negative offsets are on the right.

4.7.2 Calibration between hydrophone and vertical geophone

In marine data, due to measurement imperfections (e.g., different coupling, impulse response), the calibration relationship between the hydrophone and vertical geophone need to be resolved. Ball and Corrigan (1996) proposed that a match filter should be applied to the geophone trace to compensate for the different coupling and noise effects on the hydrophone and geophone trace. According to them, this match filter is estimated from the cross-ghosted traces. Cross-ghosted traces are the traces that result by applying the hydrophone ghost to the geophone traces, and the geophone ghost to the hydrophone traces. The primary and multiple trains of cross-ghosted traces should be the same, so cross-ghosted traces can be used to obtain the match filter.

Schalkwijk et al., (1999) also proposed another scheme to determine the calibration between the hydrophone and vertical-geophone components. They add the calibration filter λ into the acoustic decomposition equation (4.1), which becomes:

$$U_P^W(z_1^-) = \frac{1}{2}[W(z_1^-) + \lambda \frac{\rho_1}{q_{\alpha 1}} V_z(z_1^-)]. \tag{4.30}$$

If the acoustic medium parameters are known, the condition for solving for λ is that the data should be windowed to exclude the primary reflections (Schalkwijk et al., 1999).

Using the scheme described by Schalkwijk et al., (1999), setting the P-wave velocity of water to 1500 m/s and the density of water to 1000 kg/m^3 in equation (4.30), the scalar number for calibration between the hydrophone (Figure 4.19) and vertical geophone (Figure 4.20) can be obtained: $\lambda = 0.0021$.

4.7.3 Estimation of seafloor medium parameters

The wavefield-decomposition technique requires the seafloor medium parameters as input, so these should be known. For estimating the seafloor parameters from our real data, the strategy described in §4.5 is applied, requiring the upgoing wavefields $U^{W}(Z_1^+) = 0$ in equations (4.19) and $U^{V_z}(Z_1^+) = 0$ in equation (4.21), and obtained: α_2 = 1900 m/s, β_2= 550 m/s, and ρ_2 = 2019 kg/m^3.

For illustrating the goodness of these estimates, the estimated seafloor parameters are used to determine the scaling factor to scale the vertical-geophone trace, then plot the scaled vertical-geophone trace and hydrophone trace together, and the scaled vertical-geophone trace and inline- geophone trace together, respectively. Figure 4.23 shows the hydrophone trace (solid line) at 25-m offset with the scaled vertical-geophone trace (dash-dot line) for the optimal estimate: α_2 = 1900 m/s, β_2 = 550 m/s, and ρ_2 = 2019 kg/m^3. Figure 4.24 shows the inline trace (dash-dot line) for a 50-m offset and the scaled vertical-geophone trace (solid line) for the optimal estimates. From this illustration, it can be concluded that the estimation of seafloor parameters is sound.

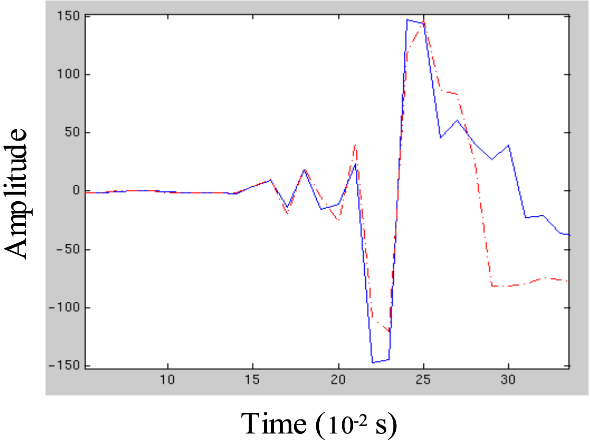

Figure 4.23. Comparison of the direct wave arrival at 25-m offset on the hydrophone trace (solid line) and the scaled vertical-velocity trace (dash-dot line) for the optimal estimates: α_2 = 1900 m/s, β_2 = 550 m/s, and ρ_2 = 2019 kg/m^3.

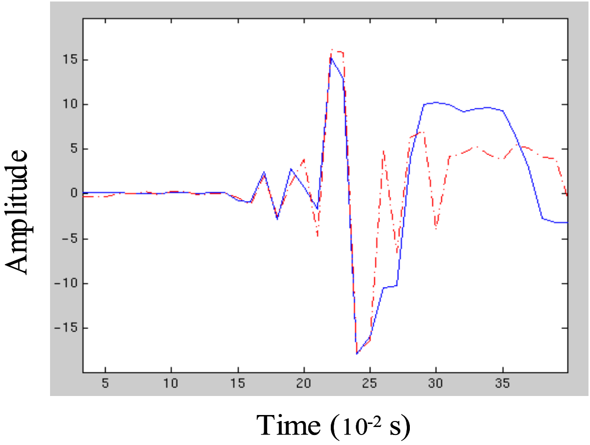

Figure 4.24. Comparison of the direct wave arrival at 50-m offset on the inline-geophone trace (dash-dot line) and the scaled vertical-geophone trace (solid line) for the optimal estimates: $\alpha_2 = 1900$ m/s, $\beta_2 = 550$ m/s, and $\rho_2 = 2019$ kg/m^3.

4.7.4 Decomposition results

After determining the dataset polarities, solving for the calibration between the hydrophone and vertical geophone, and estimating the seafloor medium parameters, the receiver gathers shown in Figures 4.19, 4.20 and 4.22 are then processed using our decomposition technique [equations (4.19), (4.21) and (4.23)]. The decomposed upgoing wavefields for the three components are shown in Figures 4.25 to 4.27, respectively. Comparing with the input data shown in Figures 4.19, 4.20 and 4.22, for the vertical-geophone and hydrophone components (Figures 4.25 and 4.26), the strong water-column reverberations arriving after the direct arrival at times around 100 ms, 260 ms, 420 ms, 580 ms, etc., are significantly attenuated, although, not be completely removed, while the primaries at times around 650 ms, 820 ms and 960 ms show better resolution and continuity in the upgoing wavefields. But for the inline-geophone component, water-column reverberations do not seem to be much attenuated in the upgoing wavefield (Figures 4.27).

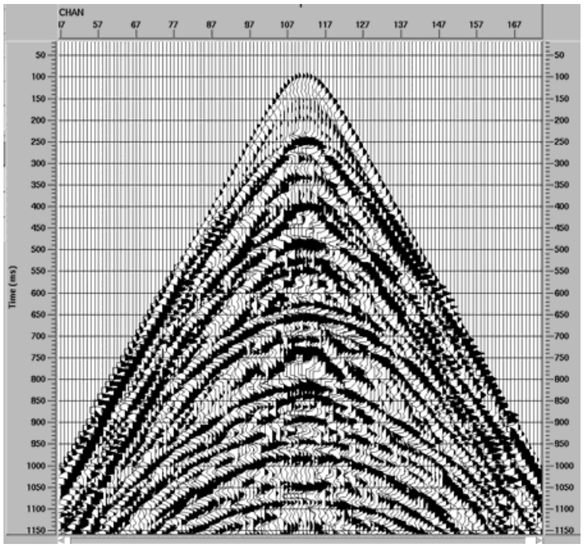

Figure 4.25. Decomposed upgoing wavefield for vertical-geophone component.

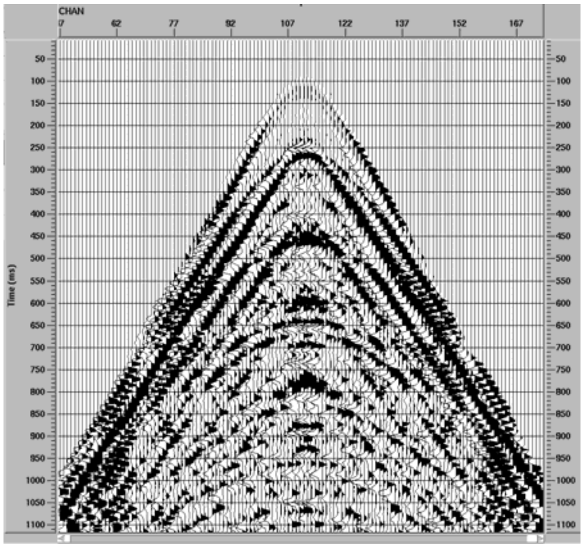

Figure 4.26. Decomposed upgoing wavefield for hydrophone component.

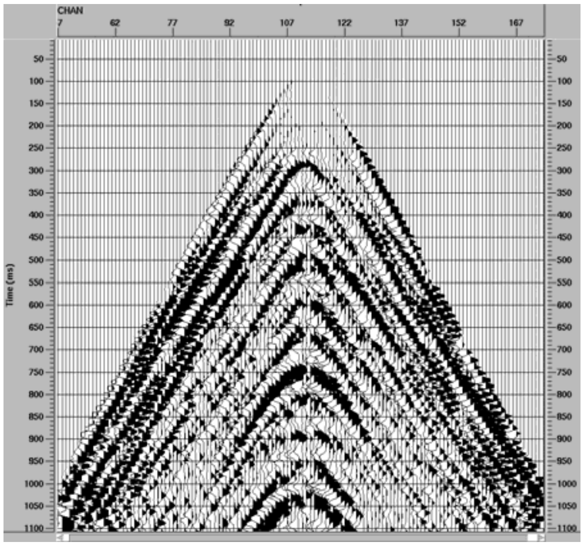

Figure 4.27. Decomposed upgoing wavefield for inline-geophone component.

4.8 Summary

The wavefield decomposition technique, decomposing wavefileds into upgoing and downgoing wavefields, is discussed. The algorithm for extracting the upgoing wavefields for three components (hydrophone, vertical-geophone, and inline-geophone) is implemented in the *f-k* domain and applied for the synthetic and real data.

In synthetic data example, since the seafloor medium parameters are known exactly, the wavefield decomposition technique works very well, after applying this technique, all downgoing waves, such as, receiver-side multiples, direct wave and accompanying reverberations, are sufficiently attenuated from the upgoing wavefields. Then, using crosscorrelation method, the source-side multiple can be further attenuated from the upgoing wavefields. But this method has certain limitation: it can not perform well when primary and multiple intersect. Also the feature used for identifying the source-side multiples only exist in laterally homogeneous cases including the uniform water depth. This method is not recommended to be used for real examples so far. In the real data example, since the seafloor medium parameters are unknown, also due to measurement imperfections (e.g., different coupling, impulse response), prior to applying the wavefield decomposition technique, the estimation of seafloor medium parameters and the calibration between different components have been performed. The accuracy of estimation of seafloor parameters and the calibration between different components will affect the decomposition results. Examples show that the quality of estimation and calibration results can be checked and, is necessary, improved. Final decomposition results show that the downgoing multiples are significantly attenuated and primaries can be observed quite confidently in decomposed upgoing wavefields on the vertical-geophone and hydrophone components. But the situation on the inline-geophone component is less clean, this result may be improved by also correcting the cross-coupling effects between the velocity components.

Chapter 5: Conclusions and future work

5.1 Conclusions

In marine seismic surveys, since the water-air interface is a strong reflector with underside reflection coefficient close to –1, the multiples caused by the free-surface are the most severe form of coherent noise found in marine seismic data. Many algorithms have been developed for water-column multiple attenuation, e.g., predictive deconvolution, K-L transform, *τ-p* transform and *f-k* attenuation. Generally, they can handle most of the water-column multiple energy. However, these methods were developed early and intended for application to the land data, and they have different limitations. Also, the degree of success of these methods generally depends on how well the recorded data agree with the assumptions which are made about them.

For OBS data, we generally use common-receiver gathers instead of common-shot gathers used in the land data case. A straightforward method for multiple attenuation on common-receive gather is the dual-sensor method, which combines the hydrophone data and the vertical-geophone data weighted by a proper scaling factor. After data summation, only the upgoing wavefieds are obtained.

Dual-sensor summation is a simple and popular method for water-column multiple attenuation of OBS data. In this thesis, a new method of estimating the scaling factor, based on cross-correlation of hydrophone and geophone data, is introduced. Experimental tests and comparison with two other dual-sensor methods have been performed on both synthetic data and field data. Test results show that these three methods perform well in different cases. For multiples that are associated with primary reflections from subseafloor horizons, Method I works best. For the water-column multiples that reverberate purely in the water-column and arrive from above as downgoing energy, Methods II and III work very well. When the hydrophone and geophone data are not exactly in phase, Method III performs the best of the three methods. None of the three methods is very sensitive to noise at the level applied ($S/N = 4$) on the synthetic traces.

The multicomponent wavefield-decomposition technique involved three or four components and has been developed as an extension of the dual-sensor method. The essence of the multicomponent wavefield-decomposition technique is combining the hydrophone, the vertical-geophone and horizontal-geophone components in proper proportions to obtain the upgoing and downgoing wavefields.

In this thesis, the algorithm for extracting the upgoing wavefields for three components (hydrophone, vertical-geophone, and inline-geophone) is implemented in the *f-k* domain and applied to both synthetic and real data. It works very well for synthetic data which provided the exact seafloor medium parameters. The upgoing wavefields without downgoing waves are successfully extracted. Then, using a crosscorrelation method, the source-side multiple is further attenuated from the extracted upgoing wavefields. But this crosscorrelation method has certain limitations: it can not perform well when primary and multiple intersect. Also the crosscorrelation technique used for identifying the source-side multiples is currently limited to laterally homogeneous cases including uniform water depth. This method needs further development before routine application to real data examples.

For real data, the calibration between different components should be performed to compensate the measurement imperfections, and the seafloor medium parameters have to be estimated prior to applying the wavefield-decomposition technique. Therefore, for real data, a better calibration between the measurements of the different components and a more accurate estimation of the seafloor medium parameters will benefit the decomposition results. Final decomposition results show that the downgoing multiples are significantly attenuated and primaries show better resolution and continuity and can be observed quite confidently in decomposed upgoing wavefields on the vertical-geophone and hydrophone components. But the situation on the inline-geophone component is less clean, this result may be improved by also correcting the cross-coupling effects between the velocity components.

Wavefield decomposition theory has been devised for multicomponent recordings at a locally flat seafloor where the seafloor medium parameters are constant while the subsurface may be arbitrary. It does not require the source signature but requires the seafloor parameters be known. It is a fairly straightforward method applied to attenuate the water-column multiples of OBS data. Also, it is computationally fast and can be easily implemented in the *f*-*k* domain.

5.2 Future work

Although considerable work on the wavefield-decomposition technique for multiple attenuation has been done in this thesis, there are many possibilities to improve and explore regarding this method.

A fundamental change to the algorithm would be extending its use into more general seafloor media. An approach for this purpose, valid for a heterogeneous, dipping seafloor has been proposed by Amundsen et al. (1998).

The synthetic data example in Chapter 4 illustrates the combination of multicomponent wavefield-decomposition techniques and how the crosscorrelation method can successfully attenuate the source-side multiple in the decomposed upgoing wavefields. However, it only works well on synthetic data in the laterally homogeneous case including uniform water depth. It would be good to expand this technique to the laterally heterogeneous case in order to apply it to real data. It would also be good if wavefield-decomposition techniques could be combined with other strategies to further attenuate the internal multiples. However, this would require a good model for the reflector that is generating the internal multiples.

In addition, precise velocity information for the seafloor provided by a good velocity-estimation method and a better calibration between measurements of different components can ensure good decomposition results. Well-log data, if available, may help to provide alternative velocity information.

References

Aki, K., and Richards, P. G., 1980, Quantitative seismology. W.H. Freeman and Company.

Amundsen, L., 1993, Wavenumber-based filtering of marine point source data: Geophysics, **58**, 1335-1348.

Amundsen, L., and Reitan, A., 1994, decomposition of multicomponent sea floor data into upgoing and downgoing P- and S-waves: Geophysics, **60**, 563-572.

Amundsen, L., and Reitan, A., 1995, Estimation of sea-floor wave velocities and density from pressure and particle velocity by AVO analysis: Geophysics, **60**, 1575-1578.

Amundsen, L., Ikelle, L. T. and Martin, J. E., 1998, Multiple attenuation and P/S splitting of OBC data: A heterogeneous seafloor: 68th Annual International SEG Meeting, Expanded Abstracts, 722-725.

Aytun, K., 1999, The footsteps of the receiver ghost in the *f-k* domain: Geophysics, **64**, 1618-1626.

Backus, M., 1959, Water reverberations, their nature and elimination: Geophysics, **24**, 233-261.

Bale, R., 1998, Plane-wave deghosting of hydrophone and geophone data: 68th Annual International SEG Meeting, Expanded Abstracts, 730-733.

Ball, V. and Corrigan, D., 1996, Dual-sensor summation of noisy ocean-bottom data: 66th Annual International SEG Meeting, Expanded Abstracts, 28-31.

Barr, F.J., 1997, Dual-sensor OBC technology: The Leading Edge, **16**, 45-51.

Barr, F.J., and Sanders, J.I., 1989, Attenuation of water-column multiples using pressure and velocity detectors in a water-bottom cable: 59th Annual International SEG Meeting, Expanded Abstracts, 653-656.

Barr, F.J., Chambers, R.E., Dragoset, W. and Paffenholz, J., 1997, A comparison of methods for combining dual-sensor ocean-bottom cable traces: 67th Annual International SEG Meeting, Expanded Abstracts, 67-70.

Berg, E., Svenning, B., and Martin, J., 1994, SUMIC: Multicomponent sea-bottom seismic surveying in the North Sea: Data interpretation and applications: 64th Annual International SEG Meeting, Expanded Abstracts, 477-480.

Berkhout, A.J., 1982, Seismic migration, imaging of acoustic energy by wavefield extrapolations: Elsevier Science Publishing Co., Inc.

Brown, R. J., and Yan, Y., 1999, Suppression of water-column multiples in multicomponent seafloor data: Preliminary results and proposal: CREWES Research Report, 311-321.

Brown, R. J., Stewart, R.R., and Lawton, D.C., 2002, A proposed polarity standard for multicomponent seismic data: Geophysics, **67**, 1028-1037.

Caldwell, J., Christie, P., Engelmark, F., McHugo, S., Özdemir, H., Kristiansen, P., and MacLeod, M., 1999, Shear waves shine brightly: Oilfield Review, **11**(1): 2-15.

Carvalho, F. M., Weglein, A. B., and Stolt, R. H., 1991, Examples of a nonlinear inversion method based on the T matrix of scattering theory: Application to multiple suppression: 61th Annual International SEG Meeting, Expanded Abstracts, 1319-1322.

Claerbout, J. F., 1976, Foundamentals of geophysical data processing: McGraw-Hill Book Co.

Dragoset, W. and Barr, F.J., 1994, Ocean-bottom cable dual-sensor scaling: 64th Annual International SEG Meeting, Expanded Abstracts, 857-860.

Foster, D. J. and Mosher, C. C., 1992, Suppression of multiple reflections using the Radon transform: Geophysics, **57**, 386-395.

Gidlow M. and Sonnier J., 2001, Triple sensor wavefield separation: 63rd Annual Conference, European Association of Geophysicists and Engineers, Extended Abstracts, Session L-10.

Hampson D., 1986, Inverse velocity stacking for multiple elimination: Journal of the Canadian Society of Exploration Geophysicists, **22**, 44-55.

Hemon, C.H. and Mace, D., 1978, Use of the Karhunen-Loève transformation in seismic data processing: Geophysical Prospecting, **26**, 600-626.

Jones, I.F., 1985, Application of the Karhunen-Loève transformtion in reflection seismic processing: Ph.D. thesis, University of British Columbia.

Jones, I.F., and Levy, S. 1987, Signal-to-noise ratio enhancement in multichannel seismic data via the Karhunen-Loève transform: Geophysical Prospecting, **35**, 12-32.

Liu, X., 1999, Ground roll suppression using the Karhunen-Loève transform: Geophysics, **64**, 564-566.

Margrave, G. F., 1999, The methods of seismic data processing: Department of Geology and Geophysics, University of Calgary.

Matson, K. and Weglein, A.B., 1996, Removal of elastic interface multiples from land and ocean-bottom data using inverse scattering: 66th Annual International SEG Meeting, Expanded Abstracts, 1526-1529.

O'Brien, S.R.M., 1997, Adaptive raytracing-based suppression of severe water-bottom multiples in marine seismic data: Ph.D. thesis, Memorial University of Newfoundland.

Osen, A., Amundsen, L., and Reitan, A., 1999, Removal of water-layer multiples from multicomponent sea-bottom data: Geophysics, **64**, 838-851.

Paffenholz, J. and Barr, F.J., 1995, An improved method for deriving water-bottom reflectivities for processing dual-sensor ocean-bottom cable data: 65th Annual International SEG Meeting, Expanded Abstracts, 987-990.

Peacock, K.L. and Treitel, S., 1969, Predictive deconvolution: theory and practice: Geophysics, **34**, 155-169.

Robinson, E.A. and Treitel, S., 1980, Geophysical signal analysis, Prentice Hall Inc.

Rodriguez, S. C., 2000, Advanced marine seismic methods: Ocean-bottom and vertical cable analyses: Ph.D. thesis, University of Calgary.

Russell, B. and Hampson, D., 1990. Noise elimination and the Radon transform: The Leading Edge, **37**, 18-23.

Schalkwijk, K. M., Wapenaar, C.P.A., and Verschuur, D.J., 1999, Application of two-step decomposition to multicomponent ocean-bottom data: Theory and case study: Journal of Seismic Exploration, **8**, 261-278.

Silawongsawat, C. and Margrave, G. F., 1998, The phase-shift cascade method of elastic wavefield modeling: 68th Annual International SEG Meeting, Expanded Abstracts, 1807-1810.

Tatham, R.H., Keeney, J.W. and Noponen, I., 1983, Application of the τ-p transform in processing seismic reflection data: 53rd Annual International SEG Meeting, Expanded Abstracts, 163-172.

Ulrych, T.J., Levy, S., Oldenburg, D.W. and Jones, I.F., 1983, Application of the Karhunen-Love transformtion in reflection seismology: 53rd Annual International SEG Meeting: S6.5.

Verschuur, D. J., Berkout A. J., Matson, K.H., Weglein, A.B., and Young, C.Y., 1998, Comparing the interface and point scatterer methods for attenuating internal multiples: a study with synthetic data-Part I: 68th Annual International SEG Meeting, Expanded Abstracts, 1519-1522.

Weglein, A.B., Gasparotto, F.A., Carvalho, P.M. and Stolt, R.H., 1997, An inverse-scattering series method for attenuating multiples in seismic reflection data: Geophysics, **62**, 1975-1989.

White, J. E., 1965, Seismic waves: Radiation, transmission and attenuation: McGraw-Hill, Inc., New York.

Yilmaz Ö. 1987, Seismic data processing: Society of Exploration Geophysicists.